

High-resolution, Real-time 3-D Shape Measurement

A Dissertation Presented

by

Song Zhang

to

The Graduate School

in Partial Fulfillment of the

Requirements

for the Degree of

Doctor of Philosophy

in

Mechanical Engineering

Stony Brook University

May 2005

Copyright by
Song Zhang
2005

Stony Brook University
The Graduate School
Song Zhang

We, the dissertation committee for the above candidate for the

Doctor of Philosophy degree,
hereby recommend acceptance of this dissertation.

Dr. Peisen S. Huang, Advisor
Department of Mechanical Engineering

Dr. Fu-Pen Chiang, Chairman
Department of Mechanical Engineering

Dr. Jeffrey Q. Ge, Member
Department of Mechanical Engineering

Dr. Klaus Mueller, Outside member
Department of Computer Science

Dr. Xianfeng Gu, Outside member
Department of Computer Science

This dissertation is accepted by the Graduate School

Dean of the Graduate School

Abstract of the Dissertation

High-resolution, Real-time 3-D Shape Measurement

by

Song Zhang

Doctor of Philosophy

in

Mechanical Engineering

Stony Brook University

2005

High-resolution, real-time 3D shape measurement for dynamically deformable objects has a huge potential for applications in many areas, including entertainment, security, design and manufacturing, etc. However, due to the challenging nature of the problem, no system with such capability has ever been developed. The focus of this dissertation research is to develop such a system and to demonstrate its practical value for applications in many fields.

The system we develop is based on a digital fringe projection and phase-shifting technique. It utilizes a single-chip Digital-Light-Processing (DLP) projector to project computer generated fringe patterns onto the object and a high-speed Charge-Coupled-Device (CCD) camera synchronized with the projector to acquire the fringe images at a frame rate of 120 frames per second. Based on a three-step phase-shifting technique, each frame of the 3D shape is reconstructed using three consecutive fringe images. Therefore the 3D data acquisition speed of the system is 40 frames per second. Together with fast 3D reconstruction algorithms and parallel processing software we developed, high-resolution, real-time 3D shape measurement is realized at a frame rate of up to 40 frames per second and a resolution of 532×500 points per frame.

Real-time 3D reconstruction is difficult if the traditional sinusoidal three-step phase shifting algorithm is used with an ordinary personal computer. Therefore, we developed a novel phase shifting algorithm, namely, trapezoidal phase-shifting algorithm, for real-time 3D shape measurement. This new algorithm replaces the calculation of a computationally more time-consuming arctangent function with a simple intensity ratio calculation, thus boosting the processing speed by at least 4.5 times when compared to the traditional sinusoidal algorithm. With this algorithm, 3D reconstruction in real time was shown to be feasible.

One shortcoming of the trapezoidal phase-shifting algorithm is that the measurement accuracy is affected by image defocus, which limits the dynamic range of measurement. Even though the error caused by image defocus is rather small, especially when compared with other intensity ratio based methods, this error has to be eliminated if high accuracy measurement is desired. In this research, we found that we could use the trapezoidal algorithm to process sinusoidal fringe images with a small error and then use a LUT method to eliminate the error. The result is a new algorithm, namely, fast phase-wrapping algorithm, which is 3.4 times faster than and just as accurate as the traditional algorithm. Essentially this new algorithm combines the speed advantage of the trapezoidal algorithm and the accuracy advantage of the traditional algorithm. By implementing this algorithm in our system, we were able to achieve real-time 3D reconstruction with high accuracy.

In the three-step phase-shifting method we utilize, the non-sinusoidal nature of the fringe patterns as a result of the nonlinear gamma curve of the projector causes significant phase measurement errors and therefore shape measurement errors. Previously proposed methods based on direct compensation of the nonlinearity of the projector gamma curve demonstrated significant reduction of the measurement error, but the residual error remains non-negligible. In this research, we propose a novel error compensation method that can produce significantly better results. This method was developed based on our finding that the phase error due to non-sinusoidal fringe patterns depends only on the nonlinearity of the projector's projection response curve (or gamma curve). Our experimental results demonstrated that by using the pro-

posed method, the measurement error could be reduced by 10 times. In addition to error compensation, a similar method is also proposed to correct the non-sinusoidality of the fringe patterns for the purpose of generating a more accurate flat image of the object for texture mapping, which is important for applications in computer vision and computer graphics.

System calibration, which usually involves complicated time-consuming procedures, is crucial for any 3D shape measurement system. In this research, a novel approach is proposed for accurate and quick system calibration. In particular, a new method is developed that enables the projector to “capture” images like a camera, thus making the calibration of a projector the same as that of a camera. This is a significant development because today projectors are increasingly used in various measurement systems yet so far no systematic way of calibrating them has been developed. Our experimental results demonstrated that the measurement accuracy of our system after calibration is less than RMS 0.22 mm over a volume of $342 \times 376 \times 658$ mm.

Dedicated to My Family

Table of Contents

List of Figures	x	
List of Tables	xiv	
Acknowledgments	xv	
1	Introduction	1
1.1	Motivations	1
1.1.1	Computer vision and graphics	1
1.1.2	Medical imaging and diagnosis	2
1.1.3	Online inspection and quality control	2
1.1.4	Recognition	2
1.2	Related Works	3
1.2.1	Image-based techniques	3
1.2.2	Time of flight method	5
1.2.3	Structured light techniques	6
1.2.4	Wave optics-based techniques	8
1.2.5	Real-time techniques	11
1.3	Objectives	12
1.4	Dissertation Structures	13
2	3D Shape Measurement Based on Digital Fringe Projection Techniques	15
2.1	Digital Micro-mirror Devices (DMD) and DLP Projectors	15
2.2	Phase Shifting Interferometry	18
2.2.1	Fundamental concepts	18
2.2.2	Fringe projection	19
2.2.3	Three-step phase-shifting algorithms	21
2.2.4	Phase unwrapping methods	22
2.3	Typical 3D Shape Measurement System Setup	26
2.4	Summary	28

3	High-resolution, Real-time 3D Shape Measurement System	29
3.1	Introduction	29
3.2	Principle	30
3.2.1	Projection mechanism of a single-chip DLP projector	30
3.2.2	System synchronization	31
3.2.3	Color-encoded three-step phase-shifting algorithm	32
3.2.4	Projection nonlinearity correction	34
3.2.5	Coordinate conversion	35
3.3	Real-time 3D Shape Measurement System	39
3.3.1	System setup	39
3.3.2	Experiments	41
3.4	System with Color Texture Mapping	43
3.4.1	System setup	43
3.4.2	Camera synchronization	45
3.4.3	Camera alignment	47
3.4.4	Experiments	48
3.5	Real-time 3D Shape Measurement System: Generation II	48
3.6	Real-time 3D Data Acquisition, Reconstruction, and Display System .	50
3.6.1	Principle	50
3.6.2	Experiments	53
3.7	Discussion	53
3.8	Summary	55
4	Trapezoidal Phase-shifting Algorithm	57
4.1	Introduction	57
4.2	Trapezoidal Phase-shifting Method	58
4.3	Error Analysis	60
4.3.1	Image defocus error	60
4.3.2	Nonlinearity error	65
4.4	Experiments	65
4.5	Conclusions	66
5	Fast Phase-wrapping Algorithm	68
5.1	Introduction	68
5.2	Principle	69
5.2.1	Fourier analysis of the trapezoidal phase-shifting algorithm . .	69
5.2.2	Fast phase-wrapping algorithm	71
5.3	Error Analysis and Compensation	72
5.4	Experiments	74
5.5	Conclusion	76
6	Error Compensation Algorithm	78
6.1	Introduction	78
6.2	Principle	79
6.2.1	Phase correction	79

6.2.2	Texture recovering	82
6.3	Simulation Results	84
6.4	Experimental Results	85
6.5	Discussions	87
6.6	Conclusions	88
7	System Calibration	90
7.1	Introduction	90
7.2	Principle	91
7.2.1	Camera model	91
7.2.2	Camera calibration	94
7.2.3	Projector calibration	95
7.2.4	System calibration	99
7.2.5	Phase-to-coordinate conversion	102
7.3	Experiments	103
7.4	Calibration Evaluation	104
7.5	Discussion	108
7.6	Conclusions	111
8	Conclusions and Future Works	113
8.1	Conclusions	113
8.2	Future Works	115
Appendix		
A	World Coordinates Calculation	119
Bibliography		121

List of Figures

Figure

2.1	Single-chip DLP projection system configuration.	16
2.2	Principle of interference. (a)-(b) fringe patterns generated by the interference of two coherent point sources.(c)-(d) Fringe pattern generated by the interference of two coherent parallel planar light waves.	20
2.3	3D result by the path integration phase unwrapping method.	23
2.4	3D reconstruction by two-wavelength phase-unwrapping algorithm.	25
2.5	GUI interactive phase unwrapping tool. (a) Reconstructed 3D model. (b) 2D photo of the object.	27
2.6	3D reconstruction using the GUI tool. Image from left to right are: 2D photo, 3D with problems, 2D photo with spline drawn to separate regions, and corrected reconstructed 3D geometry.	27
2.7	Typical 3D shape measurement system setup.	28
3.1	DLP projector and color filters. (a) Projector with photo sensor. (b) Projector with color filters. (c) Projector without color filters.	31
3.2	System timing chart.	32
3.3	System synchronization timing chart.	33
3.4	Color encoded sinusoidal fringe pattern.	33
3.5	System projection response curve. (a) The curves before nonlinearity compensation. (b)The curves after compensation.	35
3.6	Schematic diagram of phase-to-height conversion.	37
3.7	Measurement result of a flat board with a step.	38
3.8	Schematic diagram of the real-time 3D shape measurement system. .	39
3.9	Photograph of the real-time 3D shape measurement system.	40
3.10	Schematic diagram of the timing signal generator circuit.	41
3.11	3D Vision software modules.	42
3.12	Measured result of a flat board with a smooth surface.	42
3.13	3D shape measurement results of the sculpture Sapho. (a) $I_1(-2\pi/3)$. (b) $I_2(0)$. (c) $I_3(2\pi/3)$. (d) 3D geometry. (e) 3D geometry with texture mapping.	43

3.14	3D shape measurement result of a human face. (a) $I_1(-2\pi/3)$. (b) $I_2(0)$. (c) $I_3(2\pi/3)$. (d) 3D geometry. (e) 3D geometry with texture mapping.	43
3.15	Measurement results of human facial expressions.	44
3.16	Schematic diagram of the real-time 3D shape measurement system with color texture mapping.	45
3.17	Color system timing chart.	46
3.18	Photograph of the real-time 3D shape measurement system with color texture mapping.	47
3.19	Real-time 3D measurement result of human facial expression with color texture mapping.	48
3.20	Photograph of real-time 3D shape acquisition system: Gen II.	49
3.21	Measurement results using the new system. From left to right are Lincoln, Zeus, Angel, and Horses.	50
3.22	Measurement results of facial expressions using the new system.	51
3.23	Real-time 3D acquisition, reconstruction, and rendering pipeline.	52
3.24	Experimental environment for real-time 3D shape acquisition, reconstruction, and display.	54
3.25	Experiment on real-time 3D shape acquisition, reconstruction and display.	55
4.1	Phase-shifted trapezoidal fringe patterns.	61
4.2	Cross section of the intensity-ratio map.	61
4.3	Cross section of the intensity-ratio map after removal of the triangles.	61
4.4	Comparison of the intensity ratios with and without image defocus. Here the filter window size used in the calculation is T	63
4.5	Maximum error due to image defocus.	63
4.6	Blurring effect of the trapezoidal fringe pattern due to image defocus.	64
4.7	Enlarged view of the blurring effect of the trapezoidal fringe pattern in the borderline area between regions $N = 1$ and $N = 2$	64
4.8	3D shape measurement of a cylindrical part.	66
4.9	3D shape measurement of a plaster sculpture.	67
4.10	3D shape measurement of human faces.	67
5.1	Cross sections of the three phase-shifted sinusoidal patterns.	71
5.2	Cross section of the intensity ratio map.	72
5.3	Cross section of the intensity ratio map after removal of the triangular shape.	72
5.4	Error caused by the fast phase-wrapping algorithm.	74
5.5	Fringe images of a flat board captured by a 8-bit B/W CCD camera.	75
5.6	Residual phase error. (a) With the traditional algorithm. (b) With the proposed algorithm before error compensation. (c) With the proposed algorithm after error compensation.	76

5.7	Reconstructed 3D result of a sheet metal by fast phase-wrapping algorithm. (a) $I_0(-2\pi/3)$. (b) $I_1(0)$. (c) $I_2(2\pi/3)$. (d) 3D shape using the traditional phase-wrapping algorithm. (e) 3D shape using the fast phase-wrapping algorithm. (f) 3D shape difference using the traditional and the fast phase-wrapping algorithms.	77
5.8	3D reconstruction results of sculpture Lincoln. (a)2D photo. (b)3D shape using the traditional phase-wrapping algorithm. (c)3D shape using the fast phase-wrapping algorithm.	77
6.1	Camera image generation procedure.	81
6.2	Typical projection response curve.	82
6.3	Cross section of simulated fringe images before and after correction. (a) Cross sections of fringe images without correction. (b) Cross sections of fringe images after correction.	85
6.4	Phase error before and after error compensation.	85
6.5	Fringe correction for real captured fringe images. (a) Cross section of captured fringe images. (b)Cross section of fringe images after correction.	86
6.6	3D results can be corrected by our algorithms. (a) 3D geometry without correction. (b) 3D geometry after correcting fringe images. (c) 3D geometry after correcting the phase. (d) 250 th row cross section of the above image. (e) 250 th row cross section of the above image. (f) 250 th row cross section of the above image.	87
6.7	Texture image correction by using the proposed algorithm. (a) 2D texture before correction. (b)2D texture after correction.	88
6.8	3D measuring results of sculptures before and after error compensation. (a) 3D result without error compensation. (b) 3D result after fringe image correction. (c) 3D result after phase error correction. (d) 3D result with corrected texture mapping. (e) 3D result without error compensation. (f) 3D result after fringe image correction. (g) 3D result after phase error correction. (h) 3D result with corrected texture mapping.	89
7.1	Pinhole camera model.	92
7.2	Checkerboard for calibration. (a) Red/blue checkerboard. (b) White light illumination, B/W camera image. (c) Red light illumination, B/W camera image.	95
7.3	Camera calibration images.	96
7.4	Correspondence between the CCD image and the DMD image. (a)–(c) CCD horizontal fringe images I_1 , I_2 , and I_3 , respectively. (d) CCD horizontal centerline image. (e) DMD horizontal fringe image. (f)–(h) CCD vertical fringe images I_1 , I_2 , and I_3 , respectively. (i) CCD vertical centerline image. (j) DMD vertical fringe image.	97
7.5	CCD image and its corresponding DMD image.	99
7.6	World coordinate system.	100

7.7	World coordinate system construction.	100
7.8	Structured light system configuration.	101
7.9	3D measurement result of a planar surface.	104
7.10	Measurement error after calibration.	104
7.11	3D Measurement result of sculpture Zeus.	105
7.12	Positions and orientations of the planar board for the evaluation of the calibration results.	106
7.13	Planar error correlated to the poses of the measured plane using our calibration method. (a) Planar error vs plane position. (b) Planar error plane rotation angel around x axis. (c) Planar error vs plane rotation angel around y axis. (d) Planar error vs plane rotation angel around z axis.	109
7.14	Planar error correlated to the poses of the measured plane using traditional approximate calibration method. (a) Planar error vs plane position. (b) Planar error plane rotation angel around x axis. (c) Planar error vs plane rotation angel around y axis. (d) Planar error vs plane rotation angel around z axis.	110
7.15	Measurement result of a cylinder. (a) Cross section of the measured shape using our calibration method. (b) Cross section of the measured shape using the approximate calibration method. (c) Shape error for our calibration. (d) Shape error for the traditional approximate calibration method.	111
7.16	Error caused by nonlinear image distortions.	112
8.1	Tangent projection effect and possible solution. (a)Fringe image. (b)3D reconstructed result. (c) Gamma map.	116
8.2	Full field real-time 3D measurement system.	117

List of Tables

Table

7.1 Measurement data of the testing plane at different positions and orientations	107
---	-----

Acknowledgements

First and most important, I would like to express my sincere and deep gratitude to Professor Peisen S. Huang for his valuable guidance and constant academic and financial support during my Ph.D. dissertation research. I have learned a tremendous amount under his supervision.

I truly appreciate my committee members, Professor Fu-Pen Chiang, Jeffrey Q. Ge, Klaus Mueller, and Xianfeng Gu, for their precious time and invaluable suggestions on this dissertation.

My thanks also goes to Chengping Zhang for his advice at the early stages of my research; Tao Xian for his help on camera calibration; Hui Zhang for his advice on circuit design; Shizhou Zhang for his help on machining parts; Miranda White at Iowa State University, and Jackson L. Achinya for proofreading my writing; Christopher Carner and Yan Li for serving as models of our experiments. Qingying Hu, Xiaolin Li, Jian Zhou, and Li Shen, etc. for their precious friendships.

I give special thanks to Professor Shing-Tung Yau at Harvard University, for his inspiration on mathematics and methodologies for problem solving, without which, the problems of error compensation (Chapter 7) and system calibration (Chapter 8) would not have been possible to solved.

I would also like to offer a special thanks to my parents, though they cannot read even one letter of my thesis, for their continuous support and understanding.

And last but not least, I would express my deepest gratitude and thanks to my wife, Xiaomei Hao, for her endless support and understanding for my research work. Her constant encouragement and support was, in the end, what made this dissertation possible.

Chapter 1

Introduction

High-resolution, real-time 3D shape measurement for dynamically deformable objects has huge potential applications in many areas, including entertainment, security, design and manufacturing, etc. However, due to the very challenging nature of the problem, so far no system with such capability has ever been developed. The focus of this dissertation research is to develop such a system and to demonstrate its potential values in various applications. High-resolution, real-time 3D data acquisition, reconstruction and display has been a long dream. The objective of this dissertation research is to develop a system that makes this dream come true.

The motivations of this research are introduced in Section 1.1. Related works are reviewed in Section 1.2. Objectives of this research are addressed in Section 1.3. The structure of this dissertation is introduced in Section 1.4.

1.1 Motivations

1.1.1 Computer vision and graphics

One of the key research topics in computer vision and graphics is how to create realistic virtual world, real-time 3D being the goal. But before the computer can model and create the virtual world there must be a way to measure the real world. The measured data can be used as standard for computers to create “similar” world to that real world. Therefore, the first step of computer graphics is to obtain information about the real world. For example, in order to model human expressions such as “smile”, a number of “smiling” faces have to be captured and analyzed and common

features have to be extracted. This common smile can be transferred to another subject to make the other subject perform the same smile. The game industry benefits from the same technology: the player can be digitized and put into the virtual gaming world in real time.

1.1.2 Medical imaging and diagnosis

The motion of human organs, like lungs, provides information on the condition of human body. Doctors can diagnose what certain diseases are by the motion features of certain organs. For example, by measuring the volumetric movement of the lung, doctors can diagnose many diseases related to lung functions. Accurately capturing motions of the human body helps doctors since the digitized data provides useful information about the patient's health condition.

1.1.3 Online inspection and quality control

3D real-time measurement is an ongoing request in industry to drive down product cost and increase both productivity and quality. Real-time 3D shape measurement is the key to successfully implementing 3D coordinate measurement, manufacturing control, and online inspection.

1.1.4 Recognition

3D data provides more accurate information about the object than 2D data. Therefore, generating accurate 3D geometric information is a better solution for pattern recognition. Current recognition methods such as facial recognition are mostly based on 2D images. The problem of using 2D images is that it is pose sensitive. In other words, measuring the same subject from different perspective gives different results. However, 3D geometric information is significantly less sensitive to the pose of the subject since the geometric shape preserves. A system that could provide both 3D and 2D data would be a plus.

1.2 Related Works

With the recent technological advances in digital imaging, digital projection display, and personal computers, 3D shape measurement techniques have developed rapidly. Traditional Coordinate Measuring Machines(CMMs) could not meet all the needs of obtaining 3D information. Optical metrology has been more and more extensively employed. A number of methods have been developed to obtain 3D geometric information, namely, stereo vision [1], shape from shading [2], shape from focus and defocus [3, 4], laser stripe scanning [5], and time or color-coded structured light [6, 7, 8]. Among optical techniques, stereo vision is probably one of the most studied. However, finding the correspondence is fundamentally a difficult problem. Replacing one camera of a stereo vision system with a projector and projecting structured patterns onto the object can fundamentally solve the matching problem, which is called structured light system. Binary coding based structured light system can provide 3D information quickly, but with low resolution.

In this section, we briefly review some well-known optical 3D measurement techniques. They are: image based methods such as stereo vision, photogrammetry, shape from shading, shape from focus and defocus; time of flight; structure light methods; wave optics based methods such as optical interferometry and Moiré contouring; and digital fringe projection techniques. Finally, we discuss methods that can be used for real-time 3D shape measurement.

1.2.1 Image-based techniques

Image-based methods have been very broadly explored in the field of computer vision research. These methods analyze how an image is formed and how light affects that image. Obtaining the physical parameters of the imaging system is needed to obtain depth information through complicated image analysis procedures. Among all the existing methods, stereo vision, photogrammetry, shape from shading, and shape from focus and defocus are well known.

1.2.1.1 Stereo vision

Stereo vision is a long studied technique that tries to “simulate” the human eye. It requires pictures to be taken from two or more perspectives [9]. 3D information is obtained by identifying common features in two images. Compared with the active methods, stereo vision is a low cost method in terms of system setup. However, searching correspondence (stereo matching) has become a fundamentally difficult problem over the last decades [1]. Some techniques, such as correlation based techniques [10, 11], and multi-resolution techniques [12, 13], have been developed to provide robust or fast stereo matching [14, 15]. Recently, Zhang *et al.* [16] and Davis *et al.* [8] developed a new concept called spacetime stereo, which extends the matching of stereo images into the time domain. By using both spatial and temporal appearance variations, it is shown that matching ambiguity could be reduced and accuracy could be increased. As an application, Zhang *et al.* demonstrated the feasibility of using spacetime stereo to reconstruct shapes of dynamically changing objects [16]. The shortcoming of spacetime stereo or any other stereo vision method is that the matching of stereo images is usually time consuming. Therefore, it is difficult to reconstruct 3D shapes from stereo images in real time and in high resolution.

1.2.1.2 Photogrammetry

Typical photogrammetry methods employ the stereo technique to measure 3D shape, although other methods such as defocus, shading, and scaling can also be used. Photogrammetry is mainly used for feature type of 3D measurement and must usually have some bright markers on the surface of a measured object. In general, photogrammetric 3D reconstruction is established on the bundles of light rays [17].

1.2.1.3 Shape from shading

Shape-from-shading is a method for determining the shape of a surface from its image [18]. Shape-from-shading deals with the recovery of shape from a gradual variation of shading in the image. To solve the shape-from-shading problem, it is important to study how the images are formed. The Lambertian model is a simple

model of image formation in which the gray level of a pixel in the image depends on the direction of the light source direction and the normal direction of the surface. Given a gray level image in shape-from-shading, the aim is to recover the light source and the surface shape at each pixel in the image. Reconstructing the shape from shading can be reduced to solve a first-order, nonlinear partial differential equation. However, real images do not always follow the Lambertian model; Therefore, shape-from-shading is rarely used for real 3D measurement [2].

1.2.1.4 Shape from focus and defocus

In the image formed by an optical system such as a convex lens, objects at a particular distance (or depth) from the lens will be focused whereas at other distances or depths from the lens will be blurred or defocused by varying degrees depending on their distance. This suggests that the degree of the image blur can be a source of depth measurement. In the shape-from-focus approach, one of the camera parameters, such as the image detector position or the focal length, is varied until the object of interest is in focus. The distance of the object is then obtained using a lens formula [19, 20]. In the shape from defocus approach the level of defocus of the object is taken into account in determining that depth, therefore, it only requires processing a few images (2 or 3) as compared to the large number (approximately 10) of images in the shape-from-focus approach [4]. In order to do 3D measurement, shape from focus and defocus requires the user to know exactly the optical parameters of the imaging system. Even though those parameters can be calibrated, the computation is usually very expensive. Moreover, since the camera usually has a focal range, it is lesser sensitive to distance change, therefore, the real measuring accuracy cannot be very high.

1.2.2 Time of flight method

3D shape measuring methods based on the concept of time of flight directly measure the range to a point on an object by measuring the time required for a light pulse to travel from the transmitter to the surface and back to a receiver. This

can also be accomplished by the measurement of the relative phase of modulated received and transmitted signals. The laser radar approaches scan and effectively measure the range to each point in the image, one point at a time. Scanning is required to obtain a full frame of range image, and hence is limited in terms of speed [21]. The resolution and accuracy of time-of-flight scanners is quite limited, typically operating at 1 millimeter.

1.2.3 Structured light techniques

A structured light stereometric system is similar to a passive stereo vision system, one of the cameras is replaced by a projector [22]. By projecting certain type of patterns, the correspondence of the images can be easily identified, and depth information can be retrieved by a simple triangulation technique. This is one advantage that structured light has over stereo vision, in which the fundamentally difficult correspondence problem must be solved.

1.2.3.1 Laser scanning

Point laser triangulation uses the well-known triangulation relationship in optics. It has a typical measurement range of ± 5 to ± 250 mm, an accuracy of about 1 part in 10,000, and a measurement frequency of 40 kHz or higher [23, 24]. A Charged Couple Device (CCD), or a Position Sensitive Detector (PSD) is widely used to digitize the point laser image. CCD-based sensors avoid the beam spot reflection and stray light effects and provide more accuracy because of the single pixel resolution. For a PSD the measurement accuracy is mainly dependent on the accuracy of the image on the PSD. The beam spot reflection and any stray light will also affect the measurement accuracy. Another factor that affects the measurement accuracy is the difference in the surface characteristic of the measured object from the calibration surface. Usually calibration should be performed on similar surfaces to ensure the measurement accuracy. Using laser as a light source, this method has proven to be able to provide measurement at a much higher depth range than other passive systems with good discrimination of noise factors. However, this point-by-point mea-

surement technique is very slow. In order to increase the speed, techniques based on single laser line scanning have been developed. In these techniques, a laser line is usually swept across the object. A CCD array images the reflected light, and depth information is reconstructed by triangulation. This technique can give very accurate 3D information for a rigid body even with a large depth.

However, this method is time consuming for real measurement since it obtains 3D geometry a point or a line at a time. Area scanning based method is certainly faster.

1.2.3.2 Binary coding

Binary coding is one of the most well-known techniques which extracts depth information by projecting multiple binary coded structured light patterns [25, 26]. In these technique, only two illumination levels, coded as 0 and 1, are commonly used. Every pixel of the pattern has its own codeword formed by 0's and 1's corresponding to its value in every projected pattern; thus the codeword is obtained once the sequence is completed. 3D information can be retrieved based on decoding the codeword. Since only 0's and 1's are used in this method, it is robust to noise. However, the resolution cannot be high since the stripe width must be larger than 1 pixel. In order to increase resolution more patterns need to be used, which increases the acquisition time. In general this method is not suitable for high-resolution real-time measurement.

1.2.3.3 Multi-level gray coding

To reduce the number of required fringe patterns, some techniques that use more intensity levels to code the patterns have been proposed [27]. Pan *et al.* generalized the binary coding method to use N-ary code [28]. Binary code is a special case of N-ary code when N equals to 2. Caspi *et al.* developed a color N-ary gray code for range sensing, in which the number of fringe patterns, M , and the number of intensity levels, N_i , in each individual color channel, are automatically adapted to the environment [29]. Horn and Kiryati provided an optimal design for generating the

N-ary code with the smallest set of projection patterns that meets the application-specific accuracy requirements given the noise level in the system [30]. The above two techniques significantly reduced the number of fringe patterns by adopting N-ary codes; however, they required one or two additional uniform illumination references to generate the individual threshold for each pixel to achieve high resolution. The extreme case of N-ary structured light is to use all the gray levels, which leads to the intensity ratio method for 3D shape measurement.

1.2.3.4 Intensity ratio

Codification based on linear changing gray levels, or the so-called intensity-ratio method, has the advantage of a fast processing speed because it requires only a simple intensity-ratio calculation. Usually two patterns, a ramp pattern and a uniform bright pattern, are used. Depth information is extracted from the ratio map based on triangulation [31, 32]. However, this simple technique is highly sensitive to camera noise and image defocus. To reduce measurement noise, Chazan and Kiryati proposed a pyramidal intensity-ratio method, which combines this technique with the concept of hierarchical stripes [33]. Later Horn and Kiryati developed piecewise linear patterns in an attempt to optimize the design of projection patterns for best accuracy [30]. To eliminate the effect of illumination variation, Savarese *et al.* developed an algorithm that used three patterns [34]. However, this technique is still very sensitive to camera noise and image defocus. Moreover, its resolution is low unless periodical patterns are used, which then introduces the ambiguity problem.

1.2.4 Wave optics-based techniques

In nature, light propagates in the form of electromagnetic waves. By analyzing the interference fringe pattern of two waves, the depth information can be obtained. Among the existing techniques, optical interferometry, Moiré contouring methods are well studied.

1.2.4.1 Optical interferometry

The idea behind interferometric shape measurement is that fringes are formed by variation of the sensitivity matrix that relates the geometric shape of an object to the measured optical phases. The matrix contains three variables: wavelength, illumination and observation directions, from which three methods, namely, two- or multiple-wavelength [35, 36, 37]; refractive index change [38, 39, 40]; and illumination direction variation/two sources methods, are derived [41, 42, 43]. The resolution of the two-wavelength method depends on the equivalent wavelength (Λ) and the phase resolution of $\Lambda/200$. Another range measurement technique with high accuracy is double heterodyne interferometry, which uses a frequency shift.

Interferometric methods have the advantage of being mono-state without the shading problem of triangulation techniques. Combined with phase-shifting analysis, interferometric methods and heterodyne techniques can have accuracies of 1/100 and 1/1000 of a fringe, respectively [44].

1.2.4.2 Moiré contouring

Moiré fringe is generated by shooting light onto two gratings that lie in contact with a small angle between the grating lines. The mathematical description of Moiré fringe (patterns) resulting from the superposition of sinusoidal gratings is the same as for interference patterns formed by electromagnetic waves. The Moiré effect is therefore often termed as mechanical interference. The main difference lies in wavelength difference which constitutes a factor of approximate 10^2 and greater.

Traditional Moiré interferometries obtain depth information only from the peak and valley of the Moiré fringes [45, 46, 47] and abandon other valuable information. Phase measuring methods started to be applied to Moiré in the 1970's [48, 49, 50, 51, 52]. These methods greatly improved the resolution, accuracy, and repeatability of early Moiré technologies. The typical measurement range of phase shifting Moiré methods is from 1 mm to 0.5 m with a resolution at 1/10 to 1/100 of a fringe [53]. Moiré method has the primary advantage of fast measurement speed due to the fact that it does not need to scan over the entire surface of the object. Also the image

processing for retrieving 3D contour information is relatively straightforward.

Moiré contouring techniques include shadow and projection Moiré. The shadow Moiré method has the merit of easiness in acquiring quantitative contour information from the Moiré patterns. However it is usually difficult to use it for the contouring of large objects. Projection Moiré can handle large objects and accommodate phase-shifting techniques for enhanced measurement resolution. Their primary limitation is the tedium associated with obtaining quantitative height information and the requirements of additional actuators and controls if the phase shifting technique is used.

Analyzing interference fringes especially analyzing phase can give very accurate 3D geometric information. If this technique is combined with digital technologies, it provides dramatic advantages over other optical metrology methods. This technique is called digital fringe projection.

1.2.4.3 Digital fringe projection

Digital fringe projection is a technique that takes advantage of digital projection technology and the phase analysis of fringe images. The fringe patterns are generated by a computer, projected through a digital display device such as Digital-Light-Processing (DLP) projector or Liquid-Crystal-Display (LCD) projector onto the object being measured. 3D information can be retrieved accurately by phase analysis. This method is called *digital fringe projection* method. The primary advantages of digital fringe projection technology are: first, different shapes of patterns can be generated easily; second, the shape of the patterns can be accurately controlled by software; and third, the errors caused by mechanical devices for phase shifting are eliminated.

Fringe projection can be regarded as a type of projection Moiré [54, 55, 56]. However, traditional fringe projection techniques or Moiré interferometry techniques do not have the flexibility of changing fringe shape and size and the fringe patterns cannot be accurately generated as specified. Fringe projection method can also be regarded as a structure light method if the projected sinusoidal fringe images are

regarded as structured light patterns.

With all these 3D shape measurement techniques and the advance of digital technology, real-time 3D shape acquisition, reconstruction, and display becomes increasingly possible. The question is which technique is most suitable for real-time measurement.

1.2.5 Real-time techniques

Real-time 3D shape measurement is increasingly being pursued with the continuous development of digital technologies. For all these real-time methods, there are basically two approaches: one is to use a single pattern, typically a color pattern; the other is to use multiple patterns but switch them rapidly.

Several techniques have been developed based on single pattern method. Harding proposed a color-encoded Moiré technique for high-speed 3D surface contour retrieval [57]. Geng developed a rainbow 3D camera for high-speed 3D vision [58]. Wust and Capson [59] proposed a color fringe projection method for surface topography measurement with the color fringe pattern printed on a color transparency film. Huang *et al.* [60] implemented a similar concept but with the color fringe pattern produced digitally by a DLP projector. Zhang *et al.* developed a color structured light technique for high-speed scans of moving objects [61]. Since the above methods use color to code the patterns, the shape acquisition result is affected to various degrees by the variations of the object's surface color. On the contrary, Takeda and Mutoh proposed 3D shape measuring method based on Fourier transform [62]. This method uses a single monochromatic fringe image to reconstruct 3D geometry through Fourier transform. The limitation of this method lies in the requirement that the geometric surface must be smooth, otherwise the reconstructed geometry will have larger error. In general, the more patterns that are used in a structured light system, the better accuracy can be achieved. Therefore, the above methods sacrifice accuracy for improved acquisition speed.

The other approach for real-time 3D shape acquisition is to use multiple patterns but switch them rapidly so that they can be captured in a short period of

time. Rusinkiewicz *et al.* [63] and Hall-Holf and Rusinkiewicz [64] developed a real-time 3D model acquisition system that uses four patterns coded with stripe boundary codes. The acquisition speed achieved was 15 frame per second (or pseudo 60 Hz), which is good enough for scanning slowly moving objects. However, like any other binary-coding method, the spatial resolution of these methods is relatively low because the stripe width must be larger than one pixel. Moreover, switching the patterns by repeatedly loading patterns to the projector limits the switching speed of the patterns and therefore the speed of shape acquisition. Huang *et al.* recently proposed a high-speed 3D shape measurement technique based on a rapid phase-shifting technique [65]. This technique uses three phase-shifted, sinusoidal gray scale fringe patterns to provide pixel-level resolution.

Since only three images are required to reconstruct pixel-level resolution 3D geometry, the three-step phase-shifting algorithm is certainly desirable for this research. Therefore, in this research, we mainly uses three-step phase-shifting algorithm for real-time 3D shape measurement.

1.3 Objectives

High-resolution, real-time 3D measurement is highly needed and has huge potentials in many applications. Due to the very challenging nature of developing a high-resolution, real-time 3D shape measurement system, so far no system with such capability has ever been developed. The objective of this dissertation research is to develop such a system and demonstrate its potential values in various applications. In particular, our focus is on the following:

- Develop a system to acquire, reconstruct, and display high-resolution 3D information of the measured objects in real time.
- Develop novel phase-shifting algorithms for 3D shape reconstruction in real time.
- Develop error compensation methods to improve 3D measurement accuracy.

- Develop a systematic method to calibrate the 3D measurement system accurately and quickly.

1.4 Dissertation Structures

In this dissertation, Chapter 2 introduces the basics of DLP technology, overviews phase-shifting algorithms, and discusses a simple system setup of 3D shape measurement system using a DLP projector based on a phase-shifting method.

In order to realize real-time 3D shape acquisition, an advanced hardware system has to be built. In Chapter 3, we discuss the development of this hardware system. The system we develop is based on a digital fringe projection and phase-shifting technique. It utilizes a DLP projector to project computer generated fringe patterns to the object and a high-speed CCD camera synchronized with the projector to acquire the fringe images at a frame rate of 120 frames per second. Based on a phase-shifting technique, each frame of the 3D shape of the object is reconstructed using three consecutive fringe images. For real-time 3D reconstruction, a novel fast phase-wrapping algorithm is developed, which significantly reduces the processing time of the fringe images. Parallel processing software is also developed to achieve simultaneous 3D data acquisition, reconstruction, and display. As a result, high-resolution, real-time 3D shape measurement is realized at a frame rate of up to 40 frames per second and a resolution of 532×500 points per frame.

Real-time 3D reconstruction is the second challenging topic. In Chapter 4, we propose a novel method called trapezoidal phase-shifting method. Instead of calculating the phase by using the arctangent function, we calculate a simple intensity ratio which is much faster. Experiments demonstrated that the new algorithm allows for 3D shape reconstruction speed of 40 frames per second with an ordinary personal computer at pixel level with an ordinary personal computer. The drawback of trapezoidal phase-shifting method lies in its sensitivity to image defocusing, which limits the dynamic range of measurement.

In Chapter 5, we introduce a fast phase-wrapping algorithm, which uses the algorithm of the trapezoidal phase-shifting method to process phase-shifted sinusoidal

patterns. The reconstructed geometry has similar accuracy as that obtained by the traditional phase-wrapping algorithm, but its processing speed improves at least 3.4 times faster. This new algorithm combines the advantages of the trapezoidal phase-shifting and traditional sinusoidal phase-shifting algorithms; it has the fast processing speed of the trapezoidal method and the high measurement accuracy of the traditional sinusoidal method.

In the phase-shifting method we use, the non-sinusoidal nature of the fringe patterns due to projector nonlinearity is the major error source. In this Chapter 6, we propose a novel error compensation method, which can theoretically completely eliminate errors due to non-sinusoidal fringes. Moreover, a method is also proposed to correct the non-sinusoidality of the fringe patterns, which makes the high-quality texture mapping becomes possible.

System calibration, which usually involves complicated time-consuming procedures, is crucial for any 3D shape measurement system. In Chapter 7, a novel approach is proposed for accurate and quick system calibration. In particular, a new method is developed which enables a projector to “capture” images like a camera, thus making the calibration of a projector the same as that of a camera. This is a significant development because today projectors are increasingly used in various measurement systems and yet so far no systematic way of calibrating them has been developed. Our experimental results demonstrate that the measurement accuracy of our system after calibration is less than RMS 0.22 mm over a volume of $342 \times 376 \times 658$ mm.

Chapter 8 summarizes the contributions of this research and proposes future works.

Chapter 2

3D Shape Measurement Based on Digital Fringe Projection Techniques

With the rapid development of digital technologies, many optical 3D shape measurement techniques using digital video projectors have been developed. Digital-light-processing (DLP) technology plays an important role in the development of these techniques. In this chapter, Section 2.1 introduces the basics of DLP technology, Section 2.2 discusses phase-shifting algorithms, Section 2.3 gives a typical 3D measurement system using a digital fringe projection and phase-shifting method, and Section 2.4 summarizes the chapter.

2.1 Digital Micro-mirror Devices (DMD) and DLP Projectors

The DLP concept originated from Texas Instruments(TI) in the later 1980's. In 1996, TI commercialized its first generation of DLP projectors. DLP projectors fundamentally have many advantages over LCD projectors due to digital nature of DLP. The core of DLP technology is an optical switch called DMD [66, 67]. DMD consists of an array of tiny mirrors, each operating in a bistable mode, tilting diagonally $+\theta$ degrees (ON) or $-\theta$ degrees (OFF) about the hinge attached to the support post. Each microscopic mirror corresponds to one pixel of the light in a projected image. By switching these mirrors ON and OFF up to several thousand times per second, a DLP projection system can translate a digital video or graphic source into a projected image with maximum fidelity. The proportion of time during each video frame that a micromirror remains ON determines that shade of pixel gray scale from

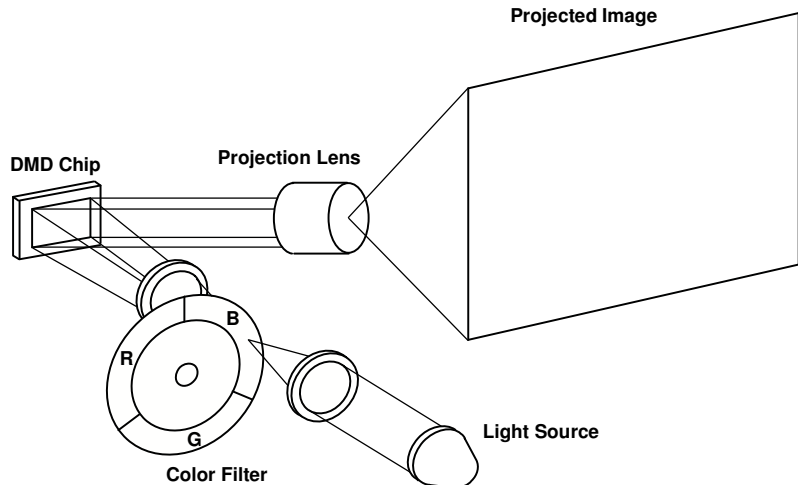


Figure 2.1: Single-chip DLP projection system configuration.

black for 0% ON-time to white for 100% ON-time.

Figure 2.1 shows the configuration of a DLP projector with one DMD chip. The light from the illuminator is first focused to a small spot on the color filter. The color filter spins at high speed producing red, green and blue light sequentially that illuminates the DMD surface. The image to be projected is formed on the DMD chip. Since there is only one DMD chip in the projector, but a 24-bit color image is to be projected, the projector operates in a unique color-channel-switching mode. At one specific moment only one channel of the color image, red, green, or blue, is projected and the three color channels are projected in sequence. A photodiode mounted on the cover of the DMD projection engine monitors the position of the color filter, and provides a timing signal to the projector. Based on this signal, the DMD forms the image of the corresponding color channel. Since the color channels are switched at high speed, what the viewer sees is a 24-bit color image.

For a single-chip DLP projection system, the color filter functions as the “color” generator. The color filter usually contains three or six color segments for sequentially separating red, green, and blue wavelengths. Typically, a white (or clear) segment, which is usually a section of anti-reflection coated glass, is added to boost the brightness of the projected image. The four segments (red, green, blue and clear) of the color wheel do not distribute uniformly. Usually the red segment is the largest and

the white one is the smallest, which is used to balance the projected color channels. In comparison with Cathode-Ray Tube (CRT) or LCD displays, DLP displays have their own advantages because they are inherently digital.

- *High image quality.* Each DMD device includes up to 1.3 million individually hinge-mounted microscopic mirrors. Its projection image is film-like or video with photographic quality. Since the image produced by DLP projectors is the exact mirror image of its source material, it comes closer than any other display solution to reproduce the source image.
- *Large color range.* DLP technology reproduces a range of color up to eight times greater than that of analog projection systems. DLP projection creates rich blacks and darker shades than is possible with other technologies and projects no fewer than 35 trillion colors over eight times more than what is possible with film.
- *Long operation hours.* It has been demonstrated that DLP projectors can work reliably over 100,000 operation hours and more than 1 trillion mirror cycles. They are reliable enough and their life expectancy is long enough for the ordinary users.
- *Inherent noise immune.* With all-digital displays, users can watch without ground-loop noise or electromagnetic interference from household appliance or local radiation sources.

Unique new features are only possible with digital view processing in the display. Its digital nature matches well with today's surge in computer graphics display. In summary, DLP projection display technology offers exceptional flexibility, high brightness, high resolution, and high image quality. DLP projectors enable us to generate fringe patterns easily and accurately, which is one of the key factors of our high-speed and high-resolution 3D measurement research.

2.2 Phase Shifting Interferometry

The single largest change in all types of instrumentation over the past decades has been the integration of computers into the measurement system. Phase Shifting Interferometry (PSI) is not a specific optical hardware configuration but rather a data collection and analysis method that can be applied to a great variety of testing situations. Although computerization benefits the analysis of the static interferograms, it suffers from the need of finding fringe centers and the resulting tradeoff between precision and number of data points.

PSI recovers phase by a pixel-by-pixel calculation of a series of wavefront phase encoded interferograms. The need to locate the fringe centers and its associated problems are eliminated. Over the years, the applications of phase measurement have been extensively used in optical testing, real-time wavefront sensing for active optics, distance measuring interferometry, surface contouring, and microscopy, etc.

2.2.1 Fundamental concepts

The basic concept behind phase shifting interferometry is that a time-varying phase shift is introduced between the reference wavefront and the test or sample wavefront in the interferometers. A time varying signal is then produced at each measurement point in the interferogram, and the relative phase between the two wavefronts at that location is encoded in these signals.

From physical optics, the wavefront of a light source is

$$w(x, y, t) = a(x, y)e^{i(\phi(x, y))}, \quad (2.1)$$

where x and y are spatial coordinates, $a(x, y)$ the wavefront amplitude, and $\phi(x, y) = 4\pi h(x, y)/\lambda$ the wavefront phase. Here λ is the wavelength, $h(x, y)$ the surface height errors tested in reflection.

General expressions for the reference and test wavefronts in the interferometer are,

$$w_r(x, y, t) = a_r(x, y)e^{i(\phi_r(x, y) - \delta(t))}, \quad (2.2)$$

and

$$w_t(x, y, t) = a_t(x, y) e^{i(\phi_t(x, y) - \delta(t))}, \quad (2.3)$$

respectively, where $a_r(x, y)$ and $a_t(x, y)$ are the wavefront amplitudes, $\phi_r(x, y)$ and $\phi_t(x, y)$ the wavefront phases, and $\delta(t)$ the time-varying phase shift. When the reference and test wavefront interfere with each other, the resultant intensity pattern is:

$$I(x, y, t) = |w_r(x, y, t) + w_t(x, y, t)|^2, \quad (2.4)$$

or

$$I(x, y, t) = I'(x, y) + I''(x, y) \cos [\phi_t(x, y) - \phi_r(x, y) + \delta(t)], \quad (2.5)$$

where $I'(x, y) = a_r^2(x, y) + a_t^2(x, y)$ is the average intensity, and $I''(x, y) = 2a_r(x, y)a_t(x, y)$ is the fringe or intensity modulation. If we define the phase difference as $\phi(x, y) = \phi_t(x, y) - \phi_r(x, y)$, then we obtain the fundamental equation of phase shifting:

$$I(x, y, t) = I'(x, y) + I''(x, y) \cos [\phi(x, y) + \delta(t)], \quad (2.6)$$

where $\delta(t)$ is the time-varying phase shift, $I'(x, y)$ the intensity bias, $I''(x, y)$ half of the peak-to-valley intensity modulation, and $\phi(x, y)$ is the unknown phase related to the temporal phase shift of this sinusoidal variation. The wavefront phase at this location can be easily computed from this temporal delay. The entire map of the unknown wavefront phase $\phi(x, y)$ can be measured by monitoring and comparing this temporal delay at all the required measurement points.

Figure 2.2 illustrates interference patterns formed by two coherent light sources on a plane and on a complicated surface. In Figures 2.2(a) and 2.2(b), the light sources are point lights; and in Figures 2.2(c) and 2.2(d), the light sources are at infinity, which are plane waves.

2.2.2 Fringe projection

Figure 2.2(c) and 2.2(d) illustrate the interference pattern caused by parallel planar light waves. That can be obtained equivalently by orthographically projecting a regular sinusoidal fringe pattern onto the object surface in a direction parallel

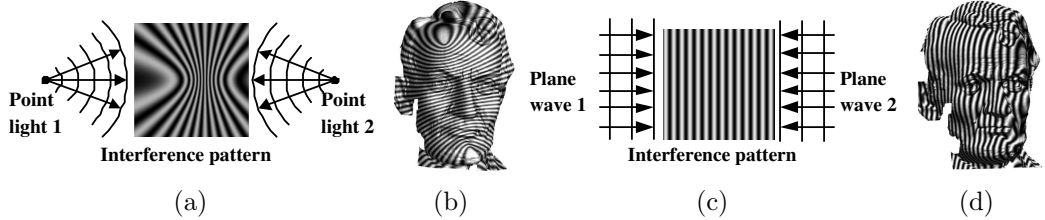


Figure 2.2: Principle of interference. (a)-(b) fringe patterns generated by the interference of two coherent point sources.(c)-(d) Fringe pattern generated by the interference of two coherent parallel planar light waves.

to the light source planes. For example, the fringes on the Lincoln head surface introduced by the interference of two parallel planar light waves can also be obtained by projecting the fringes directly to the surface in a direction parallel to the light planes.

We assume two planar light sources are at $x = \pm c$ and the wave propagation directions are $(\mp 1, 0, 0)$ respectively. Then the waves can be described as

$$u_1 = U e^{i \frac{2\pi}{\lambda} (x - c)}, \quad (2.7)$$

$$u_2 = U e^{-i \frac{2\pi}{\lambda} (x - c)}, \quad (2.8)$$

The interference wave is simply

$$u = u_1 + u_2 = 2U \cos \frac{2\pi}{\lambda} (x - c). \quad (2.9)$$

The intensity of the interfering light is

$$I = 2U^2 \{\cos[4\pi(x - c)/\lambda] + 1\}. \quad (2.10)$$

The fringe pattern can be obtained by projecting a planar light onto the surface directly along the z -axis, with intensity given by the above equation.

Thus, instead of making coherent light waves interfere on the test surface, the interference fringe pattern can be projected directly to the surface and viewed from a different angle by a camera. This method is called *fringe projection*.

Note that for real measurement, the interference fringe images are always generated by two planar light sources at an angle less than 180 degrees to illuminate the object. We used 180 degrees for simplicity.

2.2.3 Three-step phase-shifting algorithms

Over the years a number of phase-shifting algorithms have been developed and applied to real measurement applications, including three-step algorithms, least-square algorithms etc [68]. All of these algorithms share common characteristics, they require that a series of fringe images are recorded as the reference phase is varied. Differences between the various algorithms relate to the number of recorded fringe images, the phase shift between fringe images, and the susceptibility of the algorithm to errors in the phase shift or environmental noise such as vibration and turbulence. This section discusses the three-step phase-shifting algorithm that is used in this research.

Since there are three unknowns in Equation 2.6, the minimum number of measurements of the fringe images that are required to reconstruct the unknown wave-front phase is three. Equal phase steps of size α is usually used in the three-step algorithm. That is

$$\delta_k = -\alpha, 0, \alpha; \quad k = 1, 2, 3,$$

and

$$\begin{aligned} I_k(x, y) &= I'(x, y) + I''(x, y) \cos [\phi(x, y) + \delta_k], \\ &= I'(x, y) \{1 + \gamma(x, y) \cos [\phi(x, y) + \delta_k]\}, \end{aligned} \quad (2.11)$$

where $I'(x, y)$ is the average intensity, $I''(x, y)$ the intensity modulation or the dynamic range of the encoded fringe, and $\phi(x, y)$ the phase to be determined, and $\gamma(x, y) = I''(x, y)/I'(x, y)$ the data modulation. If phase shift is $\alpha = 2\pi/3$, solving Equations 2.11 gives,

$$\phi(x, y) = \tan^{-1} \left(\sqrt{3} \frac{I_1 - I_3}{2I_2 - I_1 - I_3} \right), \quad (2.12)$$

$$I'(x, y) = (I_1 + I_2 + I_3)/3, \quad (2.13)$$

$$\gamma(x, y) = \frac{I''(x, y)}{I'(x, y)} = \frac{\sqrt{3(I_1 - I_3)^2 + (2I_2 - I_1 - I_3)^2}}{I_1 + I_2 + I_3}. \quad (2.14)$$

The advantage of this three-step algorithm is that it requires the minimum number of three fringe patterns, which translates into high speed. The drawback of

this algorithm is its sensitivity to errors in the phase shift between frames. However, a DLP projector is utilized in this research to project computer generated phase-shifted fringe images, no phase-shift error will be introduced. Therefore, we choose this three-step phase-shifting algorithm for our real-time 3D shape system.

2.2.4 Phase unwrapping methods

Phase $\phi(x, y)$ can be recovered with ambiguity of $2k\pi$, where $k \in Z$, from fringe images using Equation 2.12. The discontinuities occur every time ϕ changes by 2π . Phase unwrapping aims to unwrap or integrate the phase along a path counting the 2π discontinuities. The key to reliable phase unwrapping is the ability to accurately detect the 2π jumps. However, for complex geometric surfaces, noisy images, and sharp changing surfaces, phase-unwrapping procedure is usually very difficult. This section introduces four basic phase unwrapping algorithms, namely, the path integration, spatial coherent, two-wavelength, and interactive phase unwrapping algorithms.

2.2.4.1 Path integration phase unwrapping

In principle, the 2π phase jump curves are special level sets of the depth function $z(x, y)$. In general, they are closed curves on the surface, or curves intersecting the boundaries or shadow or occlusion areas. The self-occlusion area is in general difficult to locate from phase map. The red curves in the first image in the second row of Figure 2.3 illustrates the phase jumping curves.

In an ideal noise-free wrapped phase image with adequately sampled data such that the phase gradients are significantly less than 2π , a simple approach to unwrap phase is adequate. All that is required is a sequential scan through the object, line by line, to integrate the phase by adding or subtracting multiples of 2π at the phase jumps.

Figure 2.3 shows the procedures of path integration phase-unwrapping algorithm. The first row from left to right shows fringe images with $-2\pi/3$, 0 , $2\pi/3$ phase shift, and wrapped phase map whose value ranges from 0 to 2π . The first

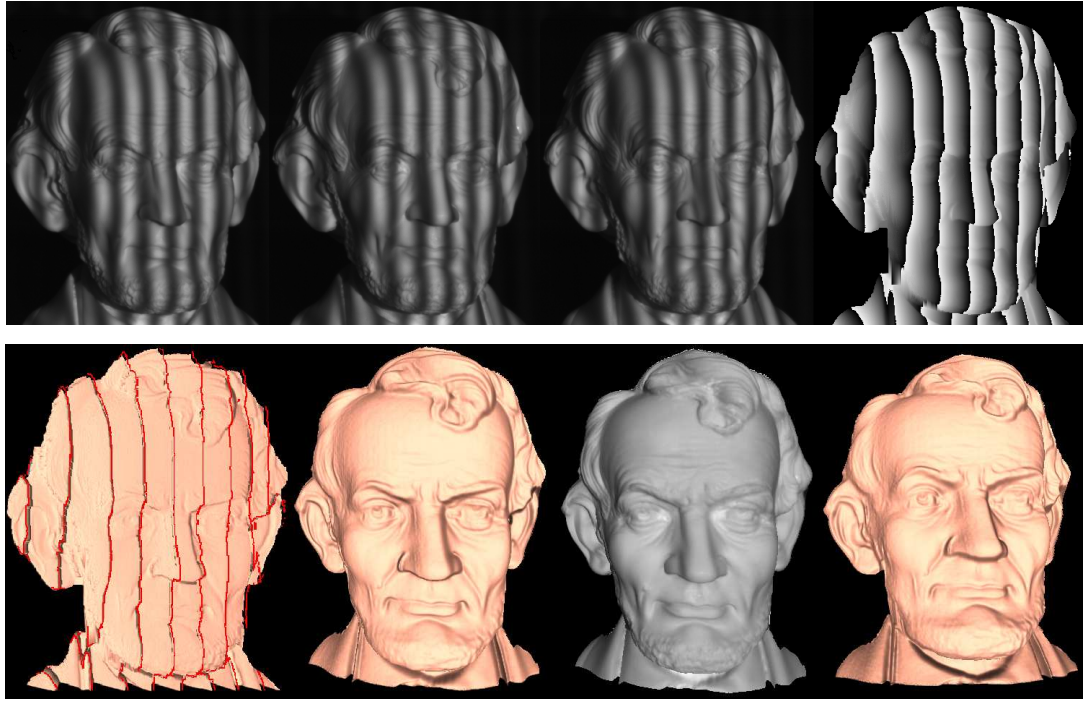


Figure 2.3: 3D result by the path integration phase unwrapping method.

image in the second row is the wrapped phase map with areas of 2π phase jumps detected (indicated in red). The second and last images illustrate the reconstructed 3D geometric model at different view angles. The third image shows the 3D model with texture mapping. Here the texture image was generated by averaging the three phase-shifted fringe images.

For most captured images, noise in the sampled data is a major contributing factor in the false identification of phase jumps. The real phase jumps will be obscured if the noise amplitude approaches 2π .

2.2.4.2 Spatial coherent phase unwrapping

Assume the wrapped phase is represented as $\psi(x, y)$. The goal is to find a smooth function $\phi(x, y)$ such that the gradient of $\phi(x, y)$ approximates the gradient of $\psi(x, y)$ as closely as possible. Thus we use the following variational approach to find a continuous function $\phi(x, y)$ that minimizes the functional,

$$J(\phi) = \int \int |\nabla \phi - \nabla \psi|^2. \quad (2.15)$$

The Euler-Langrange equation is $\Delta\phi = \Delta\psi$, where $\Delta = \frac{\partial^2}{\partial x^2} + \frac{\partial^2}{\partial y^2}$. This is a Poisson's equation and can be easily solved using either the conjugate gradient method or a Fast Fourier Transform as in Ref. [69].

The real phase jumps will be obscured in the shadow or near the self-occlusion area of the projection fringes where the projection light is tangent to the surface. The quality of each pixel in the wrapped phase map is mainly determined by two factors, namely, the phase gradient and the visibility. Pixels with low gradient and high visibility are more reliable. Therefore, we adjust our functional as

$$J(\phi) = \int \int \frac{\gamma}{1 + |\nabla\psi|^2} (|\nabla\phi - \nabla\psi|^2). \quad (2.16)$$

The functional can be converted to a weighted least square problem and solved by using the conjugate gradient method directly [70].

For surfaces with high continuity and less self-occlusion, the spatial coherent phase unwrapping algorithm works well. For surfaces with many self-occlusion regions and sharp phase gradient, phase unwrapping is more challenging. In this case, the two-wavelength phase-unwrapping algorithm can be applied.

2.2.4.3 Two-wavelength phase unwrapping

In order to remove the ambiguity of the phase, one can choose a special projection fringe such that the wavelength λ is large enough to cover the whole depth range of the scene. Thus, no phase unwrapping will be necessary at all. Unfortunately, the cost of increasing the wavelength is the decrease of the quality of the reconstructed 3D data. Therefore, one can capture two sets of fringe images with different wavelengths. The first one with a longer wavelength will remove the phase ambiguity but produce poor result. The second one will produce high quality result, but with phase ambiguity. Therefore, if we unwrap the second phase map while keeping the geometric consistency with the first one, we can obtain high quality data without the problem of phase ambiguity.

Figure 2.4 illustrates an example of 3D reconstruction employing the two-wavelength phase unwrapping algorithm. The first image is one of the fringe images

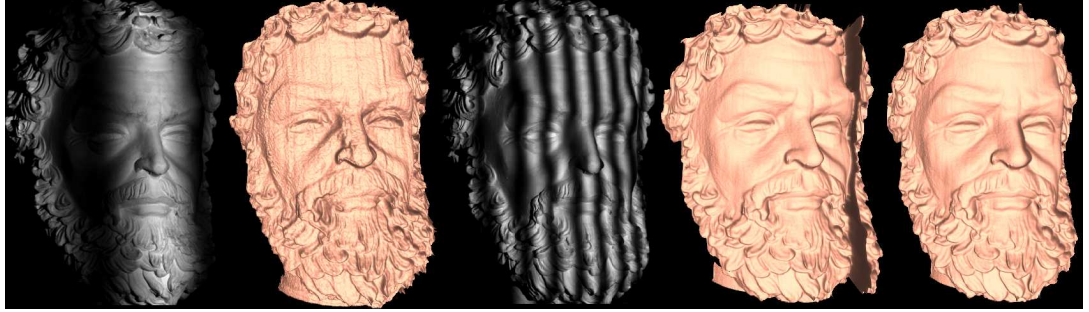


Figure 2.4: 3D reconstruction by two-wavelength phase-unwrapping algorithm.

with a longer wavelength. The geometry changes are less than 2π . Therefore, 3D information can be retrieved correctly although the quality is poor. The third image shows one of the fringe images with a shorter wavelength and the geometric changes are beyond 2π somewhere on the surface. Thus phase unwrapping cannot correctly reconstruct the geometry as illustrated in the fourth image. But with the reference of geometric information reconstructed with the longer wavelength fringe images as references, 3D shape can be correctly reconstructed as shown in the last image.

However, there are still some limitations for this method. The 2π phase ambiguity of the second phase map must be less than the phase error caused by the discretization error of the first phase map. Assume that the wavelengths are λ_1, λ_2 , and the number of bits for each pixel is n , then

$$\frac{\lambda_1}{\lambda_2} < 2^n.$$

If the depth range of the scene is very large, and the reconstructed geometry is required to be of high quality, then one can apply the multiple-wavelength phase-unwrapping algorithms.

The two-wavelength method is undesirable for high-speed data acquisition applications because it reduces the acquisition speed by half, but it is preferable for measuring static objects, especially those that would result in self-occlusions in the phase image.

2.2.4.4 Interactive phase unwrapping

For those systems that do not allow taking more images, such as our real-time system, the reconstruction procedure may require manual work. In this research, we develop an interactive Graphic User's Interface (GUI) tool that allows the user to correct those areas that have not been correctly unwrapped.

Users have the most accurate information about the quality of the reconstructed result. Therefore, if the user can communicate with the computer, providing feedback of the reconstruction result, the final phase unwrapping result will be satisfactory. In this research, we develop a GUI that allows the users to perform interactive phase unwrapping. Figure 2.5 shows the software interface of the GUI tool. The basic idea behind this tool is that the user tells the algorithm where two regions should separate. The underline phase-unwrapping algorithm is a simple path integration method. Figure 2.6 shows an example. The direct phase unwrapping resulted in geometric jumps. These jumps are due to the geometric changes beyond 2π around the regions of the little horse's mouth and the mother horse's tail. Pre-knowledge tells us that the small horse head should be separate with other areas, therefore we draw a spline (illustrated in the third image of Figure 2.6). This line tells the algorithm not to cross the line. Similarly, we draw another spline at the back. After being given these additional information, the algorithm can correctly reconstruct the 3D information of this sculpture. This special case cannot be correctly reconstructed using other algorithms without an increase in the number of fringe images. Moreover, this tool runs very fast. It can reconstruct a 3D model and render it in less than 12.5 ms, therefore the user can interactively view the effect of the operations.

2.3 Typical 3D Shape Measurement System Setup

A simple approach for 3D shape measurement is to project fringe or a grating onto an object and then view it from another direction. The deformation of the projected fringes by the object provides the information to reconstruct the shape of the 3D object.

The fringe pattern can be generated by a personal computer, projected by

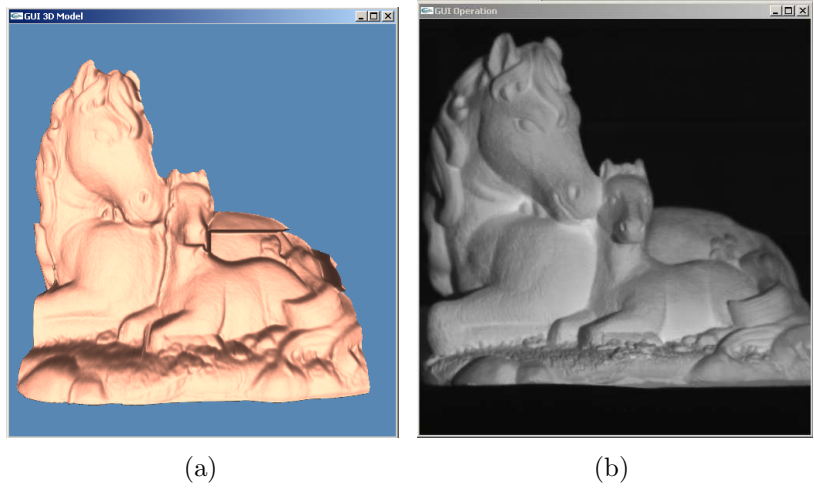


Figure 2.5: GUI interactive phase unwrapping tool. (a) Reconstructed 3D model. (b) 2D photo of the object.

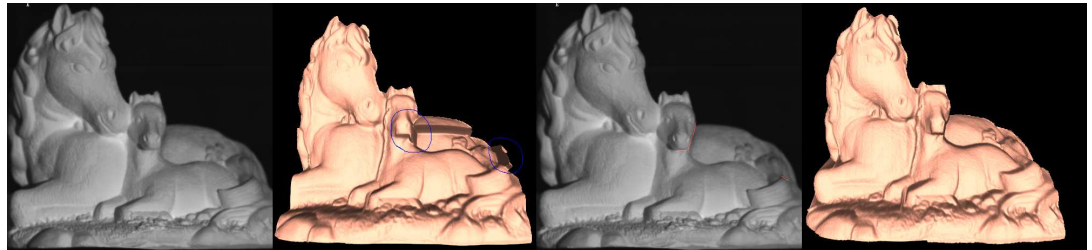


Figure 2.6: 3D reconstruction using the GUI tool. Image from left to right are: 2D photo, 3D with problems, 2D photo with spline drawn to separate regions, and corrected reconstructed 3D geometry.

a digital projector onto the object, and imaged by a camera. Software algorithm can then be applied to retrieve 3D information of the object. Figure 2.7 shows a typical system setup. A projector projects computer generated fringe patterns onto the object. The reflected light is captured by a camera. After the fringe images are captured, a phase-wrapping and -unwrapping algorithm is applied to reconstruct the 3D geometry. Figure 2.3 shows an example of measuring the sculpture of Lincoln using this simple system configuration.

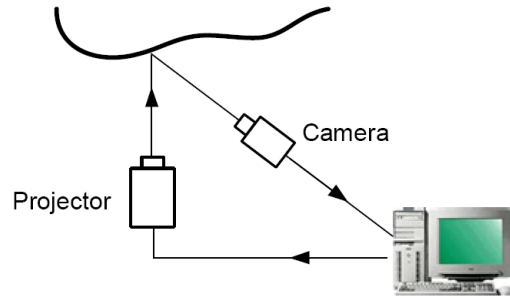


Figure 2.7: Typical 3D shape measurement system setup.

2.4 Summary

This chapter introduced the DLP digital projection display technology, reviewed three-step phase-shifting algorithm and phase-unwrapping algorithms, and finally described a basic 3D measurement system based on a digital fringe projection technique.

Chapter 3

High-resolution, Real-time 3D Shape Measurement System

This chapter describes a high-resolution, real-time 3D shape measurement system developed in this research. The system is based on a digital fringe projection and phase shifting technique. It utilizes a single-chip DLP projector to project computer generated fringe patterns to the object and a high-speed CCD camera synchronized with the projector to acquire the fringe images at a frame rate of 120 frames per second. Based on a three-step phase-shifting technique, each frame of the 3D shape of the object is reconstructed using three consecutive fringe images. A color CCD camera is also used to capture color images for color texture mapping. By implementing a novel fast phase-wrapping algorithm and parallel processing technique, we realize simultaneous 3-D data acquisition, reconstruction, and display at a frame rate of up to 40 frames per second and a resolution of 532×500 points per frame.

3.1 Introduction

To achieve real-time 3D measurement, there are basically two approaches: one is to use a single pattern (typically a color pattern), the other method is use multiple patterns and switch them rapidly so that images required for reconstructing the 3D geometry can be captured in a short period of time. In this research, we adopted the second approach. Three phase-shifted fringe patterns are encoded in the three primary color channels and projected by a single-chip DLP projector in sequence at a frame rate of 80 Hz. A properly synchronized high-speed B/W CCD camera is used to capture the distorted fringe patterns in real time. In order to achieve more

realistic visual effect, a color camera synchronized with the B/W camera is used to provide color images for texture mapping.

The rest of this chapter is organized as follows. Section 3.2 explains the basic principle of this high-resolution, high-speed 3D shape measurement system. Section 3.3 introduces the system setup. Section 3.4 describes a system that is able to capture color photo simultaneously. Section 3.5 introduces a new system that gives high quality data stably. Section 3.6 presents the framework of simultaneously data acquisition, reconstruction and display. Section 3.7 discusses the advantages and disadvantages of this real-time system. And Section 3.8 summarizes the chapter.

3.2 Principle

3.2.1 Projection mechanism of a single-chip DLP projector

One of the keys to successfully developing this real-time system is to understand the projection mechanism of a single-chip DLP projector. In this research, a commercial Kodak DP900 projector is extensively studied. For the DLP projector, a photodiode behind the color wheel supplies a trigger signal to the DMD to generate images. However, since color is not desired in this research, the color filters are removed. As a result, the photo sensor cannot detect the color signal and supply the trigger signal to DMD, which disables the projector from projecting images. Figure 3.1(a) shows the position of the photo-detector, Figure 3.1(b) shows the commercial projector with the color filters while Figure 3.1(c) shows the modified projector without the color filters. To make the projector work without the color filters, Zhang found an approach by supplying the projector with an externally generated 2-level current signal to replace the trigger signal from the photo sensor [71]. Some experiments were done and reasonable results were obtained.

However, in this research, we find that the projector could not work stably if it is triggered by the 2-level current signal. After operating for a while, the projector flashes and starts to project images improperly. To improve the stability of the projector, a parallel input 12-bit D/A converter is utilized to generate a 2-level voltage signal, 10 mv at the low level and 56 mv at the high level, respectively. We

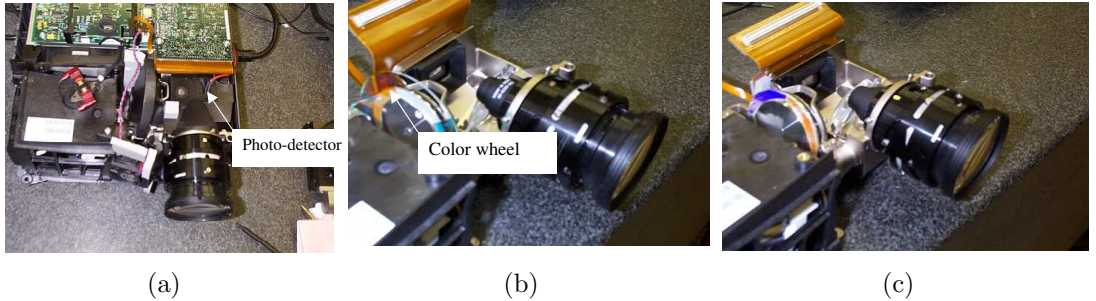


Figure 3.1: DLP projector and color filters. (a) Projector with photo sensor. (b) Projector with color filters. (c) Projector without color filters.

also notice that the projector always starts projecting images at the falling edge of the trigger signal and projects red, clear (white), green, and blue channels sequentially when the trigger signal has a period longer than 10 ms. After repeated experiments, we find the optimal trigger signal period to be 12.5 ms, at which the projector works most stably.

3.2.2 System synchronization

After fully understanding the projection mechanism of the single-chip DLP projector, it is possible to take advantage of it to boost the 3D measurement speed. Three phase-shifted fringe images are encoded in three the primary color channels (RGB) of the projector. Since the color filters are removed, the projector projects three phase-shifted gray scale fringe images sequentially and repeatedly at a high speed when the RGB fringe image is sent to the projector. If a high-speed camera synchronized with the projector is used, three fringe images can be captured rapidly for real-time 3D shape measurement.

Figure 3.2 shows the timing chart of our system. The waveform at the top is the trigger signal to the projector. The projector's trigger signal is generated by an external micro-controller based timing signal circuit. The internal timing signal of the projector is disabled. The middle waveform is the projection timing chart, where R, G, B, and C represent the red, green, blue, and clear channels of the projector. The clear channel is designed to enhance the brightness of the projected image. The projection signal shows the sequence and timing of the color channels.

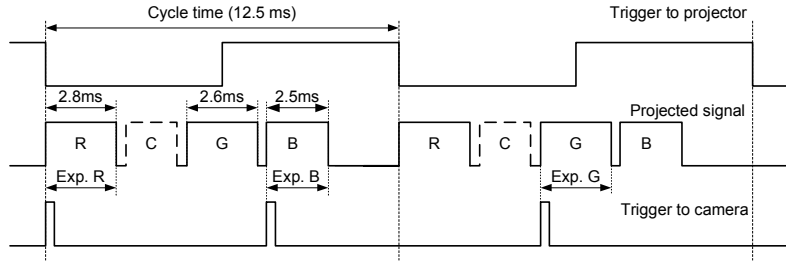


Figure 3.2: System timing chart.

The projection cycle starts with the red channel at the falling edge of the projector trigger signal. The bottom waveform is the trigger signal to the B/W CCD camera. The camera's trigger signal is generated by the same micro-controller based circuit, which guarantees its synchronization with the projector's trigger signal. Because of the limitation of the frame rate of our camera (maximum of 262 frames per second), two cycles of projection are needed for the camera to capture the three phase-shifted fringe patterns, which results in a frame rate of 40 frames per second for 3D data acquisition. If a higher speed camera is used, a maximum frame rate of 80 Hz can be achieved.

The non-uniform distribution of three color channels of the projector can potentially affect the measurement accuracy. We observe that the RGB channels do not have the same duration time (red is approximately 2.8 ms and blue is approximately 2.5 ms). For this real-time system, the exposure time of the camera could not be adjusted according to each individual frame. To solve this problem, we set the exposure time at a fixed time of 2.8 ms for all channels and take advantage of the 0.2 ms gaps between channels to make sure that all channels are captured properly, as shown in Figure 3.3. One should notice that with this timing design, only the red channel is truly synchronized. The green and blue channels are pseudo synchronized.

3.2.3 Color-encoded three-step phase-shifting algorithm

As introduced in Chapter 2, three-step phase-shifting algorithm requires minimum number of fringe images to reconstruct 3D shape. In general, the three color encoded fringe images with a phase shift of $2\pi/3$ generated by a computer are, re-

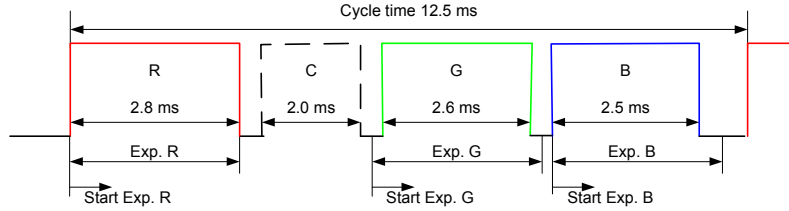


Figure 3.3: System synchronization timing chart.

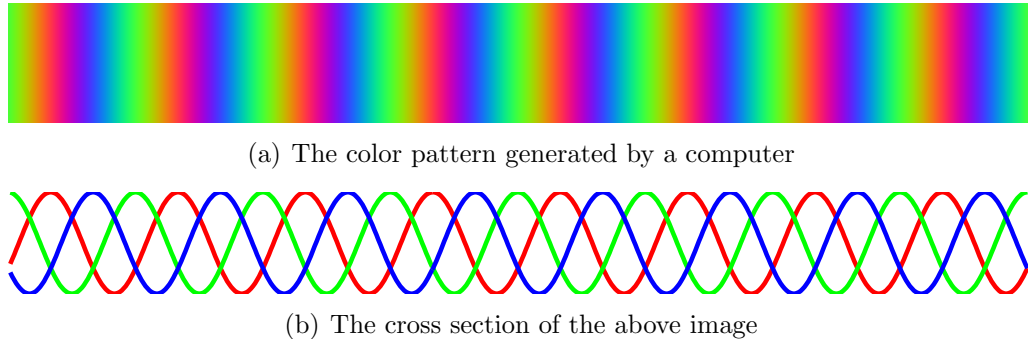


Figure 3.4: Color encoded sinusoidal fringe pattern.

spectively,

$$I_r(x, y) = b \left[1 + \cos \left(\frac{2\pi}{p}x - \frac{2\pi}{3} \right) \right] + a , \quad (3.1)$$

$$I_g(x, y) = b \left[1 + \cos \left(\frac{2\pi}{p}x \right) \right] + a , \quad (3.2)$$

$$I_b(x, y) = b \left[1 + \cos \left(\frac{2\pi}{p}x + \frac{2\pi}{3} \right) \right] + a . \quad (3.3)$$

where a is the bias, b the amplitude of the fringe images, and p the fringe pitch. The color fringe image and its cross section are illustrated in Figure 3.4. When captured by a camera, the fringe patterns have the intensities as,

$$I_r(x, y) = I'(x, y) + I''(x, y) \cos \left[\phi(x, y) - \frac{2\pi}{3} \right] , \quad (3.4)$$

$$I_g(x, y) = I'(x, y) + I''(x, y) \cos [\phi(x, y)] , \quad (3.5)$$

$$I_b(x, y) = I'(x, y) + I''(x, y) \cos \left[\phi(x, y) + \frac{2\pi}{3} \right] . \quad (3.6)$$

Where $I'(x, y)$ the average intensity, $I''(x, y)$ the intensity modulation, and $\phi(x, y)$ the phase to be determined. Phase $\phi(x, y)$ and data modulation $\gamma(x, y)$ (in Equa-

tions 2.12 and 2.14) respectively become,

$$\phi(x, y) = \arctan \left(\sqrt{3} \frac{I_r - I_b}{2I_g - I_r - I_b} \right), \quad (3.7)$$

and

$$\gamma(x, y) = \frac{I''(x, y)}{I'(x, y)} = \frac{\sqrt{3(I_r - I_b)^2 + (2I_g - I_r - I_b)^2}}{I_r + I_g + I_b}. \quad (3.8)$$

A phase map with the phase ranging from 0 to 2π is obtained after this step. A continuous phase map can be obtained by phase unwrapping (see Section 2.2.4).

3.2.4 Projection nonlinearity correction

The accuracy of the phase measurement can be improved by reducing systematic errors of the system. In phase shifting interferometry [72], the most common sources of systematic errors include nonsinusoidal waveforms of a signal due to multiple-beam interference or nonlinearity of the detector and phase-shift errors due to a miscalibration or nonlinear projection response of the phase shifter. In our system, the dominant error source is nonsinusoidal waveforms due to the nonlinear projection curve (or gamma curve) of the projector. This nonlinear projection response makes the intensity profile of the fringe images nonsinusoidal and therefore causes phase measurement errors. Phase shifting error in our system is negligible because of the digital nature of the fringe generation technique.

The projection response curve of a commercial video projector, which represents the relationship between the input gray scale values generated by the computer and the output intensity values projected by the projector and captured by the camera, is typically designed to be nonlinear for better visual effects. Figure 3.5(a) shows a typical projection response curves of the Kodak DP900 projector obtained experimentally. The projected intensity is measured by the CCD camera. Notice that when the input gray scale value is less than approximately 45, the projected intensity value almost does not change. This part of the input gray scale value is therefore not used in our experiment. In our experiment, we adjust the brightness, contrast, and tint of the projector to make the projection response curves for the three color channels

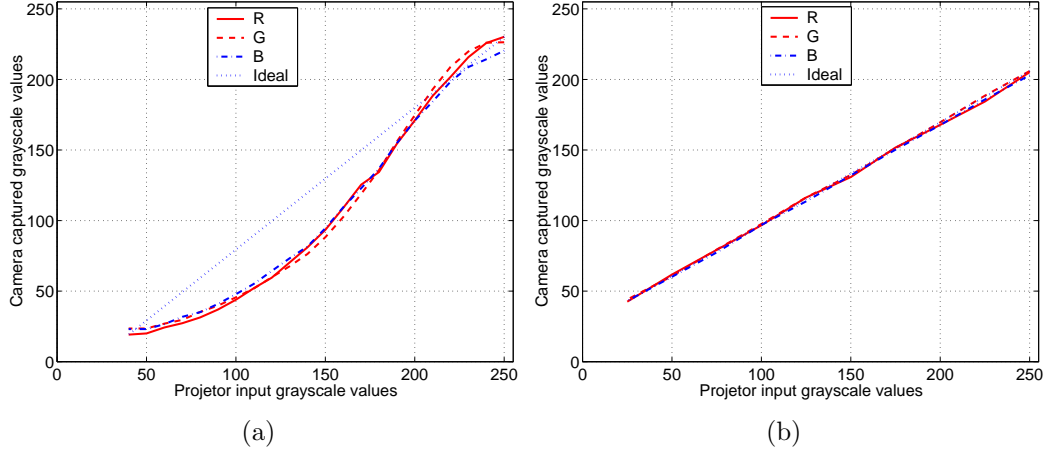


Figure 3.5: System projection response curve. (a) The curves before nonlinearity compensation. (b) The curves after compensation.

to be as close to each other as possible and their nonlinearity as small as possible before nonlinearity correction is performed.

To compensate for the nonlinearity of the projector, the projection response curves are fitted with spline, whose inverse functions are then used to modify the input gray scale values of the fringe images generated by the computer. Figure 3.5(b) shows the projection response curves after nonlinearity correction, which are almost linear.

This method provides fairly good measurement accuracy, however, the shortcoming is obvious. However, no matter how careful the calibration is done, the projection response curve could never be truly linear, which causes residue errors. In Chapter 6, we will discuss another error compensation method that further improves the accuracy.

3.2.5 Coordinate conversion

The measured phase contains the height information of the measured object, which can be extracted by using a phase-to-height conversion algorithm. Since in this real-time system, we are more interested in the relative height variations on an object surface than absolute coordinates, a simple approximate approach by subtracting reference plane is employed [48].

In order to convert phase to height, the relationship between the height and phase has to be established. The schematic diagram of the system is illustrated in Figure 3.6. Points P and I are the center of the exit pupil of the DLP projector and that of the CCD camera, respectively. The optical axes of the projector and the camera coincide at point O . After the system has been set up, a flat reference plane is measured first whose phase map is used as the reference for subsequent measurements. The height of the object surface is measured relative to this plane. From the point view of the DMD camera, point D on the object surface has the same phase value as point C on the reference plane, $\phi_D = \phi_C$. While on the CCD array, point D on the object surface and A on the reference plane are imaged on the same pixel. By subtracting the reference phase map from the object phase map, we obtained the phase difference at this specific pixel:

$$\phi_{AD} = \phi_{AC} = \phi_A - \phi_C, \quad (3.9)$$

Assume points P and I are designed to be on the same plane with a distance l to the reference plane and have a fixed distance d between them, and reference plane is parallel to the device. Thus, $\triangle PID$ and $\triangle CAD$ are similar, the height of point D on the object surface relative to reference plane \overline{DB} can be related to the distance between points A and C , or \overline{AC} :

$$\frac{d}{\overline{AC}} = \frac{l - \overline{DB}}{\overline{DB}} = \frac{l}{\overline{DB}} - 1, \quad (3.10)$$

Since d is much larger than \overline{AC} for real measurement, this equation can be simplified as

$$z(x, y) = \overline{DB} \approx \frac{l}{d} \overline{AC} = \frac{pl}{2\pi d} \phi_{AC} = K \phi_{AC}, \quad (3.11)$$

where p is the fringe pitch on the reference plane. Therefore, a proportional relationship between the phase map and the surface height can be derived.

A calibration standard with a known height is used to determine the phase-height conversion constant K . The calibration height of the step from the flat board is 1.506 ± 0.01 inches. Figure 3.7 shows a measurement result of a flat board with a step height on top. From the cross section of the top surface and bottom surfaces, we

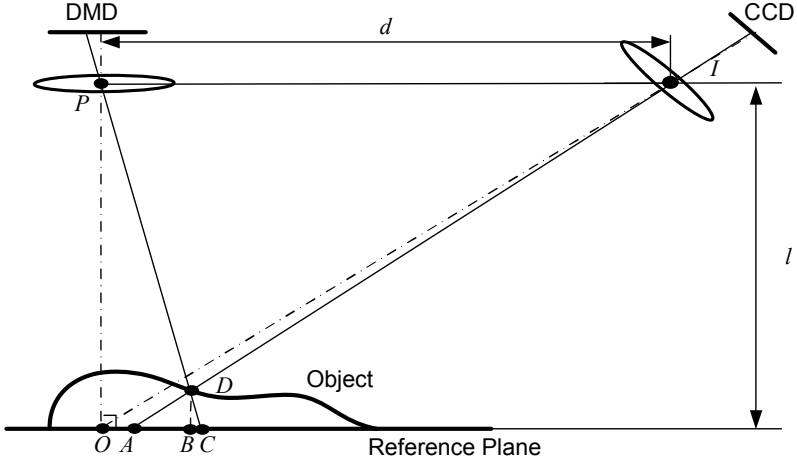


Figure 3.6: Schematic diagram of phase-to-height conversion.

can calculate the phase difference between the top and bottom surfaces of the step is $\phi_{AC} = \phi_A - \phi_C = \phi_{top} - \phi_{bottom} = 3.6054 - (-0.9909) = 4.5963$ rad. Therefore the constant K is:

$$K = \frac{1.506}{4.5963} = 0.3227(\text{inch/rad}) = 8.3224(\text{mm/rad}) . \quad (3.12)$$

We assume the x and y coordinate values are proportional to the real coordinate of the object for this simple algorithm. The measured area on the reference plane is 260×244 mm, therefore, the x and y coordinate conversion constants are,

$$k_x = k_y = \frac{260}{532} = 0.4887(\text{mm/pixel}) . \quad (3.13)$$

By applying K , k_x and k_y on the 3D phase map of the reconstructed image, we can obtain the 3D coordinates of the measured object.

This calibration method only gives approximate relationship between the phase map and the real coordinates. For objects with small depth, all assumptions can be sufficiently satisfied. However, for objects with large depths, this simple calibration may not provide accurate results for the following reasons:

- (1) The reference plane is required to put parallel to the device. It is difficult for practice to measure the reference plane.
- (2) The fringe is assumed to be uniformly distributed on the reference plane. It is usually not the case.

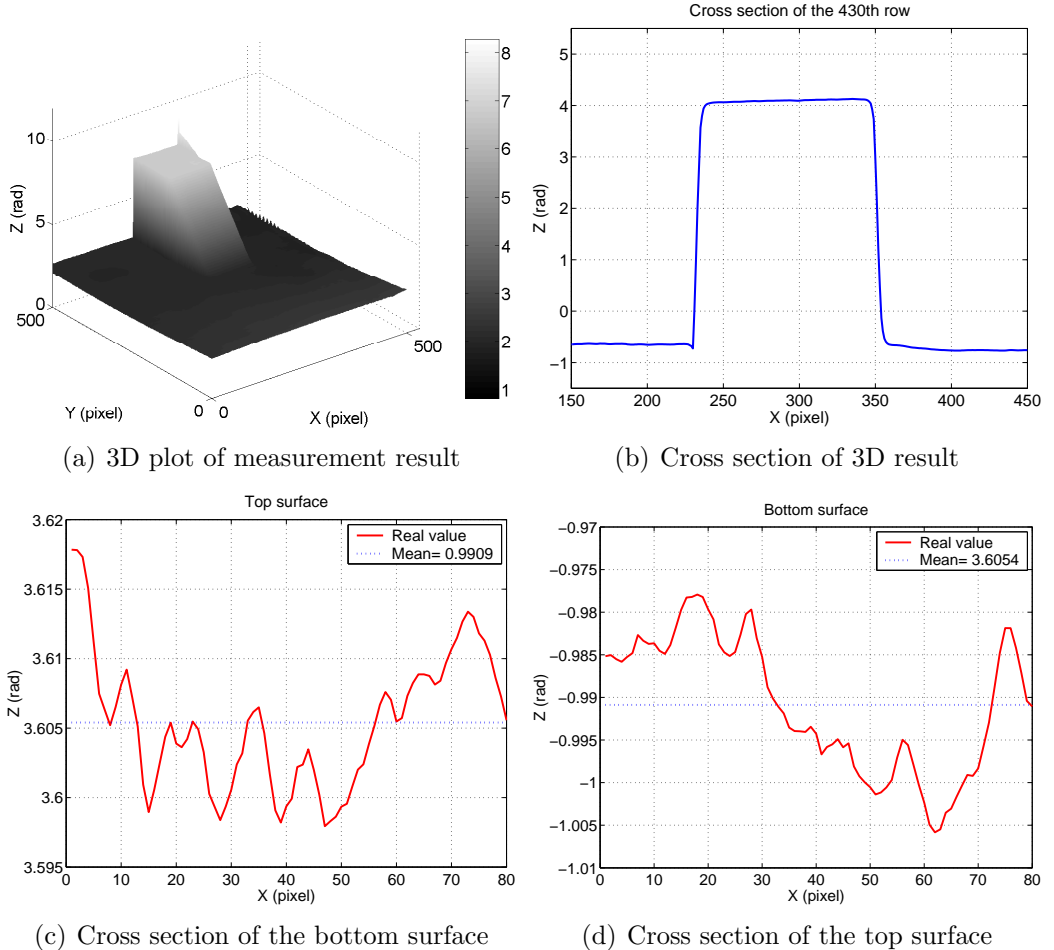


Figure 3.7: Measurement result of a flat board with a step.

- (3) The reference plane is assumed to include the distortion of the measured object shape. However, for different object depths from the reference plane, the degree of distortion is different. Therefore, subtracting the same reference plane from the measured object shape will not remove the distortions.
- (4) This approximation is only for small depth measurement. The approximation in Equation 3.11 does not hold for large dynamic range measurement.
- (5) The ignored distortion of lens, sensor noise, etc., induces errors for real measurement.

In Chapter 7, we will propose a novel structured light system calibration technique that is more accurate.

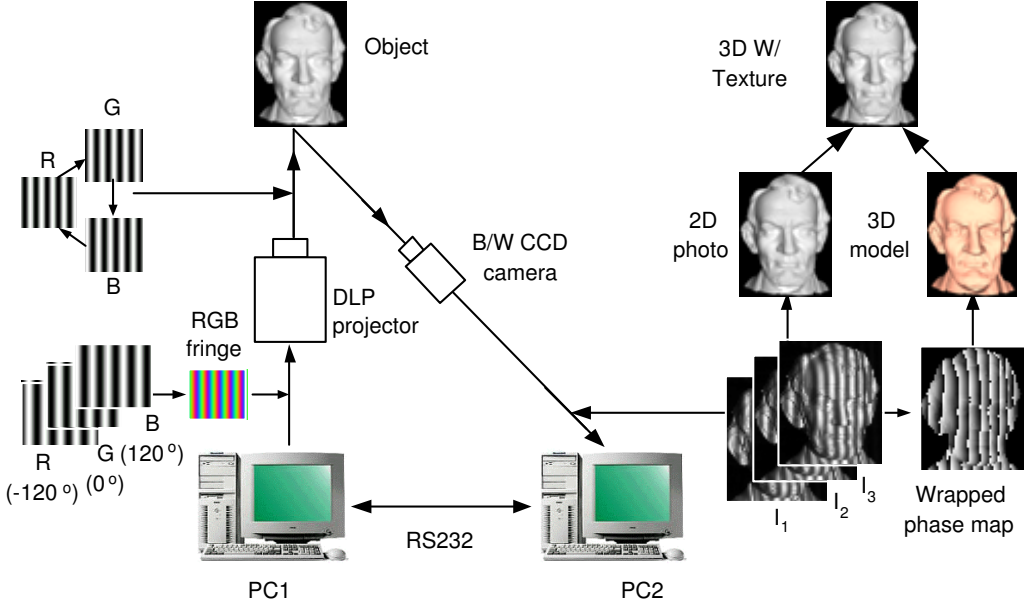


Figure 3.8: Schematic diagram of the real-time 3D shape measurement system.

3.3 Real-time 3D Shape Measurement System

3.3.1 System setup

Figure 3.8 shows the schematic diagram of the real-time 3D shape measurement system developed in this research. A color fringe pattern is generated by a Personal Computer (PC) and is projected onto the object by a DLP video projector (Kodak DP900). A high-speed B/W CCD camera (Dalsa CA-D6-0512W) synchronized with the projector is used to capture the distorted fringe images of each color channel. Phase-wrapping and -unwrapping algorithms are implemented to reconstruct the 3D geometry. Since the fringe images used have $2\pi/3$ of phase shift, averaging three fringe images result in a 2D image without fringes, which can be used for texture mapping. Figure 3.9 is a picture of the system developed in this research.

The whole measurement system basically includes five components: one Dell desktop computer (Pentium 4, 2.8 GHz CPU, 1 GB DDR SDRAM at 333 MHz, 80 GB hard drive) with a Matrox frame grabber Meteor II/Digital installed, one Kodak DP900 digital projector, one Dalsa high-speed CCD camera (CA-D6-0512), and one external timing signal generator circuit board.

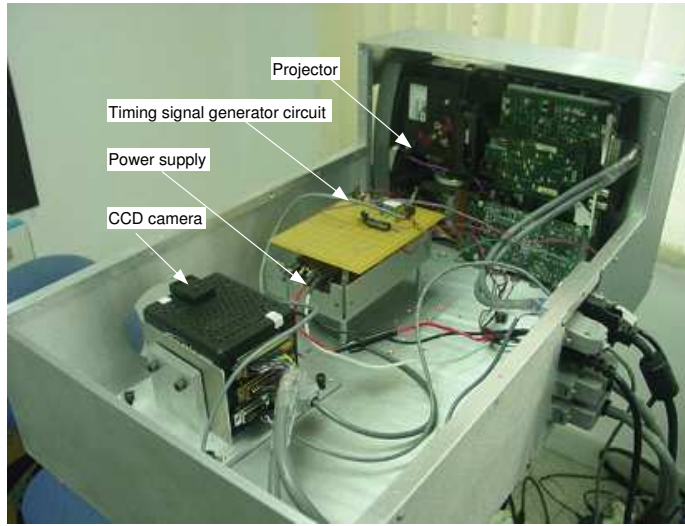


Figure 3.9: Photograph of the real-time 3D shape measurement system.

The digital projector has one DMD chip with a resolution of 800×600 pixels and a brightness of 900 lumens. It receives the video signal from a PC's video output and projects the image onto the object surface.

The CCD camera is a high-speed camera with full frame rate at 262 frames per second. It has $532(H) \times 516(V)$ pixels CCD image sensor with 10 mm square pixels with 100% fill factor, and 8-bit data depth (256 gray levels).

In this research, we use Matrox frame grabber, which supports digital video acquisition from standard and non-standard cameras in a single or multi-tap configuration, offering RGB and monochrome grabs. There are some different software tools that support the frame grabber. In this research, the Matrox Imaging Library (MIL) provided by Matrox imaging is used, which is basically a set of functions that controls image acquisition, transferring, displaying and processing.

Figure 3.10 is the schematic diagram of the timing signal generator circuit that provides the signals to trigger projector as well as the camera. The trigger signal to the projector is voltage signal +10 mv at low level and +56 mv at the high level, The trigger signal for the camera is an opto-isolated differential signal connected to the frame grabber via RS232. The exposure time can be adjusted by the user.

In order to capture 120 2D 8-bit fringe images per second, a software algo-

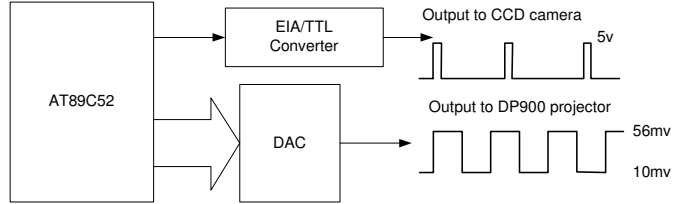


Figure 3.10: Schematic diagram of the timing signal generator circuit.

rithm called “double buffering” is utilized. The principle of double buffering is that the events of grabbing and transferring images occur simultaneously under the asynchronous mode of the camera. A parallel software is developed to acquire a large number of images continuously.

Image acquisition is the first step. The second step is to utilize the 3D vision software developed in this research to reconstruct 3D models. OpenGL tools are employed to render the 3D model, GLUT is utilized to create the GUI. Figure 3.11 shows the modules of our 3D Vision software, which consists of eight modules including fringe generation, image capture, camera control, phase wrapping, phase unwrapping, coordinate calculation, 3D display, and file I/O. Fringe generation is responsible for producing various types of fringe patterns with shifted phases. Image acquisition controls real-time image data acquisition. Phase wrapping and unwrapping modules include algorithms for image processing and 3D model reconstruction. Coordinate calculation module is used to calculate the real x , y and z coordinates from the phase map. 3D display is used to render the measured results, while the File I/O module handles various data preprocessing, data storing, data converting, and data saving.

3.3.2 Experiments

After calibration, we first tested the measurement uncertainty of the system. Figure 3.12 shows the measured results of a flat board. Since the surface is very smooth, the variations shown in the results are largely due to the noise of the system, which is RMS 0.05 mm for the measured area. We then measured a static sculpture, the results are shown in Figure 3.13. The geometric result is shown in Figure 3.13(d),

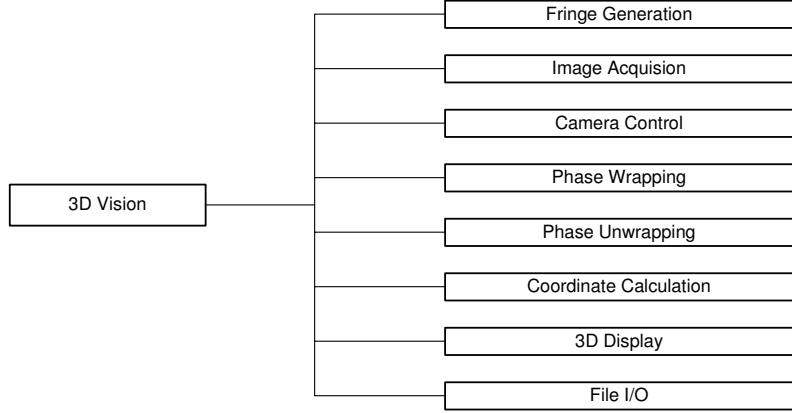


Figure 3.11: 3D Vision software modules.

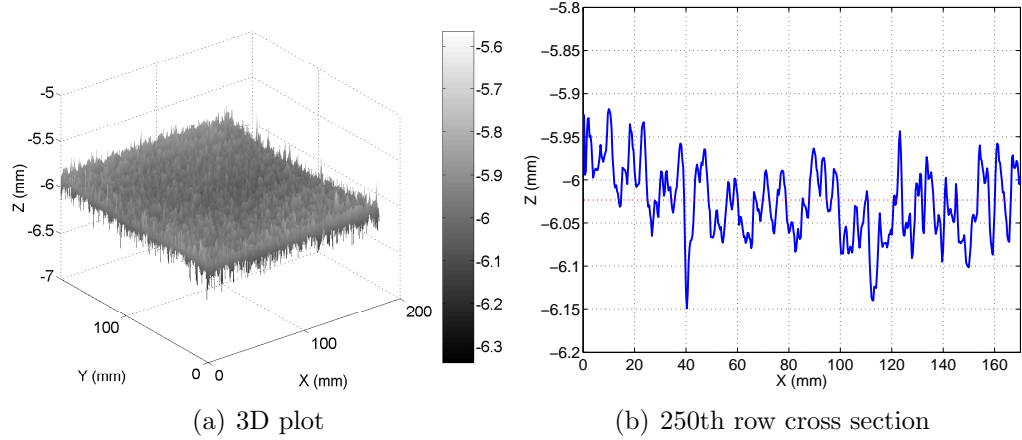


Figure 3.12: Measured result of a flat board with a smooth surface.

which is smooth with details. We also measured a human face as shown in Figure 3.14. Again, the measured 3D geometry is smooth with low noise. It should be noted that during the experiment, we intentionally asked the subject to smile so that facial expressions was captured. These experimental results demonstrated that the system could measure slow moving objects. To verify the performance of the system in measuring human facial expression changes, a series of 3D images with exaggerated facial expressions are recorded. Figure 3.15 shows three frames picked from 539 3D frames captured at 40 frames per second with a resolution of 532×500 pixels. From these frames and their zoom-in views, we can see clearly the details of facial expressions and changes.

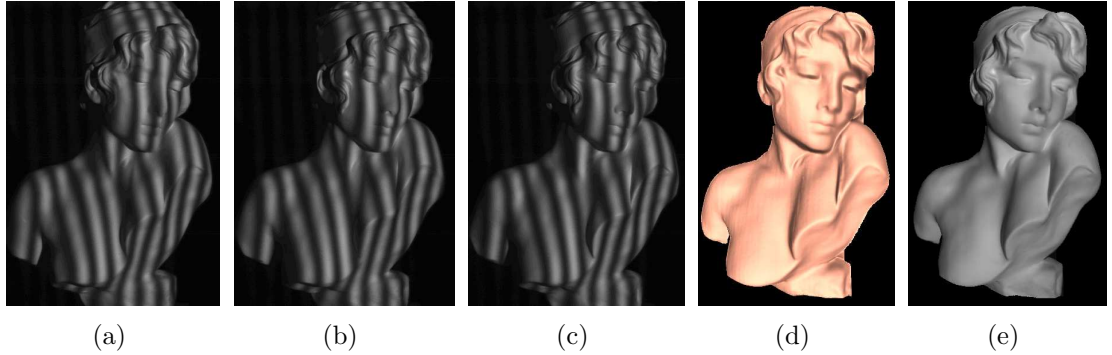


Figure 3.13: 3D shape measurement results of the sculpture Sapho. (a) $I_1(-2\pi/3)$. (b) $I_2(0)$. (c) $I_3(2\pi/3)$. (d) 3D geometry. (e) 3D geometry with texture mapping.

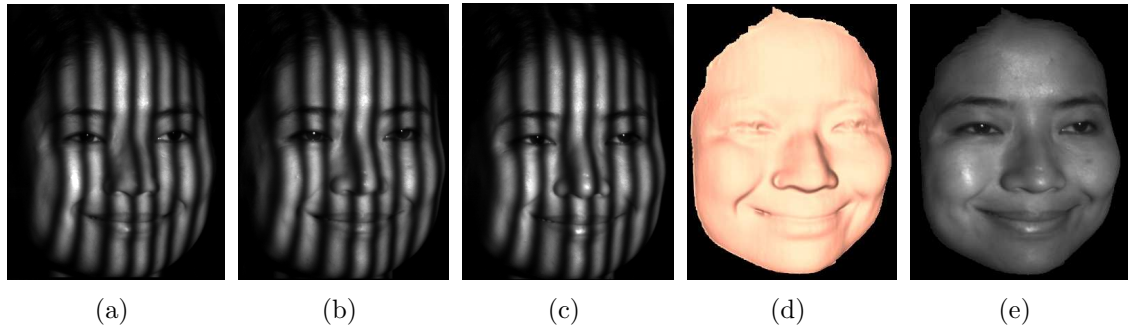


Figure 3.14: 3D shape measurement result of a human face. (a) $I_1(-2\pi/3)$. (b) $I_2(0)$. (c) $I_3(2\pi/3)$. (d) 3D geometry. (e) 3D geometry with texture mapping.

3.4 System with Color Texture Mapping

Color texture mapping is desired for many applications. However, for 3D data acquisition, color should be avoided because it affects the measurement accuracy. In order to solve this dilemma, we develop a system with two cameras: A B/W camera and a color camera. The B/W camera is used to capture fringe images for 3D geometric reconstruction, and the color camera is used to provide color photos for color texture mapping.

3.4.1 System setup

Figure 3.16 illustrates the schematic diagram of the real-time 3D shape measurement system with color texture mapping. A color camera (Uniq Vision UC-930)



Figure 3.15: Measurement results of human facial expressions.

synchronized with the projector is added in the previously developed B/W system shown in Figure 3.8. A beam splitter is used to divide the incoming light into two parts, one for the B/W camera, and the other for the color camera. Since the transmitted portion and reflected part are from the same input light source, viewing from both directions gives the same information excluding the difference of intensity.

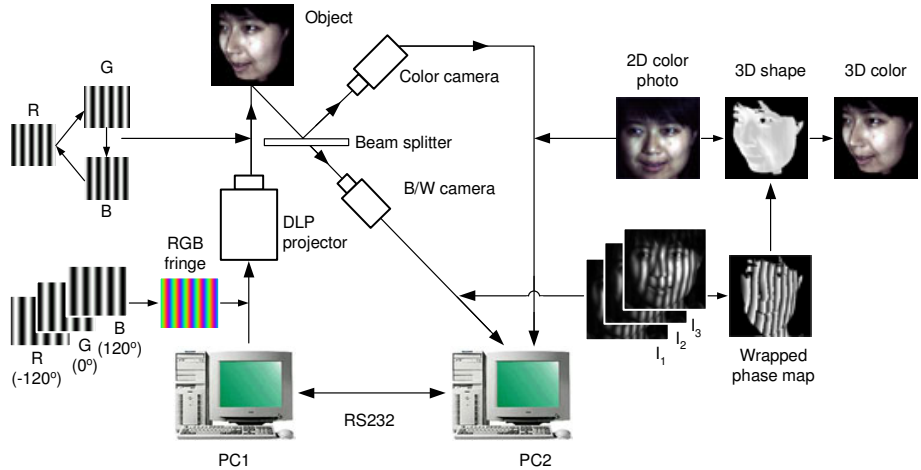


Figure 3.16: Schematic diagram of the real-time 3D shape measurement system with color texture mapping.

Therefore, the color photo acquired by the color camera can be used for texture mapping purpose.

The color camera is a 10-bit pseudo-color camera using a Bayer color filter. The color information is recorded in a single sensor simultaneously. The indices of the pixels are encoded to certain standard that indicates which color the pixel represents. The color information can be recovered by software from the single image.

3.4.2 Camera synchronization

The exposure time of the color camera is chosen to be one projection cycle, 12.5 ms, to eliminate the fringe pattern and produce the texture image. Figure 3.17(a) shows the timing chart of the color system. The waveform at the top is the trigger signal to the projector generated by a microcontroller based timing signal circuit. The second waveform from the top is the projection timing chart. The next two waveforms are the trigger signals to the B/W camera and the color camera, respectively. The frame rate for the color camera is limited to 26.7 frames per second, which is good enough for texture mapping purpose. In order to keep color and B/W cameras synchronized, we reduce the frame rate of our 3D acquisition so that it is the same as that of the color camera. However, the time for acquiring three phase-shifted fringe patterns is kept the same. Therefore, potential object motion induced error will stay

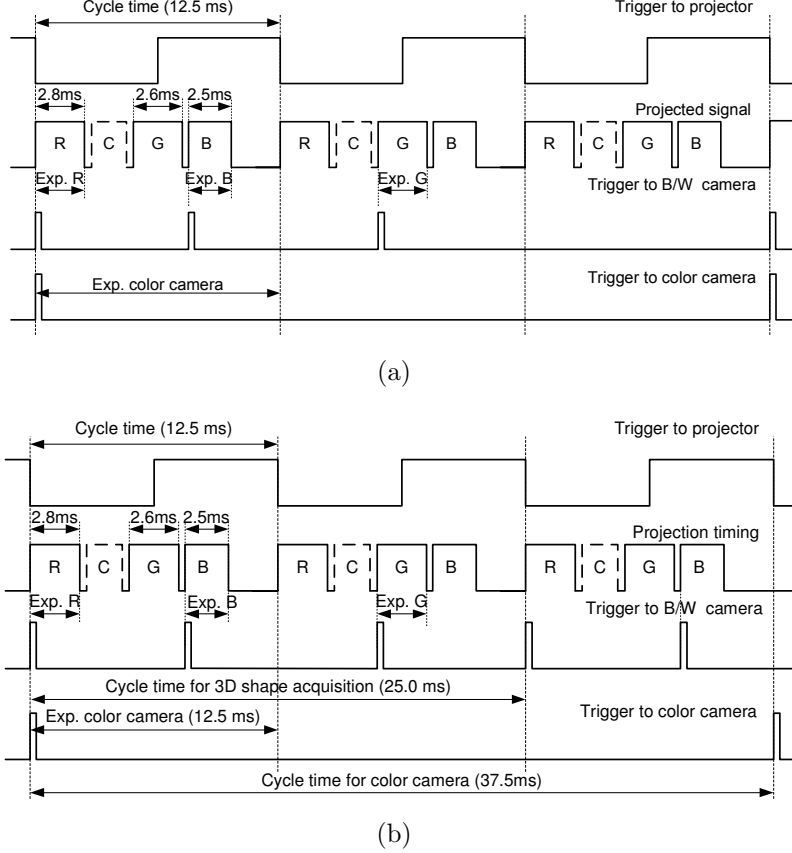


Figure 3.17: Color system timing chart.

the same. We first use one PC to capture both color and B/W images. To avoid the conflict of two cameras, a parallel processing software is developed. Figure 3.18 shows a photograph of the developed hardware system with an added color camera. However, our experiments demonstrate that using one PC to capture images for both cameras cause large error due to mutual interference. Therefore, instead of one PC, two PCs are utilized to avoid the interference problem of two cameras. The frame rate of the B/W camera can remain to be 40 frames per second. The color camera captures color texture images at a frame rate of 26.7 frames per second. The color texture images for 3D models in between can be obtained by linearly interpolating two neighboring images. The timing chart is shown in Figure 3.17(b).

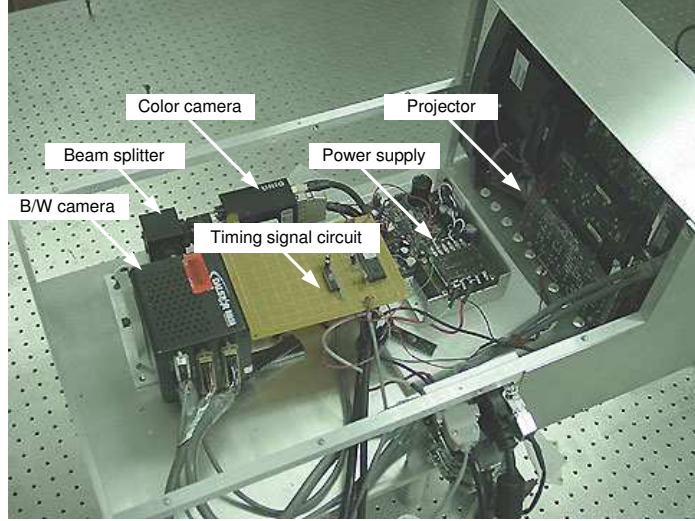


Figure 3.18: Photograph of the real-time 3D shape measurement system with color texture mapping.

3.4.3 Camera alignment

Theoretically, two cameras capture the same images, however, practically, it is difficult. Therefore aligning two cameras and matching correspondence are necessary. In order to find the relationship between two cameras, a coordinate transformation matrix P has to be determined, which satisfies

$$\begin{bmatrix} sx_{bw} \\ sy_{bw} \\ s \end{bmatrix} = \begin{bmatrix} p_{11} & p_{12} & p_{13} \\ p_{21} & p_{22} & p_{23} \\ p_{31} & p_{32} & p_{33} \end{bmatrix} \begin{bmatrix} x_c \\ y_c \\ 1 \end{bmatrix} = P X_c, \quad (3.14)$$

where x_{bw}, y_{bw} are coordinates of the B/W camera, x_c, y_c coordinates of the color camera, and s the scaling factor. The transformation matrix can be obtained by finding a set of corresponding points in the B/W image and color image using singular value decomposition (SVD) algorithm. It should be noticed that the transformation matrix P only needs to be determined once since the relationship between two cameras is fixed by the hardware system setup.



(a) Measured 3D models



(b) Measured results with color texture mapping of the above 3D models

Figure 3.19: Real-time 3D measurement result of human facial expression with color texture mapping.

3.4.4 Experiments

After the system is calibrated and two cameras are aligned, we measured dynamic objects. Again human facial expression was measured. Figure 3.19 are several frames chosen from a sequence of 540 frames captured at 40 Hz for the 3D model, and 26.7 Hz for the color texture. We see that the facial expression details were clearly captured, and that the color texture images are well aligned with 3D geometric models.

3.5 Real-time 3D Shape Measurement System: Generation II

The Kodak DP900 projector as an early model of DLP projectors, caused many problems in our system. First, the lamp life span was very short, only 100 hours for

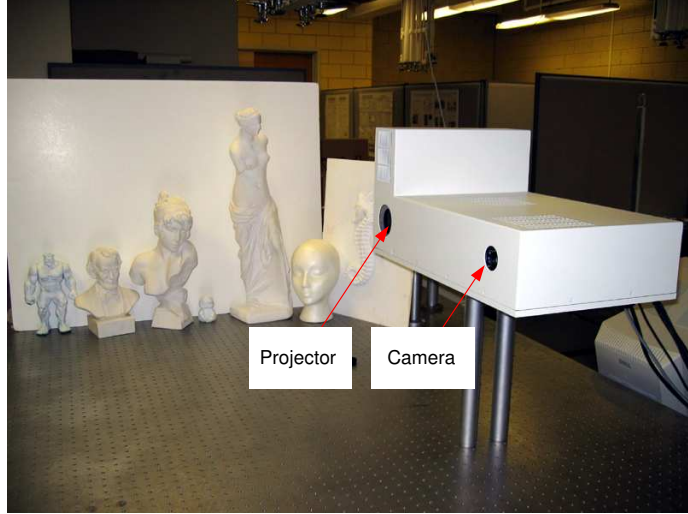


Figure 3.20: Photograph of real-time 3D shape acquisition system: Gen II.

reasonable measurements. Second, the calibration was tedious. It took about one hour each time to warm up and calibrate the system. Third, the projector was not stable, with the noise level changing from frame to frame. This is not desirable for real-time 3D shape measurement. Moreover, the projector has to be shut down for cooling after working for about 2.5 hours, and thus it is difficult to collect a large volume of data. Therefore, replacing the projector with a newer model was necessary. A customized new projector, PLUS U2-1200 was chosen as a substitute. After replacing the projector, the system became much more stable and easier to calibrate. Moreover, the projector also has a desirable B/W projection mode that is convenient for our application. Figure 3.20 shows the developed new system, which is a little smaller than the old one. But the color camera cannot be added due to the use of a new DMD projection mechanism in the new projector. The size of the system is approximately $21'' \times 12.5'' \times 10''$. The drawback of the new system is that its acquisition speed is reduced to 30 frames per second due to the hardware limitation.

Figure 3.21 shows some sculptures measured by the new system. We also measured dynamic facial expressions as shown in Figure 3.22. 12 frames for this subject are selected from 539 frames recorded at 30 frames per second. All these frames have similar noise level, which is good for repeated measurements.

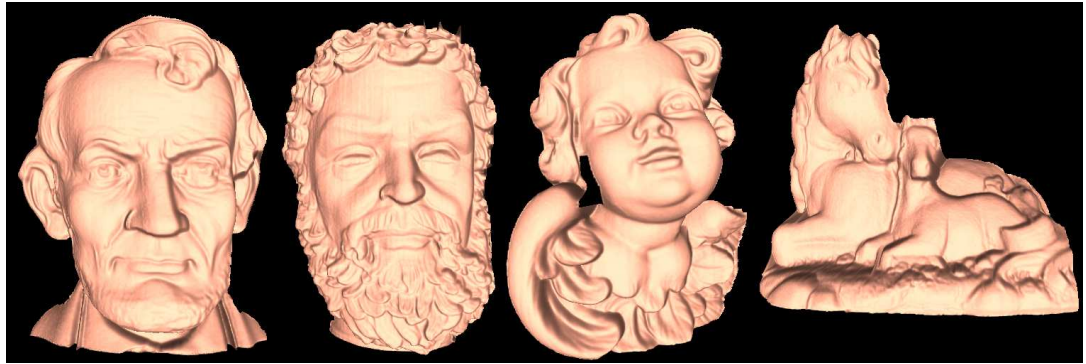


Figure 3.21: Measurement results using the new system. From left to right are Lincoln, Zeus, Angel, and Horses.

3.6 Real-time 3D Data Acquisition, Reconstruction, and Display System

The system we developed could acquire 3D data in real time. Our goal was to achieve simultaneous 3D data acquisition, reconstruction, and display, all in real time. To reach our goal, a parallel processing software employing a fast 3D reconstruction algorithm is developed. We will discuss the fast 3D reconstruction algorithms in Chapters 4 and 5. This section discusses the framework of this real-time system.

3.6.1 Principle

Figure 3.23 illustrates the pipeline of real-time 3D acquisition, reconstruction, and rendering system. The system includes three threads,

- *Acquisition.* A high-speed CCD camera captures fringe images in real time, and the fringe images are continuously sent to the computer.
- *Reconstruction.* 3D reconstruction algorithm based on newly proposed fast phase-wrapping algorithm (to be discussed in Chapter 5) is employed to generate 3D models in real time.
- *Display.* The 3D models are sent to the graphics card for display.

As discussed above, the new system is able to acquire 90 frames of 2D fringe images per second. These 2D images are then sent to the computer directly without



Figure 3.22: Measurement results of facial expressions using the new system.

any processing. Since the algorithm used in this research is the three-step phase-shifting algorithm, any three consecutive images can be used to reconstruct one 3D model through phase-wrapping and -unwrapping. With the help of the fast 3D reconstruction algorithms, 3D reconstruction can keep up with acquisition. For the current system, the typical reconstruction time for one frame is about 12.5 ms with

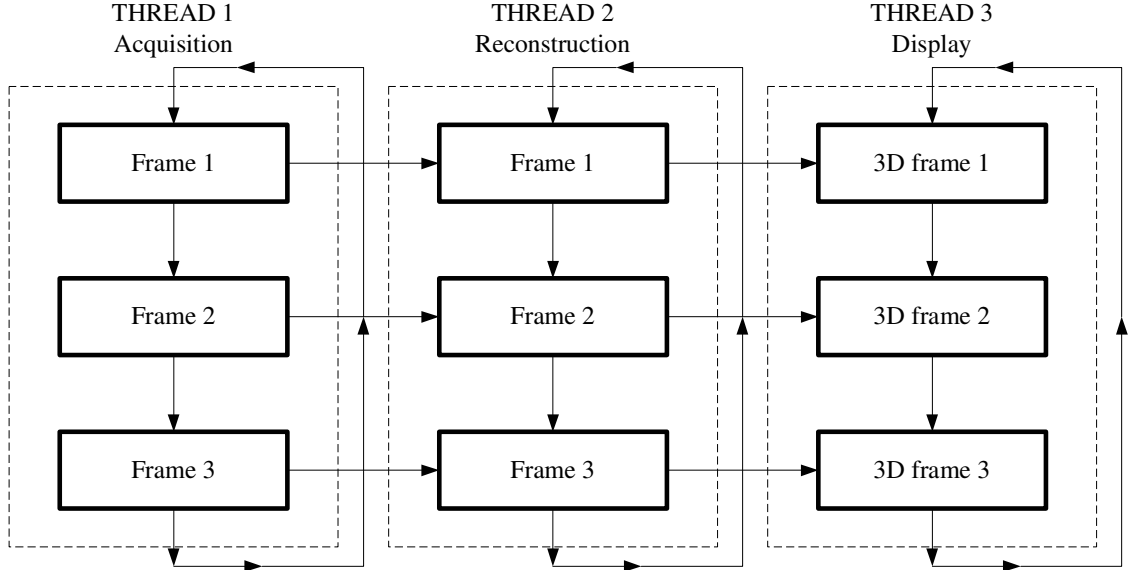


Figure 3.23: Real-time 3D acquisition, reconstruction, and rendering pipeline.

a Pentium 4, 2.8 GHz CPU workstation. The reconstructed 3D point clouds are converted to 3D geometric coordinates and sent to the graphics card for display.

Our experiments showed that a dual-CPU computer was necessary for this real-time system. One CPU handles the acquisition, while the other CPU deals with the reconstruction and display. The reconstruction typically takes 12.5 ms one CPU time per frame. Therefore, only 20.8 ms left for display, which is not enough for full-resolution, 532×500 pixels, rendering. Experiments demonstrated that only 1/9 points could be rendered in real time for the current algorithm. If a Graphics Processing Unit (GPU) is utilized, a full-resolution rendering in real time can be expected.

Three threads, the acquisition thread, reconstruction thread, and display thread are used to realize real-time 3D shape acquisition, reconstruction, and display. The acquisition thread is responsible for continuously capturing fringe images from the camera. The reconstruction thread takes in the fringe images passed over by the acquisition thread, reconstructs the 3D shape, and then passes the data to the display thread where the 3D shape is rendered. At any moment of the time, if the acquisition thread is capturing frame i , the reconstruction thread is processing the immediately

previous frame $i - 1$, and the display thread is rendering still the previous frame ($i - 2$). Between the acquisition thread and the reconstruction thread, or the reconstruction thread and the display thread, there is always a delay of one frame. During the process, no frame of data is stored or remained in the memory for more than the time of acquiring three frames. That is, the fourth frame overrides the first frame and so on.

3.6.2 Experiments

In this research, we used a DELL Precision 650 workstation, with dual CPUs (2.8 GHz), 1 GB memory to accomplish the procedures. The programming environment was Microsoft Visual C++6.0. Figure 3.24 shows the experimental environment of the real-time 3D system. The projector is very bright, so is the face with illumination. To balance the contrast of the image, an additional projector was utilized to project the computer screen onto a white board on the side of the subject. Figure 3.25 shows one image of a video sequence recorded during the experiments. The left image is a human subject, while the right image is the image generated by the computer in real time.

3.7 Discussion

The real-time 3D shape measurement systems developed in this research have the following advantages over other systems:

- *High resolution.* The phase-shifting method employed in this research provide a pixel-level resolution, which is much higher than that of stereo vision or binary coding based methods.
- *High acquisition speed.* Our real-time 3D system has achieved a speed of up to 40 frames per second with grayscale texture mapping. With color texture mapping, the speed is reduced to 26.7 frames per second due to the limited frame rate of the color camera. The acquisition speed is already faster than that achieved by most of the other methods proposed. In the future, the

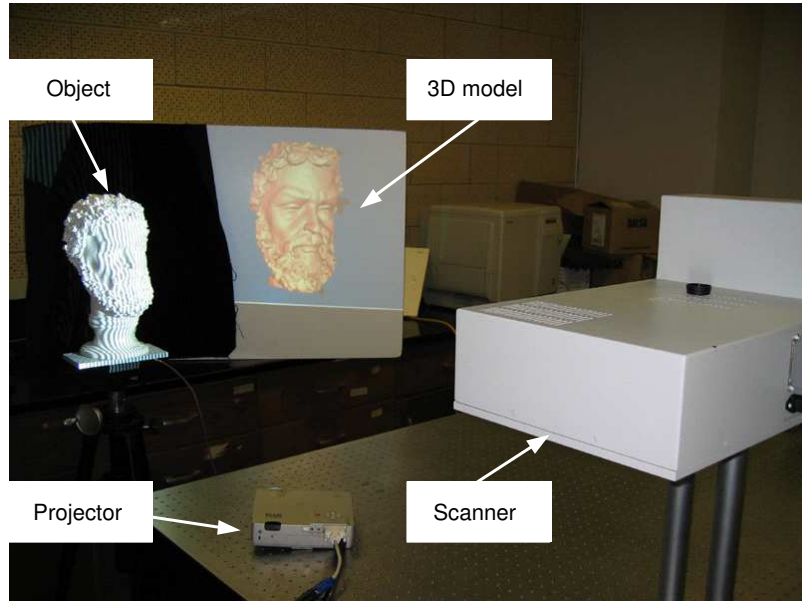


Figure 3.24: Experimental environment for real-time 3D shape acquisition, reconstruction, and display.

acquisition speed can be further improved if a faster camera is used, the maximum achievable 3D shape acquisition speed is 120 frames per second, which is determined by the projector.

- *High processing speed.* With the fast phase-wrapping algorithm, the processing time for 3D shape reconstruction is reduced to approximately 12.5 ms per frame with a Pentium 4, 2.8 GHz PC.
- *Large dynamic range.* Since the sinusoidal phase shifting method is insensitive to the defocusing of the projected pattern, a relatively large depth can be measured, provided that the fringe visibility is good enough.
- *Simultaneous 2D and 3D acquisition.* This is one of the unique features of the sinusoidal phase shifting method. From the three phase-shifted fringe images, 3D and 3D information can be obtained simultaneously.
- *Color tolerance.* Unlike those real-time systems based on color coded structured light methods, this system uses B/W fringe images, therefore the object color does not affect the measurement accuracy.

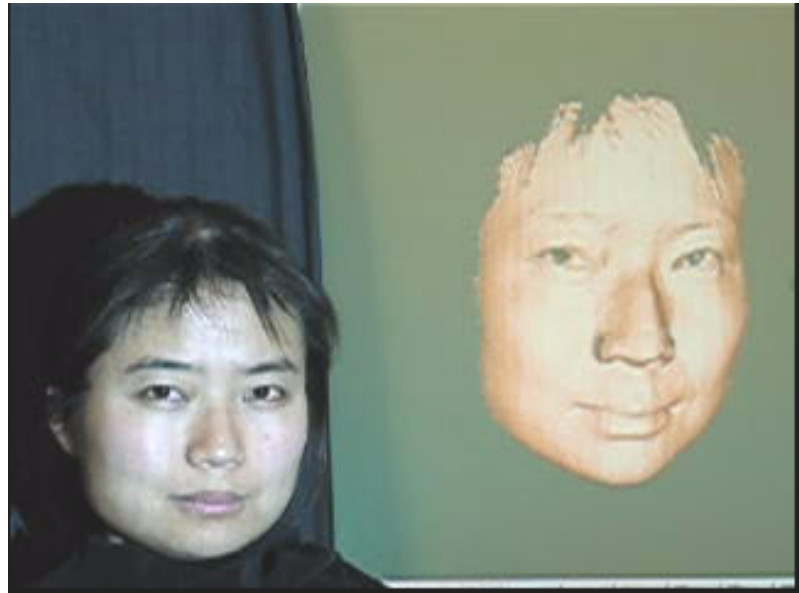


Figure 3.25: Experiment on real-time 3D shape acquisition, reconstruction and display.

- *Real-time acquisition, reconstruction, and display.* Phase-shifting algorithm is a pixel-by-pixel geometry computation that does not require computation intensive stereo matching, real-time reconstruction and display is one of the biggest advantages of the system.

In the meanwhile, the system shares some of the same shortcomings of structured light methods. The measuring surfaces has to be diffuse to obtain high accuracy. Since this method is based on light reflection, the system can not handle dark surfaces well.

3.8 Summary

Two high-resolution, real-time 3D shape measurement systems have been successfully developed in this research. Both systems generate a data cloud of 532×500 points per frame. The first system has a speed of 40 frames per second for 3D data acquisition, 40 frames per second for B/W texture image acquisition, and 26.7 frames per second for color texture image acquisition. The second system has a lower speed of 30 frames per second for both 3D data and B/W texture image acquisition. Color

texture mapping is not possible for the second system due to hardware limitation. However, the second system is much more stable and produces better results with smaller errors, as compared to the first system. By further implementing the fast 3D reconstruction algorithms and parallel processing technique into the real-time 3D data acquisition system, we developed a system that can simultaneously acquire, reconstruct and display 3D information of the measured object at a frame rate of up to 40 frames per second and at a image resolution of 532×500 points per frame. Experiments demonstrated that the real-time system provided satisfactory measurement results for slow moving objects such as human facial expressions. In the following two chapters, Chapter 4 and Chapter 5, we will discuss the algorithms that enabled real-time 3D reconstruction in details.

Chapter 4

Trapezoidal Phase-shifting Algorithm

This chapter addresses a novel structured light method, namely trapezoidal phase-shifting method, for 3D shape measurement. This method uses three patterns coded with phase-shifted, trapezoidal-shaped gray levels. The 3D information of the object is extracted by direct calculation of an intensity ratio. The 3D reconstruction speed is at least 4.5 times faster than traditional sinusoidal phase-shifting algorithm. Our experiments demonstrate that the 3D reconstruction speed can be as high as 40 frames per second for an image resolution of 532×500 .

4.1 Introduction

Codification based on linearly changing gray levels, or the so-called intensity-ratio method, has the advantage of fast processing speed because it requires only a simple intensity-ratio calculation. In this chapter, we describe a novel coding method, the trapezoidal phase-shifting method, which combines the advantages of the high processing speed of the intensity ratio based methods and the high vertical resolution of the sinusoidal phase-shifting methods. Its lateral resolution is at the pixel level, which is the same as that of the intensity-ratio based methods and the sinusoidal phase-shifting methods. Compared to the intensity-ratio based methods, this method is also far less sensitive to image defocus, which significantly reduces measurement errors when the measured object has a large depth. However, when compared to the sinusoidal phase-shifting methods, which are not sensitive to image defocus at all, the sensitivity of this method to image defocus, albeit very low, may

be less than ideal for some applications. This is the only conceivable disadvantage of the proposed method.

Section 4.2 explains the principle of the trapezoidal phase-shifting method. Section 4.3 analyzes the potential error sources of the method, in particular, the image defocus error. The experimental results are presented in Section 4.4 and the conclusions are given in Section 4.5.

4.2 Trapezoidal Phase-shifting Method

Intensity-ratio based methods for 3D shape measurement have the advantage of fast processing speed because the calculation of the intensity ratio is rather simple. However, these methods usually show large measurement noise, which limits their applications. To reduce measurement noise, one has to repeat the ramp pattern to create the so-called triangular or pyramidal patterns. The smaller the pitch of the pattern is, the lower the noise level will be. However, the periodical nature of the pattern introduces the ambiguity problem, which causes errors when objects with discontinuous features are measured. Another major problem with the use of a triangular or pyramidal pattern is that the measurement is highly sensitive to the defocusing of the image. This can cause problems when objects with a relatively large depth are measured and the projector or the camera does not have a large enough depth of focus.

In this research, we propose to use a new coding method called the trapezoidal phase-shifting method to solve the problems of the conventional intensity-ratio method while preserving its advantages. This method can increase the range of the intensity-ratio value from [0, 1] for the traditional intensity-ratio method to [0, 6] without introducing the ambiguity problem, thus reducing the noise level by 6 times. For even lower noise level, the pattern can also be repeated. This introduces the ambiguity problem but to a lesser degree. Another advantage of the trapezoidal method is that the measurement is much less sensitive to image defocus.

The proposed trapezoidal phase-shifting method is very similar to the three-step sinusoidal phase-shifting method, only that the cross-sectional shape of the

patterns has been changed from sinusoidal to trapezoidal. To reconstruct the 3D shape of the object, three patterns, which are phase-shifted by $2\pi/3$ or one-third of the pitch, are needed. Figure 4.1 shows the cross sections of the three patterns. Their intensities can be written as follows:

$$I_1(x, y) = \begin{cases} I'(x, y) + I''(x, y) & x \in [0, T/6) \text{ or } [5T/6, T] \\ I'(x, y) + I''(x, y)(2 - 6x/T) & x \in [T/6, T/3) \\ I'(x, y) & x \in [T/3, 2T/3) \\ I'(x, y) + I''(x, y)(6x/T - 4) & x \in [2T/3, 5T/6) \end{cases}, \quad (4.1)$$

$$I_2(x, y) = \begin{cases} I'(x, y) + I''(x, y)(6x/T) & x \in [0, T/6) \\ I'(x, y) + I''(x, y) & x \in [T/6, T/2) \\ I'(x, y) + I''(x, y)(4 - 6x/T) & x \in [T/2, 2T/3) \\ I'(x, y) & x \in [2T/3, T] \end{cases}, \quad (4.2)$$

$$I_3(x, y) = \begin{cases} I'(x, y) & x \in [0, T/3) \\ I'(x, y) + I''(x, y)(6x/T - 2) & x \in [T/3, T/2) \\ I'(x, y) + I''(x, y) & x \in [T/2, 5T/6) \\ I'(x, y) + I''(x, y)(6 - 6x/T) & x \in [5T/6, T] \end{cases}, \quad (4.3)$$

where $I_1(x, y)$, $I_2(x, y)$ and $I_3(x, y)$ are the intensities for the three patterns respectively, $I'(x, y)$ and $I''(x, y)$ are the minimum intensity and intensity modulation at position (x, y) respectively, and T is the pitch of the patterns. Each pattern is divided evenly into six regions that can be identified by knowing the sequence of the intensity values of the three patterns. The intensity ratio can be computed by

$$r(x, y) = \frac{I_{med}(x, y) - I_{min}(x, y)}{I_{max}(x, y) - I_{min}(x, y)}, \quad (4.4)$$

where $I_{min}(x, y)$, $I_{med}(x, y)$, and $I_{max}(x, y)$ are the minimum, median, and maximum intensities of the three patterns for point (x, y) . The value of $r(x, y)$ ranges from 0 to 1. Figure 4.2 shows the cross section of the intensity ratio map. The triangular

shape can be removed to obtain a ramp by using the following equation:

$$r(x, y) = 2 \times \text{round} \left(\frac{N - 1}{2} \right) + (-1)^{N+1} \frac{I_{med}(x, y) - I_{min}(x, y)}{I_{max}(x, y) - I_{min}(x, y)}, \quad (4.5)$$

where $I_{min}(x, y)$, $I_{med}(x, y)$, and $I_{max}(x, y)$ are the minimum, median, and maximum intensities of the three patterns for point (x, y) . The value of $r(x, y)$ ranges from 0 to 1. Figure 4.2 shows the cross section of the intensity ratio map. The triangular shape can be removed to obtain a ramp by using the following equation:

$$r(x, y) = 2 \times \text{round} \left(\frac{N - 1}{2} \right) + (-1)^{N+1} \frac{I_{med}(x, y) - I_{min}(x, y)}{I_{max}(x, y) - I_{min}(x, y)}, \quad (4.6)$$

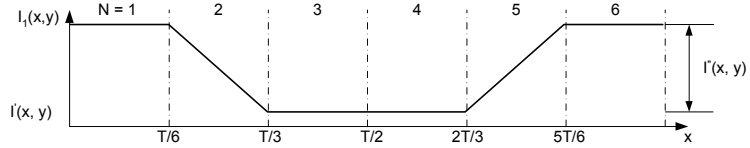
where $N = 1, 2, \dots, 6$ is the region number, which is determined by comparing the three intensity values at each point. After the removal of the triangular shape, the value of $r(x, y)$ now ranges from 0 to 6, as shown in Figure 4.3. If multiple fringes are used, the intensity ratio is wrapped into this range of 0 to 6 and has a sawtooth-like shape. A process similar to phase unwrapping in the traditional sinusoidal phase-shifting method needs to be used. The Depth information can be obtained from this intensity ratio based on an algorithm similar to the phase-to-height conversion algorithm used in the sinusoidal phase-shifting method.(see Section 3.2.5).

4.3 Error Analysis

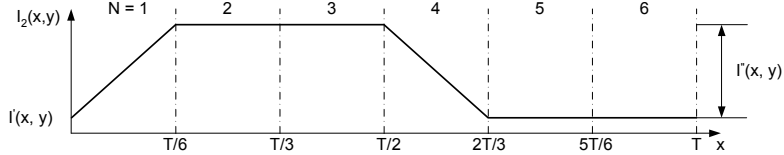
In this research, a DLP video projector was used to project the trapezoidal fringe patterns to the object. The images are captured by a CCD camera. The major potential error sources are the image defocus error due to limited depth of focus of both the projector and the camera and the nonlinear gamma curve of the projector. The nonlinear gamma curve can be corrected by software. (see Section 3.2.4). However, the residual nonlinearity can still cause errors that cannot be ignored. The following sections discuss the effects of these two error sources.

4.3.1 Image defocus error

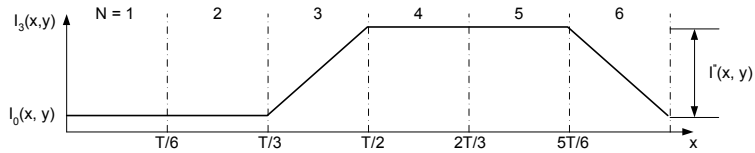
In the sinusoidal phase-shifting method, image defocus will not cause major errors because a sinusoidal pattern will still be a sinusoidal pattern when the image



(a) Cross section of I_1



(b) Cross section of I_2



(c) Cross section of I_3

Figure 4.1: Phase-shifted trapezoidal fringe patterns.

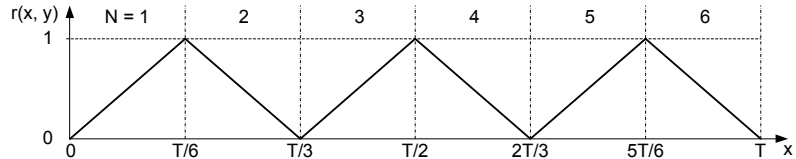


Figure 4.2: Cross section of the intensity-ratio map.

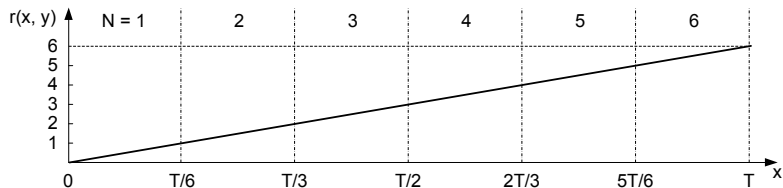


Figure 4.3: Cross section of the intensity-ratio map after removal of the triangles.

is defocused, even though the fringe contrast may be reduced. However, in the trapezoidal phase-shifting method, image defocus will blur the trapezoidal pattern, which may cause errors that cannot be ignored. In order to quantify this error, we use a Gaussian filter to simulate the defocusing effect. By changing the size of the filter window, we can simulate the level of defocus and calculate the corresponding error. Following is the equation for the intensity ratio $r(x,y)$ when the fringe images

are defocused:

$$r(x, y) = \frac{I_{med}(x, y) \otimes G(x, y) - I_{min}(x, y) \otimes G(x, y)}{I_{max}(x, y) \otimes G(x, y) - I_{min}(x, y) \otimes G(x, y)}, \quad (4.7)$$

where symbol \otimes denotes the convolution operation and

$$G(x, y) = \frac{1}{2\pi\sigma^2} e^{-\frac{(x-\bar{x})^2 + (y-\bar{y})^2}{2\sigma^2}},$$

is a 2D Gaussian filter, which is a 2D normal distribution with standard deviation σ and mean point coordinate (\bar{x}, \bar{y}) .

To simplify the analysis without loosing its generality, we consider only a 1-D case (along x-axis) within regions $N = 1$ and $N = 2$. Assuming the size of the filter window to be $(2M + 1)$ pixels, we obtain the discrete form of the intensity ratio function as

$$r_{def}(x, y) = \begin{cases} \frac{\sum_{n=-M}^{T/6-x-1} [6(x+n)/T]G(n) + \sum_{n=T/6-x}^M G(n)}{\sum_{n=-M}^{T/6-x-1} G(n) + \sum_{n=T/6-x}^M G(n)[2-6(x+n)/T]} & x \in [0, T/6) \\ \frac{\sum_{n=-M}^{T/6-x-1} G(n) + \sum_{n=T/6-x}^M G(n)[2-6(x+n)/T]}{\sum_{n=-M}^{T/6-x-1} [6(x+n)/T]G(n) + \sum_{n=T/6-x}^M G(n)} & x \in [T/6, T/3) \end{cases}, \quad (4.8)$$

where

$$G(n) = \begin{cases} e^{-\frac{n^2}{2\sigma^2}} / \sum_{n=-M}^M e^{-\frac{n^2}{2\sigma^2}} & n \in [-M, M] \\ 0 & \text{otherwise} \end{cases},$$

is a 1-D discrete Gaussian filter with standard deviation σ . To show the effect of image defocus on intensity ratio, we calculate $r_{def}(x)$ for a filter window size of T and compare it with $r(x)$, which is the intensity ratio without image defocus. The results are shown in Figure 4.4. We can see that image defocus causes the originally linear intensity ratio to become nonlinear, which introduces distortion to the measured shape. To quantify the effect of image defocus on intensity ratio as a function of the level of defocus, we define error E as follows:

$$E = \{max[r_{def}(x) - r(x)] - min[r_{def}(x) - r(x)]\}/6. \quad (4.9)$$

Figure 4.5 shows how this error value changes as the size of the filter window increases from 0 to T . From this figure, we see that the error increases with the window size up until the window size reaches about $0.7T$. After that, the error is stabilized

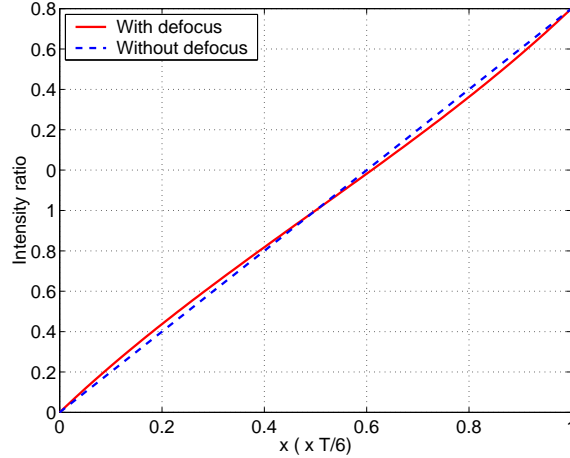


Figure 4.4: Comparison of the intensity ratios with and without image defocus. Here the filter window size used in the calculation is T .

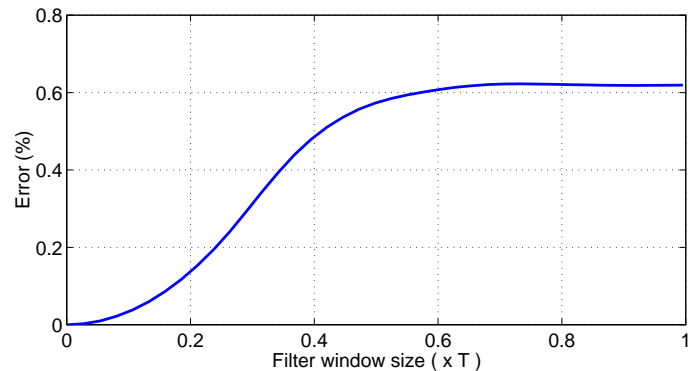


Figure 4.5: Maximum error due to image defocus.

to a relatively small value of 0.6%. This phenomenon is due to the fact that as the window size, or the defocus level, is increased, the trapezoidal pattern becomes increasingly like a sinusoidal pattern and once becoming a sinusoidal pattern, the error does not change anymore even if it is further defocused. Figure 4.6 shows how the trapezoidal pattern is blurred for different window sizes. Clearly, when the window size is increased to T , the pattern is already like a sinusoidal pattern. This error depends on the window size of the filter or the level of defocus.

To understand why for such dramatic defocusing of the fringe pattern the error is still limited to only about 0.6%, we can look at the transitional area between regions $N = 1$ and $N = 2$, which is shown in Figure 4.7. We can see that the

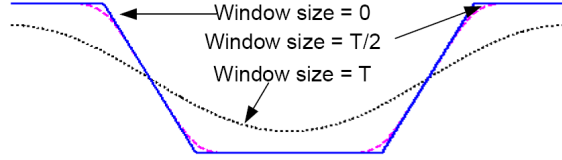


Figure 4.6: Blurring effect of the trapezoidal fringe pattern due to image defocus.

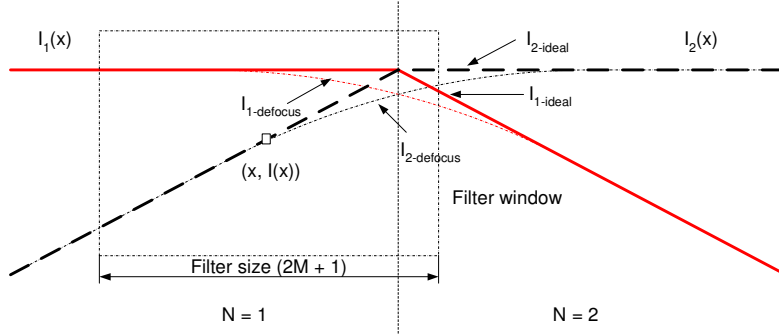


Figure 4.7: Enlarged view of the blurring effect of the trapezoidal fringe pattern in the borderline area between regions $N = 1$ and $N = 2$.

cross sections of $I_1(x, y)$ and $I_2(x, y)$ are symmetrical with respect to the borderline of the two regions. Even when the fringe patterns are defocused, this symmetry is maintained. This results in similar drops in $I_1(x, y)$ and $I_2(x, y)$ in the regions close to the borderline, which reduces the error in the calculation of the ratio $I_1(x, y)/I_2(x, y)$. At the borderline of the two regions, the ratio, which still equals to one, does not change even after the images are defocused.

In summary, even though the trapezoidal phase-shifting method is still sensitive to the defocusing effect (unlike the sinusoidal phase-shifting method), the resulting error is small, in particular when compared to conventional intensity ratio based methods. For example, for a filter window size of $0.1T$, the method proposed by Savarese *et al.* will have an error of more than 53% [34], while the error of the trapezoidal phase-shifting method will only be approximately 0.03%, which is dramatically smaller. Therefore, the trapezoidal phase-shifting method is capable of measuring objects with large depth with limited errors.

4.3.2 Nonlinearity error

The relationship between the input grayscale values and the grayscale captured by the camera should be linear. Otherwise it will result in errors in the final measurement results. Since the gamma curve of the projector is usually not linear, we use a software compensation method to linearize this relationship. However, the relationship after compensation may still not be exactly linear. This nonlinearity directly affects the measurement accuracy. In fact, the shape of the ratio curve in each region, which should be linear ideally, is a direct replica of the gamma curve, if no defocusing effect is considered. Therefore, reducing the nonlinearity of the gamma curve is critical to the measurement accuracy.

4.4 Experiments

To verify its performance, we implemented the trapezoidal phase-shifting method in our real-time 3D shape measurement system. To increase the image resolution, we used periodic patterns with a pitch of 12 pixels per fringe. The 3D result was obtained after removing the periodical discontinuity by adding or subtracting multiples of 6, which is similar to phase unwrapping in the sinusoidal phase-shifting method.

Figure 4.8 shows the measured shape of a cylindrical part with a diameter of 200 mm. Figure 4.8(a) shows the cross section of the measured patch as compared to the ideal curve, Figure 4.8(b) shows the difference or error, and Figure 4.8(c) shows the 3D plot. As can be seen from the result, the measurement is accurate (the peak-to-peak error is approximately 0.6 mm) for most part of the surface except for the left 20 mm or so, which shows a significant error. This large error is due to the slope of the surface in that area, which makes the surface almost parallel to the projection light. Figure 4.9 shows the measured result of a plaster sculpture head. The measurement resolution is comparable to that of the sinusoidal phase-shifting method. The advantage lies in the processing speed of the fringe patterns, thanks to the simple intensity-ratio calculation as opposed to the phase calculation with an arctangent function in the sinusoidal phase-shifting method. This enables potential real-time 3D shape measurement for objects with dynamically changing

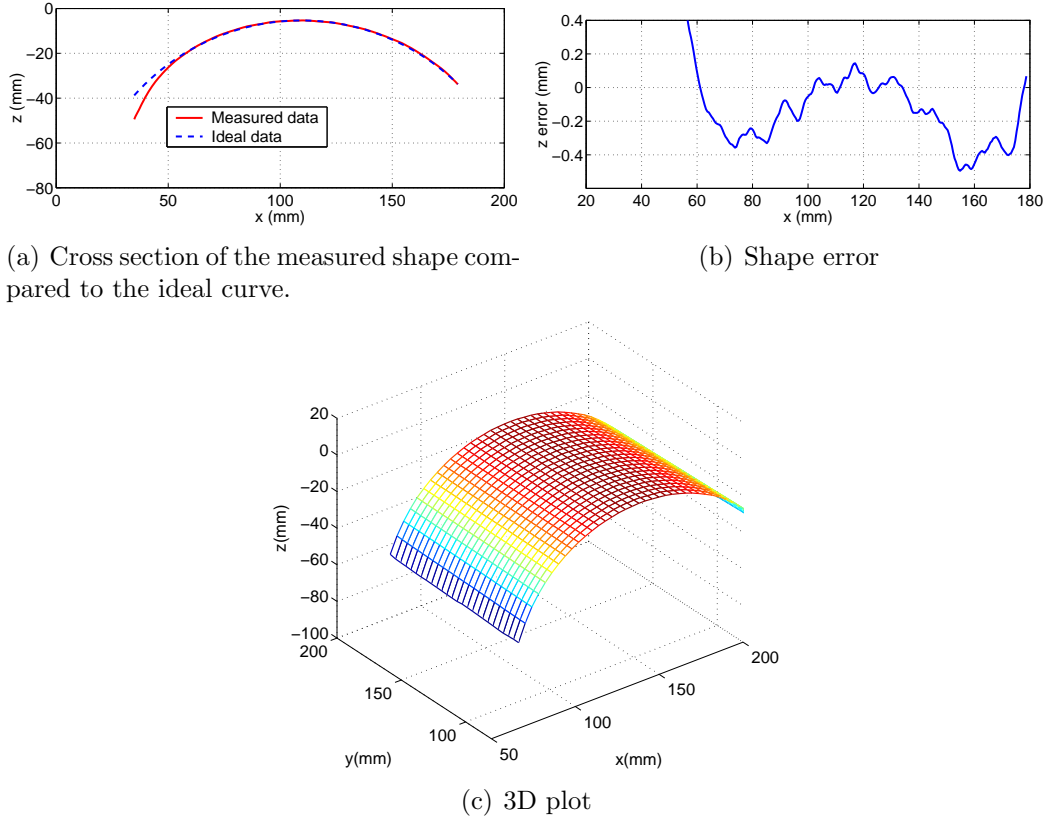


Figure 4.8: 3D shape measurement of a cylindrical part.

surface geometry. Figure 4.10 shows the measured result of a live human face. In this case, we used periodical patterns with a pitch of 30 pixels per fringe. At an image size of 532×500 pixels, it took approximately 4.6 ms to obtain the ratio map, but 20.8 ms to compute the phase map with a Pentium 4, 2.8 GHz personal computer. These experiments confirmed that the proposed trapezoidal phase-shifting method could potentially be used to measure the 3D surface shapes of slowly moving objects in real time.

4.5 Conclusions

We described a novel structured light method, trapezoidal phase-shifting method, for 3D shape measurement in this chapter. Compared to the traditional sinusoidal phase-shifting methods, this method has the advantage of a faster processing speed because it calculates a simple intensity ratio rather than phase, which is a computa-

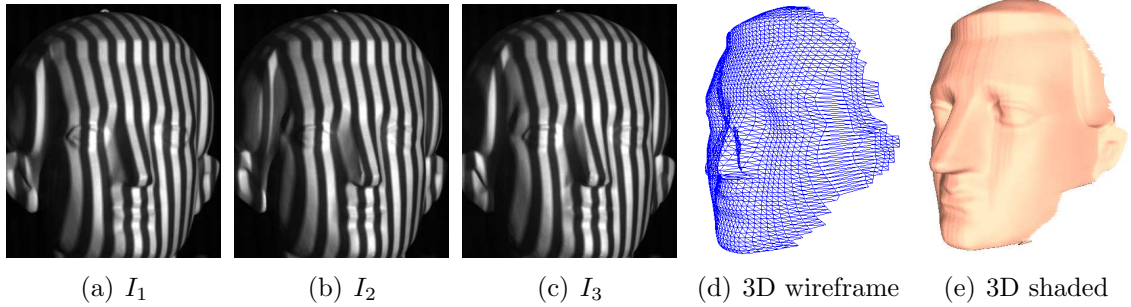


Figure 4.9: 3D shape measurement of a plaster sculpture.

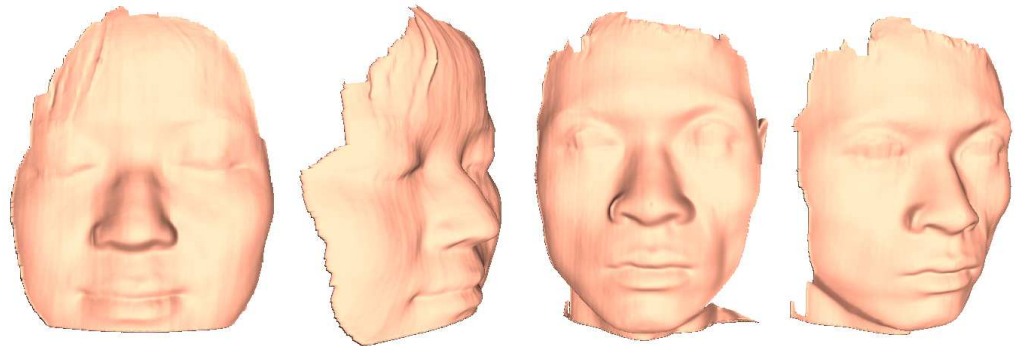


Figure 4.10: 3D shape measurement of human faces.

tionally more time-consuming arctangent function. The depth resolution is similar. The disadvantage is that image defocus may cause some errors, even though they are quite small. Compared to the traditional intensity-ratio based methods, this method has a depth resolution that is six times better. It is also significantly less sensitive to image defocus, which allows it to be used to measure objects with large depth variations. Experimental results demonstrated that the newly proposed method could be used to provide 3D surface shape measurements for both static and dynamically changing objects. However, for measurement requiring high accuracy, the small error caused by image defocusing is non-negligible.

Chapter 5

Fast Phase-wrapping Algorithm

Trapezoidal phase-shifting algorithm has the advantages of high processing speed, but its accuracy is affected by image defocusing. From analysis in Chapter 4, we know that the maximum error caused by image defocusing is 0.6%, which occurs when the trapezoidal pattern becomes sinusoidal pattern due to excessive defocus. In this chapter, we propose a new three-step algorithm which replaces the calculation of the arctangent function with a simple ratio calculation and therefore is much faster than the traditional algorithm. The phase error caused by this replacement is compensated for by use of a look-up-table (LUT). Our experimental results show that the error caused by this fast processing algorithm is negligible. The adoption of this new algorithm enabled us to successfully build a high-resolution, real-time 3D shape measurement system that captures, reconstructs, and displays the 3D shape of measured objects in real time at a speed of 40 frames per second and a resolution of 532×500 pixels, all with an ordinary personal computer.

5.1 Introduction

Sinusoidal three-step phase-shifting algorithm has the merit of fast and accurate 3D shape measurement, and is feasible for real-time 3D measurement. However, our experiments show that even with the three-step algorithm, the image processing speed is not fast enough for real-time 3D shape reconstruction. The bottleneck lies in the calculation of phase, which involves a computationally time-consuming arctangent function. To solve this problem, we propose a fast phase-wrapping algorithm,

which replaces the calculation of the arctangent function with a simple ratio calculation and therefore is much faster than the traditional algorithm. The phase error caused by this replacement is compensated for by use of a look-up-table (LUT). Our simulation and experimental results show that both the new algorithm and the traditional algorithm generate similar results, but the new algorithm is at least 3.4 times faster. The adoption of this new algorithm enables us to successfully build a high-resolution, real-time 3D shape measurement system that captures, reconstructs, and displays the 3D shape of the measured object in real time at a speed of 40 frames per second and a resolution of 532×500 pixels, all with an ordinary personal computer.

Section 5.2 explains the principle of the fast phase-wrapping algorithm. Section 5.3 analyzes the processing error and proposes an error reduction method. Section 5.4 shows some experimental results. And Section 5.5 concludes the chapter.

5.2 Principle

The traditional three-step phase-shifting algorithm works well in terms of accuracy [73]. However, due to the need of computing an arctangent function for phase, the reconstruction of 3D shape is relatively time consuming. This section addresses the principle of the proposed fast phase-wrapping algorithm based on the trapezoidal phase-shifting algorithm discussed in Chapter 4.

5.2.1 Fourier analysis of the trapezoidal phase-shifting algorithm

Sinusoidal fringe patterns can be viewed as severely defocused trapezoidal fringe patterns. From discussion in Chapter 4, we know that the error caused by image defocus peaks at approximately 0.6%, which is rather small. This means that even if we use the algorithm developed for the trapezoidal fringe patterns to process sinusoidal fringe patterns, the error should be limited. Here we use Fourier analysis to show this indeed the case.

From the plots shown in Figure 4.1, we know that the trapezoidal fringe pat-

terms are each shifted by 1/3 period, T . That is

$$I_2(x, y) = I_1\left(x - \frac{T}{3}, y\right), \quad (5.1)$$

$$I_3(x, y) = I_2\left(x - \frac{T}{3}, y\right). \quad (5.2)$$

Since the shape of the first pattern is symmetric to y axis, its Fourier expansion is a cosine series along x -axis,

$$I_1(x, y) = \frac{a_0}{2} + \sum_{m=1}^{\infty} a_m \cos\left(\frac{2\pi m}{T}x\right), \quad (5.3)$$

where

$$a_0 = \frac{2}{T} \int_0^T I_1(x, y) dx = 1, \quad (5.4)$$

$$\begin{aligned} a_m &= \frac{2}{T} \int_0^T I_1(x, y) \cos\left(\frac{2\pi m}{T}x\right) dx \\ &= \frac{12}{(m\pi)^2} \sin\left(\frac{m\pi}{2}\right) \sin\left(\frac{m\pi}{6}\right). \end{aligned} \quad (5.5)$$

Therefore,

$$I_1(x, y) = \frac{1}{2} + \sum_{m=1}^{\infty} \frac{12}{(m\pi)^2} \sin\left(\frac{m\pi}{2}\right) \sin\left(\frac{m\pi}{6}\right) \cos\left(\frac{2\pi m}{T}x\right). \quad (5.6)$$

From Equations 5.1, 5.2 and 5.6, we obtain

$$I_2(x, y) = \frac{1}{2} + \sum_{m=1}^{\infty} \frac{12}{(m\pi)^2} \sin\left(\frac{m\pi}{2}\right) \sin\left(\frac{m\pi}{6}\right) \cos\left[\frac{2\pi m}{T}\left(x - \frac{T}{3}\right)\right]. \quad (5.7)$$

$$I_3(x, y) = \frac{1}{2} + \sum_{m=1}^{\infty} \frac{12}{(m\pi)^2} \sin\left(\frac{m\pi}{2}\right) \sin\left(\frac{m\pi}{6}\right) \cos\left[\frac{2\pi m}{T}\left(x - \frac{2T}{3}\right)\right]. \quad (5.8)$$

For region $N = 1$, $x \in [0, T/6]$, the intensity ratio in Equation 4.4 can be obtained

as,

$$r(x, y) = \frac{\sum_{m=1}^{\infty} \frac{1}{m^2} \sin\left(\frac{m\pi}{2}\right) \cos\left(\frac{m\pi}{6}\right) \sin\left[\frac{2m\pi}{T}\left(x - \frac{T}{2}\right)\right]}{\sum_{m=1}^{\infty} \frac{1}{m^2} \sin\left(\frac{m\pi}{2}\right) \cos\left(\frac{m\pi}{6}\right) \sin\left[\frac{2m\pi}{T}\left(x - \frac{T}{3}\right)\right]}. \quad (5.9)$$

By observing Equation 5.9, we see that the $r(x, y)$ is determined by $1\times$, $5\times$, $7\times$, \dots , frequency components only. Since comparing to the $1\times$ frequency component, the $5\times$, and $7\times$ frequency components are $1/25$ and $1/49$ smaller respectively, $r(x, y)$ can be approximated by including only the $1\times$ frequency component without causing

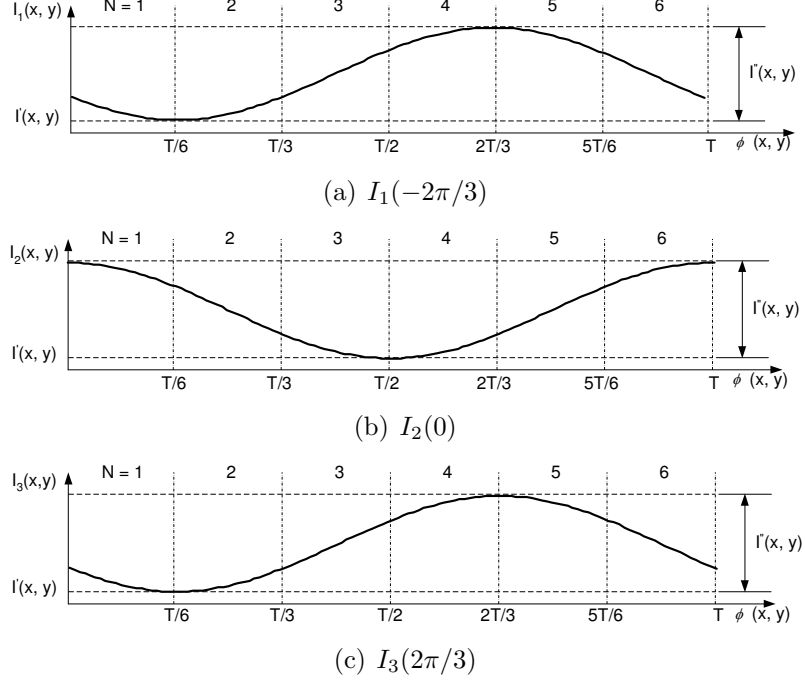


Figure 5.1: Cross sections of the three phase-shifted sinusoidal patterns.

significant errors. However, when only the $1\times$ frequency component is included, the trapezoidal fringe pattern effectively becomes a sinusoidal fringe pattern. Therefore, we can conclude that using the algorithm developed for the trapezoidal phase-shifting method to process sinusoidal fringe patterns will not result in significant error.

5.2.2 Fast phase-wrapping algorithm

Similar to trapezoidal phase-shifting algorithm, the sinusoidal fringe images can be evenly divided into 6 regions in one period ($T = 2\pi$). Figure 5.1 shows the cross sections of the sinusoidal fringe patterns. We use the same equation (Equation 4.4) developed for the trapezoidal phase-shifting method to calculate the intensity ratio. That is

$$r(x, y) = \frac{I_{med}(x, y) - I_{min}(x, y)}{I_{max}(x, y) - I_{min}(x, y)} . \quad (5.10)$$

where $I_{min}(x, y)$, $I_{med}(x, y)$ and $I_{max}(x, y)$ are the minimum, median, and maximum intensities of the three patterns for point (x, y) . The value of $r(x, y)$ ranges from 0 to 1. Figure 5.2 shows the cross section of the intensity ratio map. Similarly, the

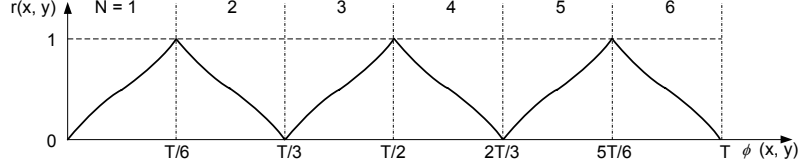


Figure 5.2: Cross section of the intensity ratio map.

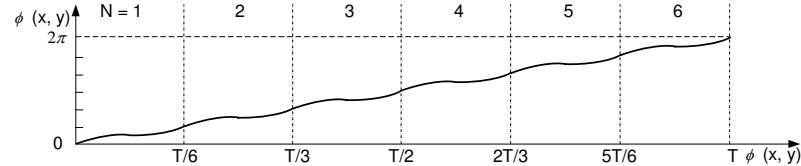


Figure 5.3: Cross section of the intensity ratio map after removal of the triangular shape.

triangular shape can be removed to obtain wrapped intensity ratio map by using Equation 4.5. The phase can then be calculated by the following equation,

$$\phi(x, y) = \frac{\pi}{3} \left[2 \times \text{round} \left(\frac{N}{2} \right) + (-1)^N r(x, y) \right], \quad (5.11)$$

whose value ranges from 0 to 2π , as shown in Figure 5.3. As we can see from the figure that the phase calculation is not accurate, but with a small error. In Section 5.3, we will analyze this error and discuss how this error can be compensated for.

If multiple fringes are used, the phase calculated by Equation 5.11 will result in a sawtooth-like shape, just as in the traditional phase shifting algorithm. Therefore, the traditional phase-unwrapping algorithm can be used to obtain the continuous phase map.

5.3 Error Analysis and Compensation

Fast phase-wrapping algorithm has the advantage of fast processing speed over traditional phase shifting algorithm. However, this method makes the linear phase value $\phi(x, y)$ to be nonlinear, as shown in Figure 5.3, which produces error. In this section, we discuss the error caused by applying fast phase-wrapping algorithm for sinusoidal patterns first and then propose an error compensation method.

From Figure 5.3, we see that the error is periodical and the pitch is $\pi/3$. Therefore, we only need to analyze the error in one period, say $\phi(x, y) \in [0, \pi/3]$. In this period, $I_h(x, y) = I_2(x, y)$, $I_m(x, y) = I_1(x, y)$, and $I_l(x, y) = I_3(x, y)$. By substituting Equations 2.11 into Equation 5.10, we obtain

$$r(\phi) = \frac{I_1 - I_3}{I_2 - I_3} = \frac{1}{2} + \frac{\sqrt{3}}{2} \tan\left(\phi - \frac{\pi}{6}\right). \quad (5.12)$$

The right-hand side of this equation can be considered as the sum of a linear and a nonlinear terms. That is

$$r(\phi) = \frac{\phi}{\pi/3} + \Delta r(\phi), \quad (5.13)$$

where the first term represents the linear relationship between $r(x, y)$ and $\phi(x, y)$ and the second term $\Delta r(x, y)$ is the nonlinearity error, which can be calculated as follows:

$$\begin{aligned} \Delta r(\phi) &= r(\phi) - \frac{\phi}{\pi/3} \\ &= \frac{1}{2} + \frac{\sqrt{3}}{2} \tan\left(\phi - \frac{\pi}{6}\right) - \frac{\phi}{\pi/3}. \end{aligned} \quad (5.14)$$

Figure 5.4(a) shows the plots of both the ideal linear ratio and the real nonlinear ratio. Their difference, which is similar to a sine wave in shape, is shown in Figure 5.4(b). By taking the derivative of $\Delta r(x, y)$ with respect to $\phi(x, y)$ and setting it to zero, we can determine that when

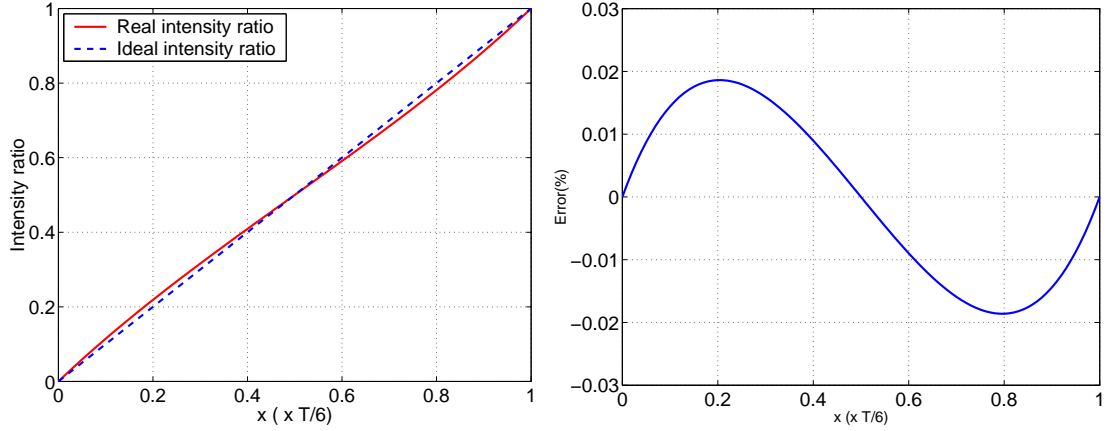
$$\phi(\phi) = \frac{\pi}{6} \pm \arccos\left(\sqrt{\sqrt{3}\pi/6}\right), \quad (5.15)$$

the ratio error reaches its maximum and minimum values respectively as

$$\Delta r(\phi)_{max} = \Delta r(\phi)|_{\phi=\phi_1} = 0.0186, \quad (5.16)$$

$$\Delta r(\phi)_{min} = \Delta r(\phi)|_{\phi=\phi_2} = -0.0186. \quad (5.17)$$

Therefore, the maximum ratio error is $\Delta r(\phi)_{max} - \Delta r(\phi)_{min} = 0.0372$. Since the maximum ratio value for the whole period is 6, the maximum ratio error in terms of percentage is $0.0372/6 = 0.6\%$. Even though this error is relatively small, it needs to be compensated for when accurate measurement is required.



(a) Nonlinear ratio ramp in region $N = 1$ (b) Error caused by the nonlinear approximation

Figure 5.4: Error caused by the fast phase-wrapping algorithm.

Since the ratio error is a systematic error, it can be compensated for by using a LUT method. In this research, an 8-bit camera is used. Therefore the LUT is constructed with 256 elements, which represent the error values determined by $\Delta r(\phi)$. If a higher-bit-depth camera is used, the size of the LUT should be increased accordingly. Because of the periodical nature of the error, this same LUT can be applied to all six regions.

5.4 Experiments

To verify the effectiveness of the proposed algorithm experimentally, we used a projector to project sinusoidal fringe patterns onto the object and an 8-bit black-and-white (B/W) CCD camera with 532×500 pixels to capture the three phase-shifted fringe images. First, we used a flat board as the target object. The captured three fringe images are shown in Figures 5.5(a) – 5.5(c). For comparison, we applied both the traditional algorithm and the newly proposed algorithm to the same fringe images. Figures 5.6(a), 5.6(b), and 5.6(c) show the error of the traditional phase-wrapping algorithm, the error of the fast phase-wrapping algorithm before error compensation, and the error of the fast phase-wrapping algorithm after error compensation, respectively. From Figure 5.6(b), we see that the phase error of the fast phase-wrapping algorithm before error compensation is approximately 0.037, which

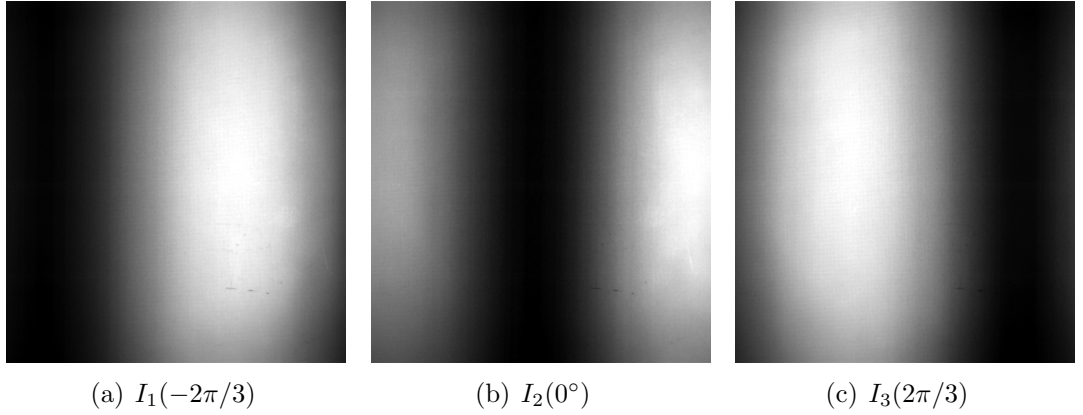


Figure 5.5: Fringe images of a flat board captured by a 8-bit B/W CCD camera.

agrees well with the theoretical analysis. After error compensation, this error, which is shown in Figure 5.6(c), is significantly reduced and is comparable to that of the traditional phase-wrapping algorithm as shown in Figure 5.6(a).

Next, we measured an triangular shape object with multiple fringe images. The captured fringe images are shown in Figures 5.7(a)– 5.7(c). The reconstructed 3D shapes using the traditional algorithm and the proposed algorithm to these fringe images are shown in Figures 5.7(d) and 5.7(e), respectively. The difference between these reconstructed result is shown in Figure 5.7(f), which is approximately ± 0.002 mm and is negligible.

Finally, we measured an object with more complex surface geometry, a Lincoln head sculpture. The 2-D photo of the object is shown in Figure 5.8(a). The reconstructed 3-D shapes based on the traditional and the proposed phase-wrapping algorithms are shown in Figures 5.8(b) and 5.8(c), respectively. We can see that the two results show almost no difference.

In our experiment, we used an ordinary personal computer (Pentium 4, 2.8GHz) for image processing. The traditional phase-wrapping algorithm took 20.8 ms, while the proposed new algorithm took only 6.1 ms, which was 3.4 times less. The improvement in processing speed is significant.

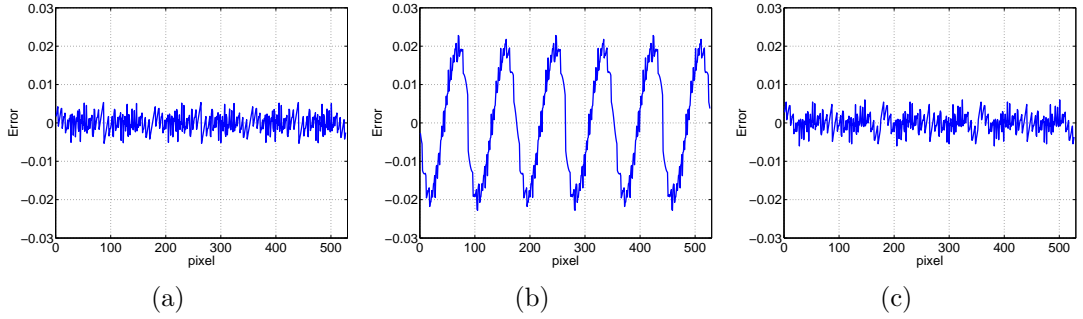


Figure 5.6: Residual phase error. (a) With the traditional algorithm. (b) With the proposed algorithm before error compensation. (c) With the proposed algorithm after error compensation.

5.5 Conclusion

In this chapter, we proposed a fast phase-wrapping algorithm based on intensity ratio calculation and LUT error compensation for real-time 3-D shape measurement. This algorithm originated from the previously proposed trapezoidal phase shifting method, which was aimed at improving the processing speed of the fringe images. In this research, we found that the same algorithm developed for the trapezoidal fringe patterns could be used to process sinusoidal fringe images with a small error, which could be easily eliminated by using a LUT method. This finding resulted in a new phase-wrapping algorithm that is 3.4 times faster than and just as accurate as the traditional phase-wrapping algorithm. Experimental results demonstrated the effectiveness of the proposed algorithm. We have successfully implemented this algorithm in our real-time 3-D shape measurement system, which has a frame rate of 40 frames per second and a resolution of 532×500 points.

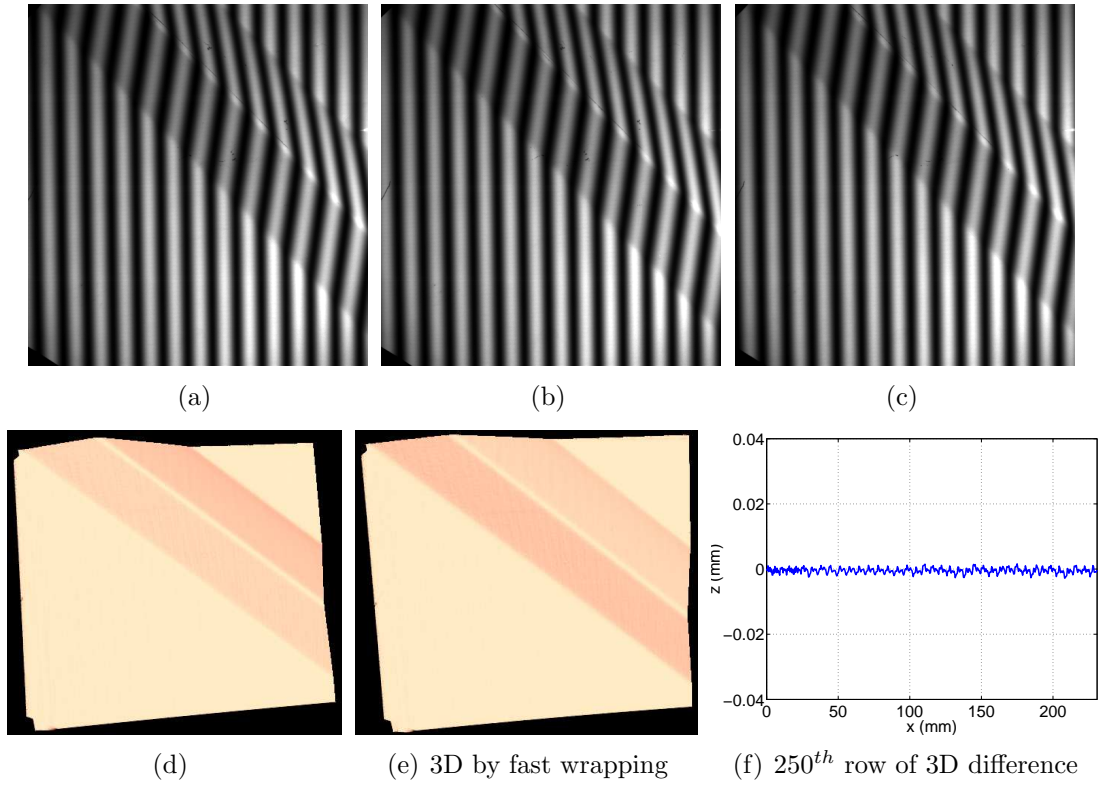


Figure 5.7: Reconstructed 3D result of a sheet metal by fast phase-wrapping algorithm. (a) $I_0(-2\pi/3)$. (b) $I_1(0)$. (c) $I_2(2\pi/3)$. (d) 3D shape using the traditional phase-wrapping algorithm. (e) 3D shape using the fast phase-wrapping algorithm. (f) 3D shape difference using the traditional and the fast phase-wrapping algorithms.

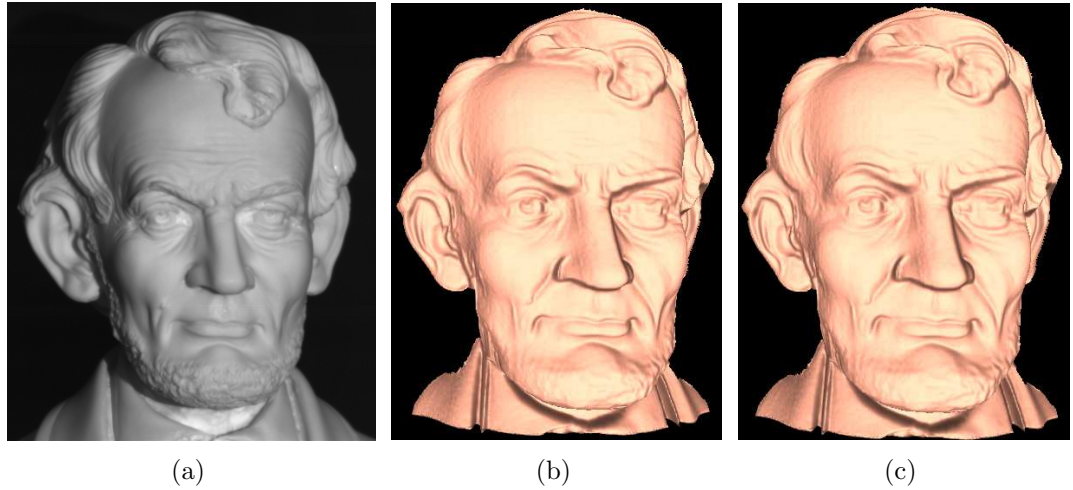


Figure 5.8: 3D reconstruction results of sculpture Lincoln. (a) 2D photo. (b) 3D shape using the traditional phase-wrapping algorithm. (c) 3D shape using the fast phase-wrapping algorithm.

Chapter 6

Error Compensation Algorithm

This chapter addresses a novel error compensation technique for reducing the measurement error caused by nonsinusoidal waveforms in the phase-shifting method. For 3D measurement systems using commercial video projectors, the non-sinusoidal nature of the projected fringe patterns as a result of the nonlinear projection response curve (or gamma curve) of the projectors causes significant phase measurement error and therefore shape measurement error. The proposed error compensation method is based on our finding that the phase error due to non-sinusoidal fringe patterns depends only on the nonlinearity of the projector's gamma curve. Therefore, if the projector's gamma curve is calibrated and the phase error due to the nonlinearity of the gamma curve is calculated, a look-up-table (LUT) that stores the phase error can be constructed for error compensation. Our experimental results demonstrate that by using the proposed method, the measurement error can be reduced by 10 times. In addition to phase error compensation, a similar method is also proposed to correct the non-sinusoidality of the fringe patterns for the purpose of generating a more accurate flat image of the object for texture mapping, which is important for applications in computer vision and computer graphics.

6.1 Introduction

With the development of digital display technologies, commercial digital video projector are more and more broadly used in 3D measurement systems. The error due to non-sinusoidal waveforms is one of the major errors of 3D measurement systems

based on the phase shifting method. The non-sinusoidal nature of the projected fringe patterns as a result of the nonlinear gamma curve of the projectors causes significant phase measurement error and therefore shape measurement error. Previously proposed methods, such as, double three-step phase-shifting algorithm [74], 3+3 phase-shifting algorithm [73], direct correction of the nonlinearity of the projector's gamma curve [65], demonstrated significant reduction of the measurement error, but the residual error remains non-negligible. In this research, we propose a novel error compensation method that can produce significantly better results. This method is developed based on our finding that the phase error due to non-sinusoidal fringe patterns depends only on the nonlinearity of the projector's gamma curve. Therefore, if the projector's gamma curve is calibrated and the phase error due to the nonlinearity of the gamma curve is calculated, a look-up-table (LUT) that stores the phase error can be constructed for error compensation. In addition to error compensation, a similar method is also proposed to correct the non-sinusoidality of the fringe patterns for the purpose of generating a more accurate flat image of the object for texture mapping, which is important for applications in computer vision and computer graphics.

In this chapter, Section 6.2 introduces the theoretical background of the this error compensation method, Section 6.3 shows simulation results, Section 6.4 shows experimental results, Section 6.5 discusses the advantages and limitations of the method, and Section 6.6 concludes the chapter.

6.2 Principle

6.2.1 Phase correction

The images captured by the camera is formed through the procedure illustrated in Figure 6.1. Without loss of generality, we consider only the three-step phase-shifting algorithm with a phase shift of $2\pi/3$ (see Section 2.2.3). Let us assume that the projector's input sinusoidal fringe images generated by a computer have the

intensity as,

$$I_k(x, y) = a_0 \{1 + \cos[\phi(x, y) + \frac{2(k-2)\pi}{3}]\} + b_0, \quad (6.1)$$

where $k = 1, 2, 3$, a_0 is the dynamic range of the fringe images, b_0 is the bias. After being projected by the projector, the output intensity of the fringe images becomes,

$$I_k^p(x, y) = f_k(I_k), \quad (6.2)$$

where $f_k(I)$ is a function of I , which represents the real projection response of the projector to the input intensity in channel k . If we assume that the projector projects light onto a surface with reflectivity $r(x, y)$ and the ambient light is $a_1(x, y)$, the reflected light intensity is

$$I_k^o(x, y) = r(x, y)[I_k^p(x, y) + a_1(x, y)], \quad (6.3)$$

The reflected image is captured by a camera with a sensitivity of α , where we assume the camera is linear response to input light intensity, namely, α is constant. Then the intensity of the image captured by the camera is,

$$I_k^c(x, y) = \alpha[I_k^o(x, y) + a_2(x, y)], \quad (6.4)$$

where $a_2(x, y)$ represents ambient light entering the camera.

Based on the three-step phase-shifting algorithm, phase $\phi(x, y)$ can be calculated as follows:

$$\begin{aligned} \phi(x, y) &= \tan^{-1} \left(\sqrt{3} \frac{I_1^c - I_3^c}{2I_2^c - I_1^c - I_3^c} \right), \\ &= \tan^{-1} \left\{ \frac{\sqrt{3} \{ \alpha[r(I_1^p + a_1) + a_2] - \alpha[r(I_3^p + a_1) + a_2] \}}{2\alpha[r(I_2^p + a_1) + a_2] - \alpha[r(I_1^p + a_1) + a_2] - \alpha[r(I_3^p + a_1) + a_2]} \right\}, \\ &= \tan^{-1} \left(\sqrt{3} \frac{I_1^p - I_3^p}{2I_2^p - I_1^p - I_3^p} \right). \end{aligned} \quad (6.5)$$

From this equation we can see that phase $\phi(x, y)$ is independent of the response of the camera, the reflectivity of the object, and the intensity of the ambient light. This indicates that the phase error due to non-sinusoidal waveforms depends only on the nonlinearity of the projector's gamma curve. Therefore if the projector's gamma curve is calibrated and the phase error due to the nonlinearity of the gamma curve

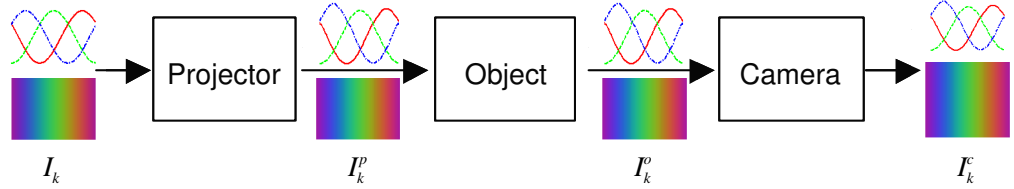


Figure 6.1: Camera image generation procedure.

is calculated, a look-up-table (LUT) that stores the phase error can be constructed for error compensation.

The following steps describe the procedure of constructing the LUT:

- (1) Sample projection response functions. A series of gray scale images with different grayscale values I_n , $n = 1, 2, \dots, N$, are sent to the projector. The projector projects the gray scale images with intensity values $f_k(I_n)$ onto a white board. The reflected images are captured by the camera and the intensities at the center of the images, I_{kn}^c , are calculated. The set of samples (I_n, I_{kn}^c) is recorded.
- (2) Approximate the projection response functions f_k . The projection response functions $f_k(I_n)$ are constructed through fitting the sample points by spline curves. Figure 6.2 illustrates a typical example of our reconstructed projection response curves for R, G, B channels. It is obvious that the curves are non-linear and unbalanced.
- (3) Find a straight line $\hat{f}(I)$, such that $\hat{f}(I_1) = \max\{f_k(I_1)\}$, $\hat{f}(I_N) = \min\{f_k(I_N)\}$, \hat{f} is considered the ideal projection response for all channels.
- (4) Compute real phase ϕ using Equation 6.5.
- (5) Compute the ideal phase $\hat{\phi}$ by replacing f_k in Equation 6.5 with \hat{f} .
- (6) Record the difference $\phi - \hat{\phi}$ and store $(\phi, \phi - \hat{\phi})$ in a phase error LUT.

The constructed phase error LUT can be used to correct phase error for real measurements. It only depends on the projection response functions f_k and can be

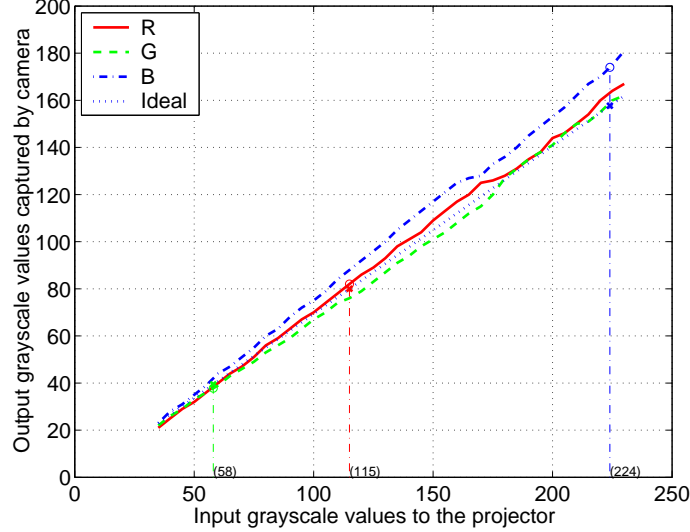


Figure 6.2: Typical projection response curve.

constructed once for all as long as the f_k 's are unchanged. The same method can be applied to correct nonsinusoidal fringe images, which is very important for many applications that require high quality texture.

6.2.2 Texture recovering

Ideally, the texture of image can be generated by averaging the three phase-shifted fringe images with $2\pi/3$ of phase shift. However, if the fringe images are not exactly sinusoidal, the texture image can not be correctly obtained by simple averaging. We found that the fringe images could be recovered by a solving reverse problem.

It is obvious that (ϕ, f_k) forms a one-to-one map in one period $\phi \in [0, 2\pi]$, and f_k is monotonous and invertible. Therefore, for a given phase value ϕ ranging from 0 to 2π , the corresponding points $(I_k, f_k(I_k))$ can be uniquely determined. Furthermore, its corresponding point $(I_k, \hat{f}(I_k))$ on the ideal projection response curve can also be determined. Hence, ratio $R_k := f_k/\hat{f}$ for any given ϕ is well defined. We can build a ratio map (ϕ, R_k) to correct the nonsinusoidal fringe images and to produce correct texture images by averaging the correct sinusoidal fringe images.

The following describes the procedure. Again, assume the camera is linear with

constant response α . Without loss of generality, we assume

$$\hat{f}(I_1) = \max\{f_k(I_1)\} = f_3(I_1),$$

$$\hat{f}(I_N) = \min\{f_k(I_N)\} = f_1(I_N),$$

Then the ideal projection response function is

$$\hat{f}(I) = \frac{f_1(I_N) - f_3(I_1)}{I_N - I_1}(I - I_1) + f_3(I_1).$$

Based on the virtual ideal linear projection response function, the camera image intensity is

$$I_{ideal}^c(x, y) = \alpha[r(x, y)(\hat{f}(I) + a_1(x, y)) + a_2(x, y)],$$

Then ratio,

$$R_k(x, y) = \frac{I_k^c}{I_{ideal}^c} = \frac{\alpha[r(f_k + a_1) + a_2]}{\alpha[r(\hat{f} + a_1) + a_2]} = \frac{r(f_k + a_1) + a_2}{r(\hat{f} + a_1) + a_2}, \quad (6.6)$$

If $a_1(x, y)$ and $a_2(x, y)$ are very small (near zero), then this equation can be approximated as

$$R_k(x, y) \approx \frac{f_k}{\hat{f}}. \quad (6.7)$$

From this equation we can see that ratio $R_k(x, y)$ is independent of the response of the camera, the reflectivity of the object, and the intensity of the ambient light. This means that the ratio map depends only on the nonlinearity of the projector's gamma curve. Similarly, a ratio map LUT can be constructed to correct the non-sinusoidality of the fringe images.

The following steps describe the procedure of constructing ratio map LUT:

- (1) Use Steps 1- 4 in phase error LUT construction procedures;
- (2) Find corresponding points of each phase value ϕ on three projection response curves (I_{kx}, f_k) as well as ideal response curves (I_{kx}, \hat{f}_k) .
- (3) Record the ratio R_k , and store (ϕ, R_k) in a LUT for fringe image correction.

These ratio maps can be used to correct the nonsinusoidal fringe images to make them sinusoidal. For example, for phase value at $\pi/4$, the corresponding point on each channel is unique (as shown in Figure 6.2), they are (115, 82.00), (58, 37.80), (224, 174.00) on the calibrated projection response curve. The ideal projection response curves are

$$\hat{f}(I) = \frac{162 - 23}{230 - 35}(I - 35) + 23.$$

The corresponding points for three channels on the ideal projection response curves are (115, 80.03), (58, 39.39), and (224, 157.72), respectively. The ratio map is then

$$\{(0.9760, 1.0421, 0.9064) | \phi = \pi/4\}.$$

This ratio LUT can be used for recovering the fringe images with wrapped phase value at $\phi = \pi/4$. After the fringe images are recovered to be ideally sinusoidal, we can use these images to reconstruct geometry correctly.

6.3 Simulation Results

A typical projection response curve of our system is shown in Figure 6.2. The usable grayscale value is shorter than the range from 0 to 255 because both ends are flat. If a projector's red, green, and blue color channels are encoded with I_1 , I_2 , and I_3 , respectively, and the input fringe images of the projector are ideally sinusoidal vertical stripes,

$$I_k(x, y) = 100\{1 + \cos[\frac{2\pi x}{p} + \frac{2(k-2)\pi}{3}]\} + 35, k = 1, 2, 3,$$

where p is the fringe period used. The cross sections of sinusoidal fringe images using projection response curves of Figure 6.2 are shown in Figure 6.3(a). After the fringe correction algorithm is applied, the cross sections of the fringe images are shown in Figure 6.3(b). It is clear that before correction, the fringe images are neither sinusoidal nor balanced. After correction, they are almost sinusoidal and balanced.

If we use the distorted fringe images to compute phase map directly, the phase error, as shown in Figure 6.4(a), is approximately 2.4%. After phase error correction using a small LUT, the phase error is reduced to 0.2% as illustrated in Figure 6.4(b).

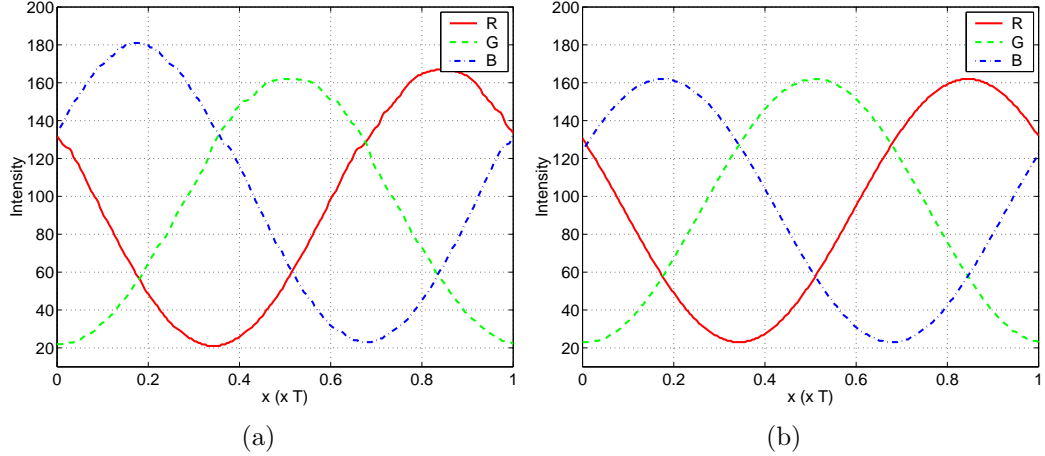


Figure 6.3: Cross section of simulated fringe images before and after correction. (a) Cross sections of fringe images without correction. (b) Cross sections of fringe images after correction.

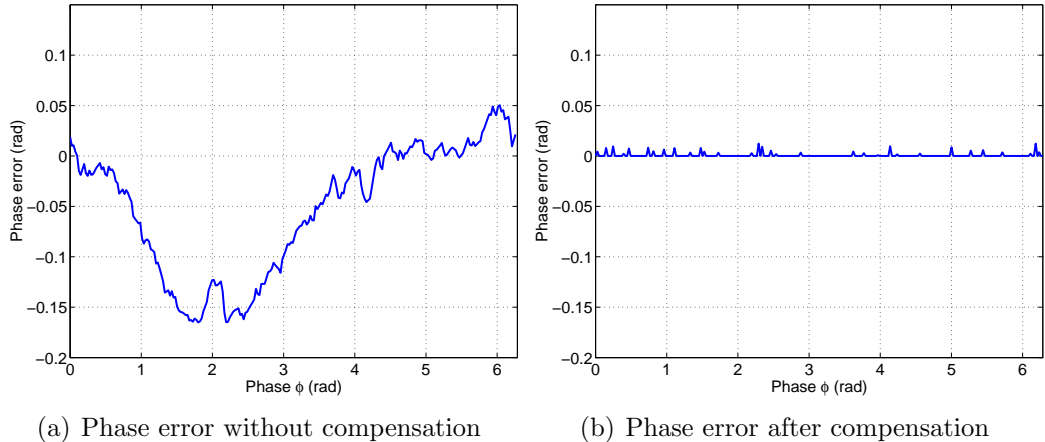


Figure 6.4: Phase error before and after error compensation.

Correcting fringes or correcting phase directly does not make any difference for simulation since the ambient light is ignored. However, for real captured images, they are slightly different due to the fact that the ambient lights, $a_1(x, y)$ and $a_2(x, y)$, are not zero, which will be explained in the next section.

6.4 Experimental Results

Our simulation results show that we can use small LUTs to correct phase error as well as fringe images. To verify that this method actually works, we implement

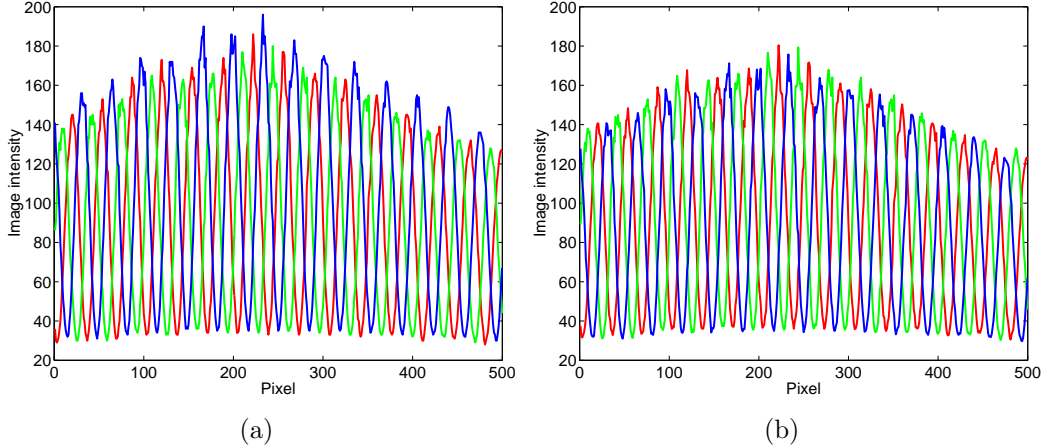


Figure 6.5: Fringe correction for real captured fringe images. (a) Cross section of captured fringe images. (b) Cross section of fringe images after correction.

implemented the algorithms in our real-time system. We first measured a flat board. Figure 6.5 shows the result. Figure 6.5(a) shows the cross sections of the originally acquired fringe images with the projection response curves shown in Figure 6.2. We see that the three fringe images are not well balanced. Figure 6.5(b) shows the cross sections of the fringe images after correction, which are more balanced.

Figure 6.6 shows a comparison of the reconstructed 3D results before and after correction. It is clear that correcting the phase error directly results in higher accuracy than correcting fringe images due to the existence of ambient light $a(x, y)$. The averaged 2D texture before and after correction are shown in Figure 6.7. The 2D texture without correction shows vertical stripes. After the correction, those stripes are barely seen and the image is sufficiently good for texture mapping purpose.

We also measured plaster models. Figure 6.8 shows the reconstructed 3D models before and after error compensation. The reconstructed 3D geometric surface after error compensation is very smooth. The first row is smooth head sculpture, and the second row is sculpture Zeus with richer geometric features. The first column shows the captured 3D models without error compensation, the second column shows the 3D results reconstructed by compensated fringe images, the third column shows the 3D results after correcting phase error directly, and the last column images are 3D results with corrected texture mapping. These experimental results confirmed that

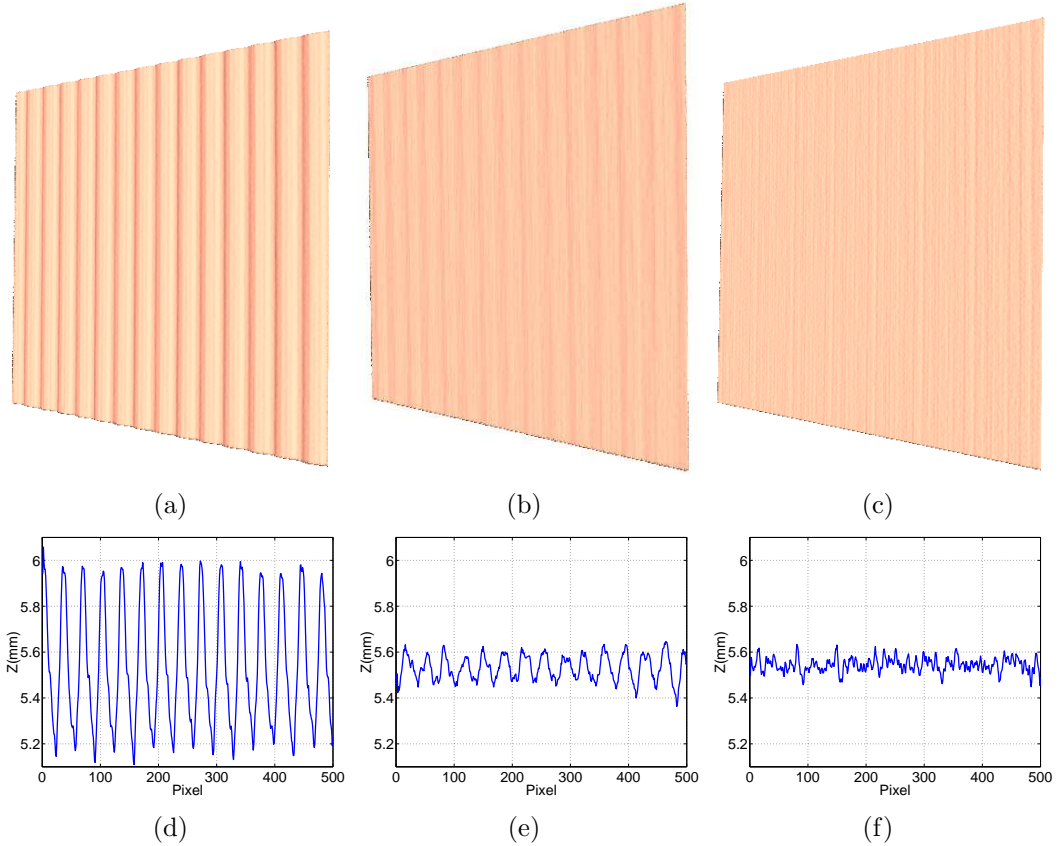


Figure 6.6: 3D results can be corrected by our algorithms. (a) 3D geometry without correction. (b) 3D geometry after correcting fringe images. (c) 3D geometry after correcting the phase. (d) 250th row cross section of the above image. (e) 250th row cross section of the above image. (f) 250th row cross section of the above image.

the error correction algorithms improved the accuracy of measurement and reduced stripe pattern error in the texture image.

6.5 Discussions

The error compensation method discussed in this chapter has the following advantages:

- *Simplicity.* The compensation algorithm introduced in this chapter is simple since the phase error as well as the non-sinusoidal error of the fringe images can be easily corrected using small LUTs.
- *Accuracy.* In theory, the phase error due to a nonlinear gamma curve can

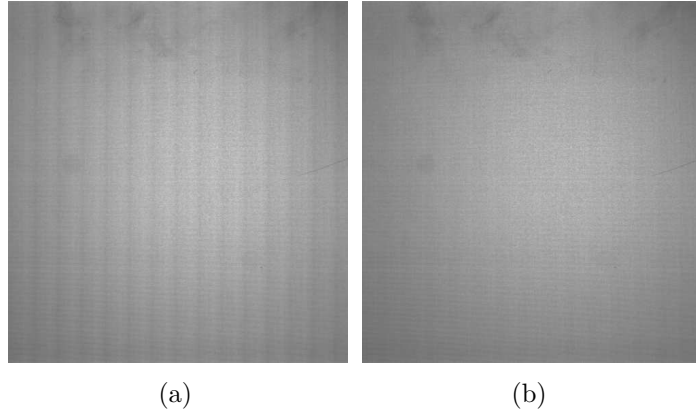


Figure 6.7: Texture image correction by using the proposed algorithm. (a) 2D texture before correction. (b) 2D texture after correction.

be completely eliminated as long as the projection response functions can be determined accurately by calibration.

- *Texture correction.* The method discussed in this chapter can correct the non-sinusoidality of the fringe images thus making high-quality texture mapping possible.

On the other hand, the algorithm is based on the following assumptions, which may limit the usage of the method.

- *Linear camera response.* This assumption is true for most of the camera. However, if the camera is nonlinear, it has to be calibrated.
- *Monotonic projection response.* This is true for most projectors.
- *No ambient light.* This assumption is for correcting nonsinusoidality of the fringe images for high-quality texture. If the ambient light is strong, the error will be larger. In most cases, comparing to the light from the projector, the ambient light is negligible.

6.6 Conclusions

This chapter introduced a novel error compensation method that can correctly wrap nonsinusoidal fringe images, the phase error due to nonsinusoidal waveforms

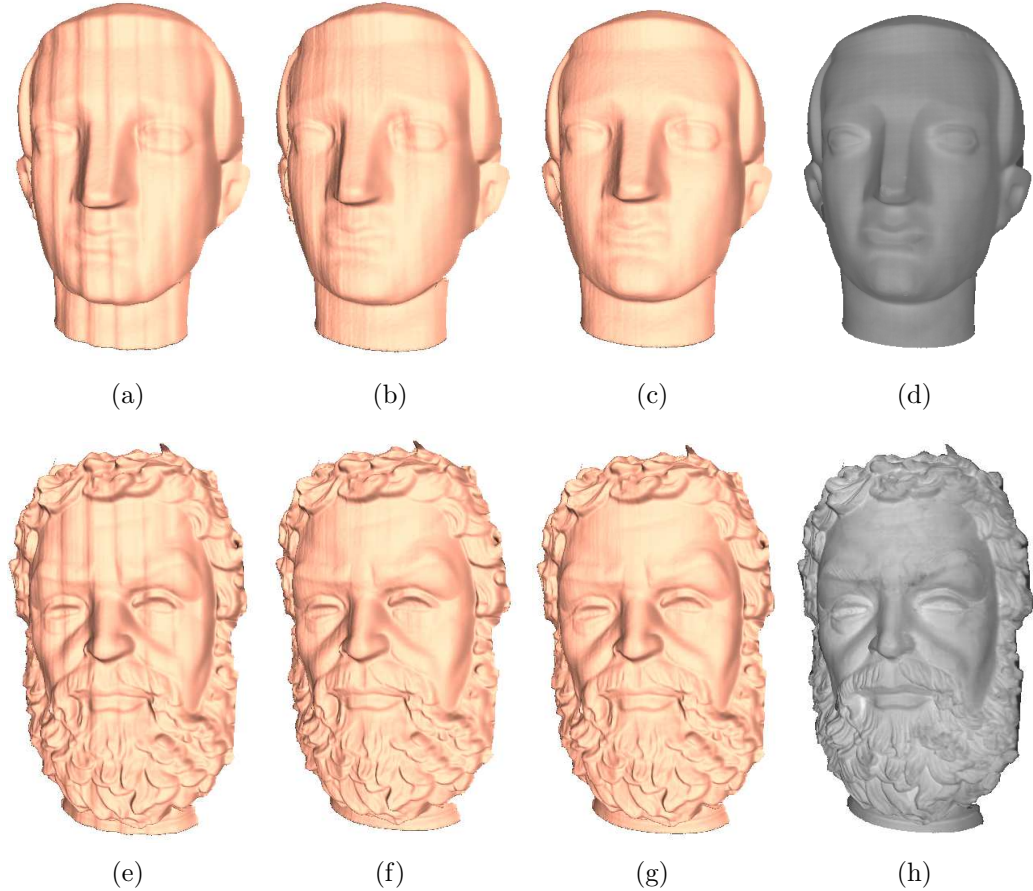


Figure 6.8: 3D measuring results of sculptures before and after error compensation. (a) 3D result without error compensation. (b) 3D result after fringe image correction. (c) 3D result after phase error correction. (d) 3D result with corrected texture mapping. (e) 3D result without error compensation. (f) 3D result after fringe image correction. (g) 3D result after phase error correction. (h) 3D result with corrected texture mapping.

can be eliminated completely in theory. Our experimental results demonstrated that by using the proposed method, the measurement error could be reduced by 10 times. In addition to error compensation, a similar method was also proposed to correct the non-sinusoidality of the fringe patterns for the purpose of generating a more accurate flat image of the object for texture mapping. Theoretical analysis, simulation results, and experimental findings were also presented.

Chapter 7

System Calibration

System calibration, which usually involves complicated and time-consuming procedures, is crucial for any 3D measurement system. In this chapter, a systematic method is proposed for accurate and quick calibration of the 3D shape measurement system we developed. In particular, a new method is developed that enables the projector to “capture” images like a camera, thus making the calibration of a projector the same as that of a camera, which is well established. This is a significant development because today projectors are increasingly used in various measurement systems yet so far no systematic way of calibrating them has been developed. This chapter describes the principle of the proposed method and presents some experimental results that demonstrate the performance of this new calibration method.

7.1 Introduction

Accurate measurement of the 3D shape of objects is a rapidly expanding field, with applications in entertainment, design, and manufacturing. Among the existing 3D measurement techniques, structured light based techniques are increasingly used due to their fast speed and non-contact nature. A structured light system differs from a classic stereo vision system in that it avoids the fundamentally difficult problem of stereo matching by replacing one camera with a projector. The key to accurate reconstruction of the 3D shape is the proper calibration of each element used in the structured light system [75]. Methods based on neural networks [76, 77], bundle adjustment [78, 79, 80, 81, 82, 83], or absolute phase [84] have been developed, in which

the calibration process varies depending on the available system parameters information and the system setup. It usually involves complicated and time-consuming procedures.

In this research, a novel approach is proposed for accurate and quick calibration of the structured light system we developed. In particular, a new method is developed that enables a projector to “capture” images like a camera, thus making the calibration of a projector the same as that of a camera, which is well established. This is a significant development because today projectors are increasingly used in various measurement systems yet so far no systematic way of calibrating them has been developed. In this new method, the projector and the camera can be calibrated independently, which avoids the problems related to the coupling of the errors of the camera and the projector. By treating the projector as a camera, we essentially unify the calibration procedures of a structure light system and a classic stereo vision system. For the system developed in this research, a linear model with a small error look-up-table(LUT) is found to be sufficient.

The rest of the chapter is organized as follows. Section 7.2 introduces the principle of the proposed calibration method. Section 7.3 shows some experimental results. Section 7.4 evaluates the calibration results. Section 7.5 discusses the advantages and disadvantages of this calibration method. Finally, Section 7.6 concludes the chapter.

7.2 Principle

7.2.1 Camera model

Camera calibration has been extensively studied over the years. A camera is often modeled by using a pinhole model, with intrinsic parameters, namely, the focal length, the principle point, the pixel skew effect and the pixel size and with extrinsic parameters, namely, the rotation and the translation from the world coordinate system to the camera coordinate system. Figure 7.1 shows a typical diagram of a pinhole camera model. p is an arbitrary point with coordinates (x^w, y^w, z^w) and (x^c, y^c, z^c) in the world coordinate system $\{o^w; x^w, y^w, z^w\}$ and camera coordinate

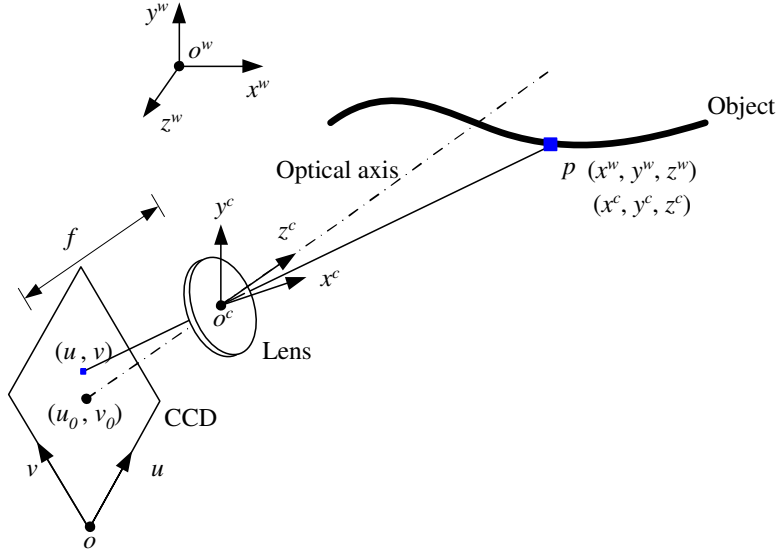


Figure 7.1: Pinhole camera model.

system $\{o^c; x^c, y^c, z^c\}$, respectively. The coordinate of its projection in the image plane $\{o; u, v\}$ is (u, v) . The relationship between a point on the object and its projection on the image sensor can be described as follows based on a projective model ,

$$sI = A[R, \ t]X^w, \quad (7.1)$$

where $I = \{u, v, 1\}^T$ is the homogeneous coordinate of the image point in the image coordinate system, $X^w = \{x^w, y^w, z^w, 1\}^T$ the homogeneous coordinate of the point in the world coordinate system, and s a scale factor. $[R, t]$, called the extrinsic parameters matrix, represents the rotation and translation between the world coordinate system and the camera coordinate system and has the following form:

$$R = \begin{bmatrix} r_{00}, & r_{01}, & r_{02} \\ r_{10}, & r_{11}, & r_{12} \\ r_{20}, & r_{21}, & r_{22} \end{bmatrix},$$

$$t = \{t_x, t_y, t_z\}^T,$$

A is the camera intrinsic parameters matrix and can be expressed as

$$A = \begin{bmatrix} \alpha, & \gamma, & u_0 \\ 0, & \beta, & v_0 \\ 0, & 0, & 1 \end{bmatrix}.$$

where (u_0, v_0) is the principle point, α and β are the focal lengthes along the u and v axes of the image plane, and γ is the parameter that describes the skewness of the two image axes.

If the surface of the standard planar calibration board is assumed to be $z^w = 0$ in the world coordinate system for each pose, then Equation 7.1 becomes,

$$s\{u, v, 1\}^T = A[r_1, r_2, r_3, t]\{x^w, y^w, 0, 1\}^T, \quad (7.2)$$

$$= A[r_1, r_2, t]\{x^w, y^w, 1\}^T, \quad (7.3)$$

$$= H\{x^w, y^w, 1\}^T, \quad (7.4)$$

where $H = A[r_1, r_2, t]$ is a 3×3 matrix defined up to scale, and r_1, r_2, r_3 are 3×1 column vectors of the rotation matrix. It is an 8 degrees of freedom problem. A target plane with at least 4 known points can be used to calculate all these parameters. In practice, more points are used to estimate the parameters by the singular-vector-decomposition (SVD) algorithm to reduce the noise effect.

7.2.1.1 Constraints on the intrinsic parameters

To separate the intrinsic parameters from matrix H , we need to find the constraints on these parameters. If we denote $H = [h_1, h_2, h_3]$, then

$$[h_1, h_2, h_3] = \lambda A[r_1, r_2, t],$$

where λ is an arbitrary scalar. We know that for rotation matrix R , r_1 and r_2 are orthonormal, we therefore have

$$h_1^T (AA^T)^{-1} h_2 = 0, \quad (7.5)$$

$$h_1^T (AA^T)^{-1} h_1 = h_2^T (AA^T)^{-1} h_2. \quad (7.6)$$

These are the two basic constraints for a given calibration plane pose. Because it has 8 degrees of freedom and there are 6 extrinsic parameters (3 for rotation and 3 for translation), we can only obtain 2 constraints. Combine these two constraints, matrix H can be separated into two matrices A and $[r_1, r_2, t]$. Therefore, the intrinsic parameters can be obtained if matrix H is known.

7.2.1.2 Lens distortion

A lens usually has distortion, especially the radial distortion. For most of the lenses, the distortion can be sufficiently described by considering the first two terms of the radial distortion. More elaborate models are discussed in references [85, 86, 87, 88]. In most cases, the distortion function is totally dominated by the radial components, especially the first term [85, 89, 90]. It has been noticed that more elaborate models not only may not help but also may cause numerical instability [89, 90].

Assume (u, v) to be the ideal pixel image coordinates and (\hat{u}, \hat{v}) the corresponding real measured image coordinates. The ideal points are the projection of the model points according to the pinhole model. Similarly, (x, y) and (\hat{x}, \hat{y}) are the ideal and real normalized image coordinates. We have,

$$\hat{x} = x + x[k_1(x^2 + y^2) + k_2(x^2 + y^2)^2], \quad (7.7)$$

$$\hat{y} = y + y[k_1(x^2 + y^2) + k_2(x^2 + y^2)^2], \quad (7.8)$$

where k_1 and k_2 are the coefficients of the radial distortion. The center of the radial distortion is the same as the principal point. From $\hat{u} = u_0 + \alpha\hat{x} + \gamma\hat{y}$ and $\hat{v} = v_0 + \beta\hat{y}$, we have,

$$\hat{u} = u + (u - u_0)[k_1(x^2 + y^2) + k_2(x^2 + y^2)^2], \quad (7.9)$$

$$\hat{v} = v + (v - v_0)[k_1(x^2 + y^2) + k_2(x^2 + y^2)^2]. \quad (7.10)$$

7.2.2 Camera calibration

To obtain the intrinsic parameters of the camera, a flat checkerboard is used, as shown in Figure 7.2. In this research, we used a checkerboard with 15×15

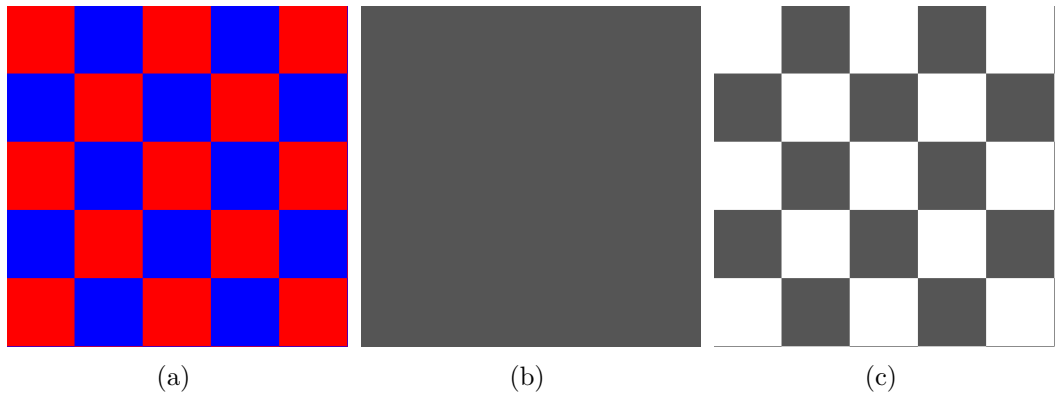


Figure 7.2: Checkerboard for calibration. (a) Red/blue checkerboard. (b) White light illumination, B/W camera image. (c) Red light illumination, B/W camera image.

mm squares. Instead of standard black-white checkerboard, we used a red/blue checkerboard, which will be explained in Section 7.2.3. The calibration procedures follow Zhang’s method [91]. The flat checkerboard positioned with different poses are imaged by the camera. A series of images (10) as shown in Figure 7.3 are used to obtain the intrinsic parameters of the camera using the Matlab tool box provided by Bouguet [92]. The intrinsic parameters matrix based on the linear model is,

$$A^c = \begin{bmatrix} 25.8031, & 0, & 2.7962 \\ 0, & 25.7786, & 2.4586 \\ 0, & 0, & 1 \end{bmatrix}.$$

for the Dalsa CA-D6-0512 camera with Fujinon HF25HA-1B lens. The size of each CCD pixel is $10 \times 10 \mu\text{m}$ square. We found that the principle point deviated from the CCD center, which might be caused by misalignment during the camera assembling process.

7.2.3 Projector calibration

A projector can be regarded as the inverse of a camera because it projects images instead of capturing them. In this research, we propose a method that enables a projector to “capture” images like a camera, thus making the calibration of a projector essentially the same as that of a camera, which is well established.

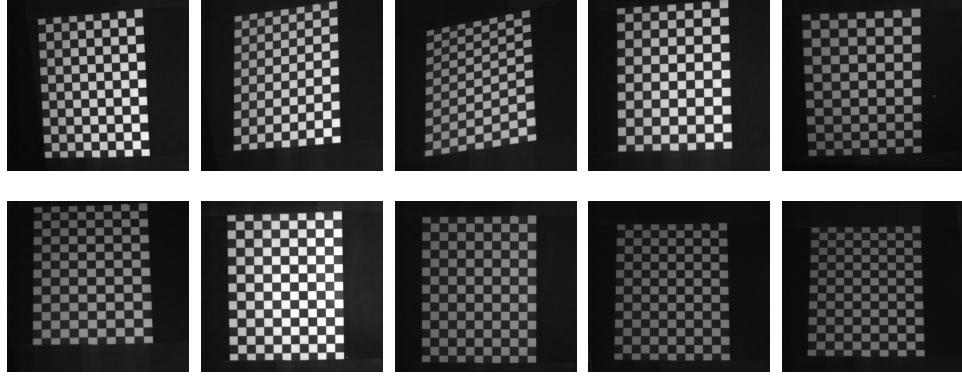


Figure 7.3: Camera calibration images.

7.2.3.1 DMD image generation

In order to “capture” images using a projector, an absolute phase measurement technique has to be employed. As shown in Figure 7.4. In addition to three phase-shifted fringe images, an additional centerline image, a bright line on the center of the DMD chip, is captured. The phase value on this centerline is assumed to be 0, which is used as the reference to convert a relative phase map to an absolute phase map. If we assume the average phase computed from the fringe images at the position of the centerline to be,

$$\bar{\Phi}_0 = \frac{\sum_{n=0}^N \phi_n(i, j)}{N}, \quad (7.11)$$

then the relative phase can be converted to absolute phase as follows,

$$\phi_a(i, j) = \phi(i, j) - \bar{\Phi}_0. \quad (7.12)$$

After the absolute phase is obtained, a unique one-to-one map between a CCD image and a DMD image in the phase domain can be established.

Figure 7.4 shows how the correspondence between the CCD image and the DMD image is established. The red point in the fringe images is an arbitrary point whose absolute phase can be determined using Equations 7.11 and 7.12. This phase value corresponds to one straight line on the DMD image, which is the horizontal red line in Figure 7.4(e). Therefore, this is a one-to-many map. If similar steps are applied to the fringe images with vertical fringes, another one-to-many map can be established. The same point on the CCD images is mapped to a vertical line on the

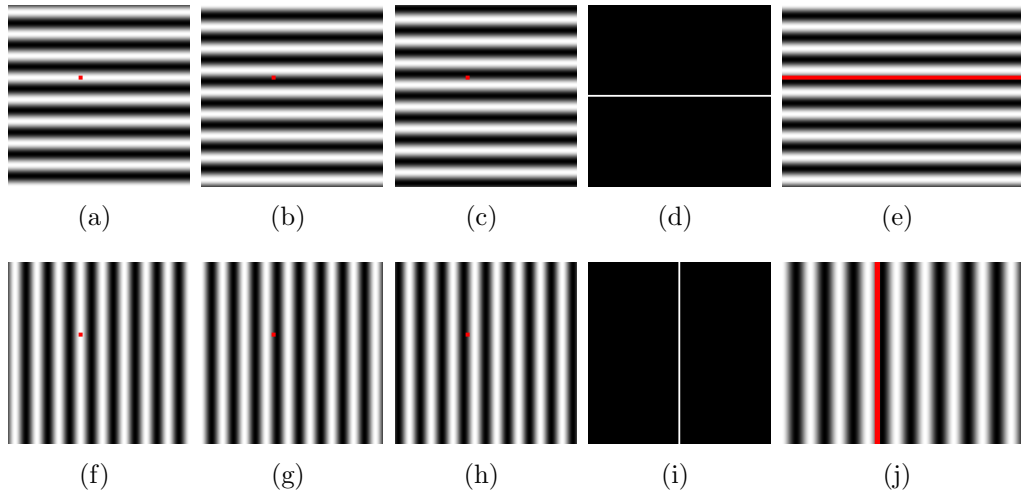


Figure 7.4: Correspondence between the CCD image and the DMD image. (a)–(c) CCD horizontal fringe images I_1 , I_2 , and I_3 , respectively. (d) CCD horizontal centerline image. (e) DMD horizontal fringe image. (f)–(h) CCD vertical fringe images I_1 , I_2 , and I_3 , respectively. (i) CCD vertical centerline image. (j) DMD vertical fringe image.

DMD image. The intersection point of the horizontal line and the vertical line is the corresponding point on the DMD of the arbitrary point on the CCD. Therefore, by using this method, we can establish a one-to-one map between a CCD image and a DMD image. In other words, the CCD image can be transferred to the DMD pixel-by-pixel to form an image, which is regarded as the image “captured” by the projector.

For well-established camera calibration, a standard B/W checkerboard is usually used. However, in this research, a B/W checkerboard cannot be used since the fringe image captured by the camera does not have enough contrast in the dark region. To avoid this problem, a red/blue checkerboard illustrated in Figure 7.2(a) is utilized. This is because the response of the B/W camera to red and blue colors are similar. If the checkerboard is illuminated by white light, the B/W camera can only see a uniform board (in the ideal case) as illustrated in Figure 7.2(b). When the checkerboard is illuminated by red or blue light, the B/W camera will see a regular checkerboard. Figure 7.2(c) shows the image of the checkerboard with red light illuminated, which can be mapped onto the DMD sensor to form the DMD image.

In summary, the projector captures the checkerboard images through the following steps,

- (1) Capture three B/W phase-shifted horizontal fringe images projected by the projector with B/W light illumination.
- (2) Capture the horizontal centerline image projected by the projector with B/W light illumination.
- (3) Capture three B/W phase-shifted vertical fringe images projected by the projector with B/W light illumination.
- (4) Capture the vertical centerline image projected by the projector with B/W light illumination.
- (5) Capture the image of the checkerboard with red light illumination.
- (6) Determine the one-to-one pixel-wise mapping between the CCD and the DMD.
- (7) Map the texture of the checkerboard with red light illumination to the DMD to create the corresponding DMD image.

Figure 7.5 shows an example of converting a CCD checkerboard image to its corresponding DMD image. Figure 7.5(a) shows the checkerboard image captured by the camera with red light illumination while Figure 7.5(b) shows the corresponding DMD image. One can verify the accuracy of the DMD image by projecting it onto the real checkerboard to check the alignment. If the alignment is good, it means that the DMD image created is accurate.

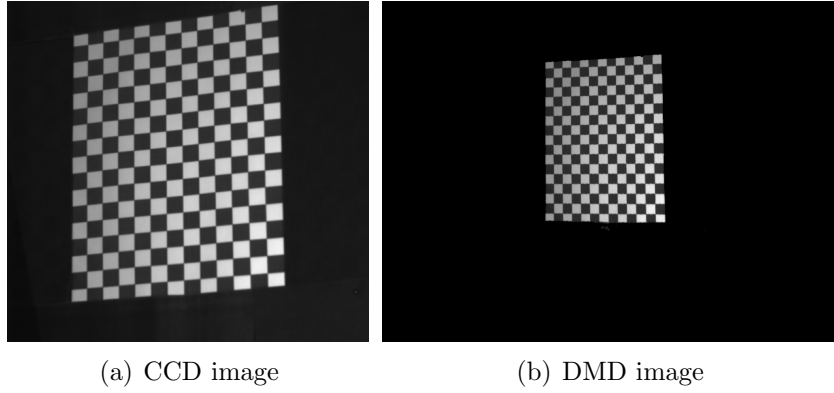


Figure 7.5: CCD image and its corresponding DMD image.

7.2.3.2 Projector calibration

After a set of DMD images are generated, the calibration of intrinsic parameters of a projector can follow that of a camera. The following matrix

$$A^p = \begin{bmatrix} 31.1384, & 0, & 6.7586 \\ 0, & 31.1918, & -0.1806 \\ 0, & 0, & 1 \end{bmatrix}.$$

is the intrinsic parameter matrix obtained for the projector PLUS U2-1200. The DMD micro-mirror size is $13.6 \times 13.6\mu m$ square. We notice that the principle point deviates from the nominal center significantly in one direction, even outside the DMD chip. This is due to the fact that the projector projects images along an off-axis direction.

7.2.4 System calibration

After the intrinsic parameters of the projector and the camera are calibrated. The next task is to calibrate the extrinsic parameters of the system. For this purpose, a unique world coordinate system for the projector and camera has to be established. In this research, a world coordinate system is established based on one calibration image set. The xy axes on the plane, while the z axis is perpendicular to the plane and points to the imaging devices (camera and projector).

Figure 7.6 shows a checker square on the checkerboard and its corresponding

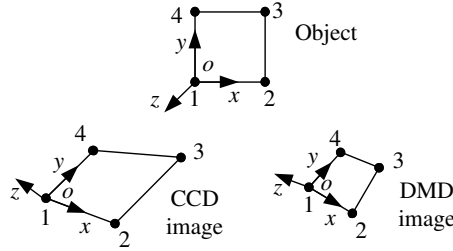


Figure 7.6: World coordinate system.

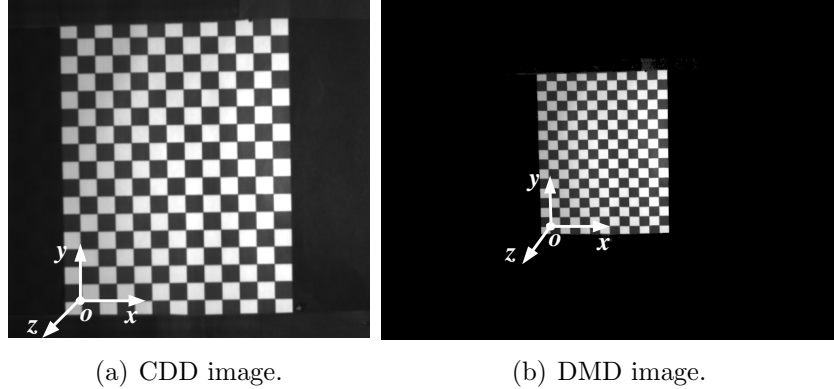


Figure 7.7: World coordinate system construction.

CCD image and DMD image. The four corners 1, 2, 3, 4 of this square are imaged onto the CCD and DMD respectively. We choose corner 1 as the origin of the world coordinate system, from 1 to 2 as the x positive direction, and 1 to 4 as the y positive direction. The z axis is defined based on the right-hand rule in Euclidean space. In this way, we can define the same world coordinate system based on the CCD and DMD images. Figure 7.7 illustrates the origin and the directions of the x, y axes on these images.

The purpose of the system calibration is to find the relationships between the camera coordinate system and the world coordinate system and also the projector coordinate system and the same world coordinate system. These relationships can be expressed as,

$$X^c = M^c X^w,$$

$$X^p = M^p X^w.$$

where $M^c = [R^c, t^c]$, is the transformation matrix between the camera coordinate

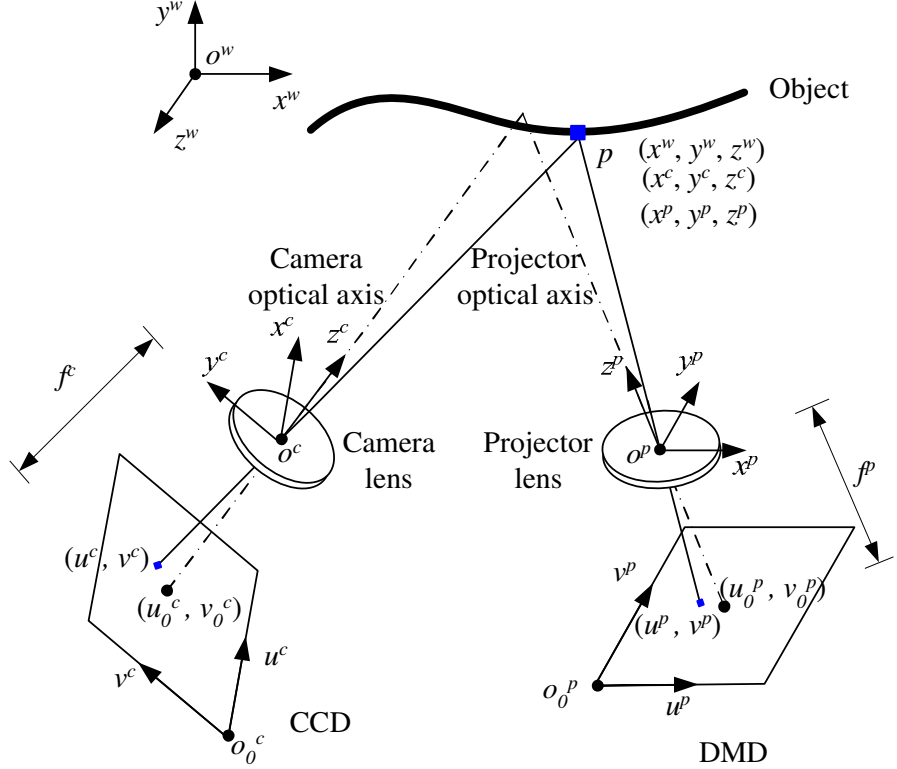


Figure 7.8: Structured light system configuration.

system and the world coordinate system and $M^p = [R^p, t^p]$, is the transformation matrix between the projector coordinate system and the world coordinate system, and $X^c = \{x^c, y^c, z^c\}^T$, $X^p = \{x^p, y^p, z^p\}^T$, and $X^w = \{x^w, y^w, z^w, 1\}^T$ are the coordinate matrices for the point p (see Figure 7.8) in the camera, projector, and the world coordinate systems, respectively. X^c and X^p can be further transformed to the CCD and DMD image coordinates (u^c, v^c) and (u^p, v^p) by applying the intrinsic matrices A^c and A^p because the intrinsic parameters are already calibrated. That is

$$s^c \{u^c, v^c, 1\}^T = A^c X^c,$$

$$s^p \{u^p, v^p, 1\}^T = A^p X^p.$$

The extrinsic parameters can be obtained by the same procedures as those for the intrinsic parameters estimation. The only difference is that only one calibration image is needed to obtain the extrinsic parameters. The same Matlab toolbox provided by Bouguet [92] was utilized to obtain the extrinsic parameters. Example extrinsic

parameter matrices for the system setup are

$$M^c = \begin{bmatrix} 0.016364, & 0.999735, & -0.016162, & -103.435483 \\ 0.999345, & -0.015831, & 0.032549, & -108.195130 \\ 0.032285, & -0.016684, & -0.999339, & 1493.079405 \end{bmatrix},$$

$$M^p = \begin{bmatrix} 0.019757, & 0.999619, & -0.019294, & -82.087351 \\ 0.991605, & -0.017125, & 0.128161, & 131.561677 \\ 0.127782, & -0.021664, & -0.991566, & 1514.164208 \end{bmatrix}.$$

7.2.5 Phase-to-coordinate conversion

Real measured object coordinates can be obtained based on the calibrated intrinsic and extrinsic parameters of the projector and the camera. Three phase-shifted fringe images and a centerline image are used to reconstruct the geometry of the surface. In the following, we discuss how to solve for the coordinates based on these four images.

For each arbitrary point (u^c, v^c) on the CCD image plane, its absolute phase can be calculated, which corresponds to a line in the DMD image with the same absolute phase value. Without loss of generality, the line is assumed to be a vertical line with $u^p = \zeta(\phi_a(u^c, v^c))$. Assuming the world coordinates of the point to be (x^w, y^w, z^w) , we have the following equation that transform the world coordinates to the camera image coordinates:

$$s \{ u^c \ v^c \ 1 \ }^T = P^c \{ x^w \ y^w \ z^w \ 1 \ }^T, \quad (7.13)$$

where P^c is the calibrated matrix for the camera,

$$P^c = A^c M^c = \begin{bmatrix} \alpha^c, & \gamma^c, & u_0^c \\ 0, & \beta^p, & v_0^c \\ 0, & 0, & 1 \end{bmatrix} \begin{bmatrix} r_{00}^c & r_{01}^c & r_{02}^c & t_0^c \\ r_{10}^c & r_{11}^c & r_{12}^c & t_1^c \\ r_{20}^c & r_{21}^c & r_{22}^c & t_2^c \end{bmatrix}.$$

Similarly, we have the coordinate transformation equation for the projector,

$$s \{ u^p \ v^p \ 1 \ }^T = P^p \{ x^w \ y^w \ z^w \ 1 \ }^T, \quad (7.14)$$

where P^p is the calibrated matrix for the projector,

$$P^p = A^p M^p = \begin{bmatrix} \alpha^p, & \gamma^p, & u_0^p \\ 0, & \beta^p, & v_0^p \\ 0, & 0, & 1 \end{bmatrix} \begin{bmatrix} r_{00}^p & r_{01}^p & r_{02}^p & t_0^p \\ r_{10}^p & r_{11}^p & r_{12}^p & t_1^p \\ r_{20}^p & r_{21}^p & r_{22}^p & t_2^p \end{bmatrix}.$$

From Equations 7.13 and 7.14, we can obtain three linear equations,

$$f_1(x^w, y^w, z^w, u^c) = 0, \quad (7.15)$$

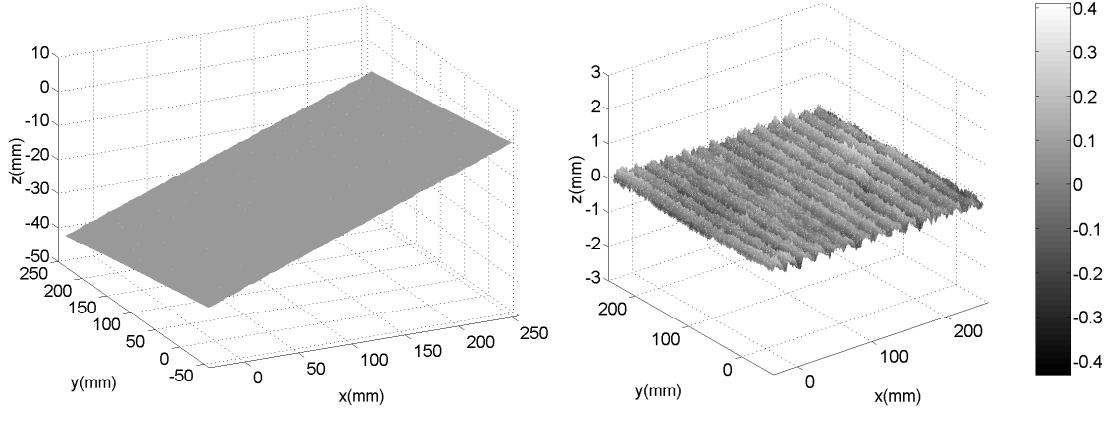
$$f_2(x^w, y^w, z^w, v^c) = 0, \quad (7.16)$$

$$f_3(x^w, y^w, z^w, u^p) = 0. \quad (7.17)$$

where u^c , v^c , and u^p are known. Therefore the world coordinates (x^w, y^w, z^w) of the point p can be uniquely solved for the image point (u^c, v^c) (see Appendix A for details).

7.3 Experiments

To verify the calibration procedures introduced in this chapter, we measured a planar board with a white surface. The measurement result is shown in Figure 7.9(a). We then fit the measured coordinates with an ideal flat plane and find the distances between the measured points and the ideal plane, which are regarded as the measurement error, as illustrated in Figure 7.10. Our experiments show that the error map has similar patterns for all measured positions and orientations. To compensate for this type of systematic error, we create an error map LUT based on one position and then subtract this error map from all the other measurements. As a result, the measurement accuracy is significantly increased (see details in Section 7.5). Figure 7.10(a) shows the error map before compensation, which is approximately RMS 0.41 mm. After this error compensation, the error is reduced to RMS 0.10 mm as illustrated in Figure 7.10(b). The remaining error is caused mostly by the residual non-sinusoidal fringe images. In addition, we measured a sculpture Zeus and the result is shown in Figure 7.11. The first image is the object with texture mapping, the second image is the 3D model of the sculpture in shaded mode, and the last one



(a) 3D plot of the measured result. (b) Measurement error.

Figure 7.9: 3D measurement result of a planar surface.

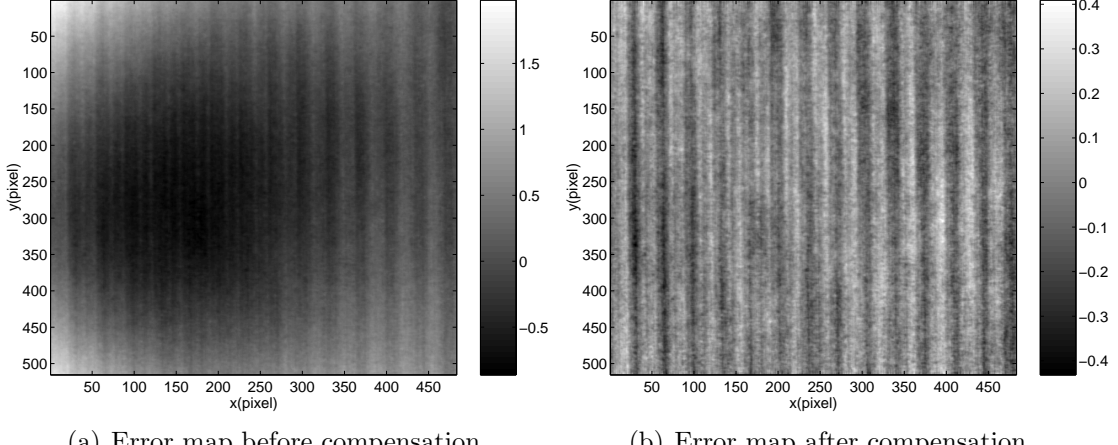
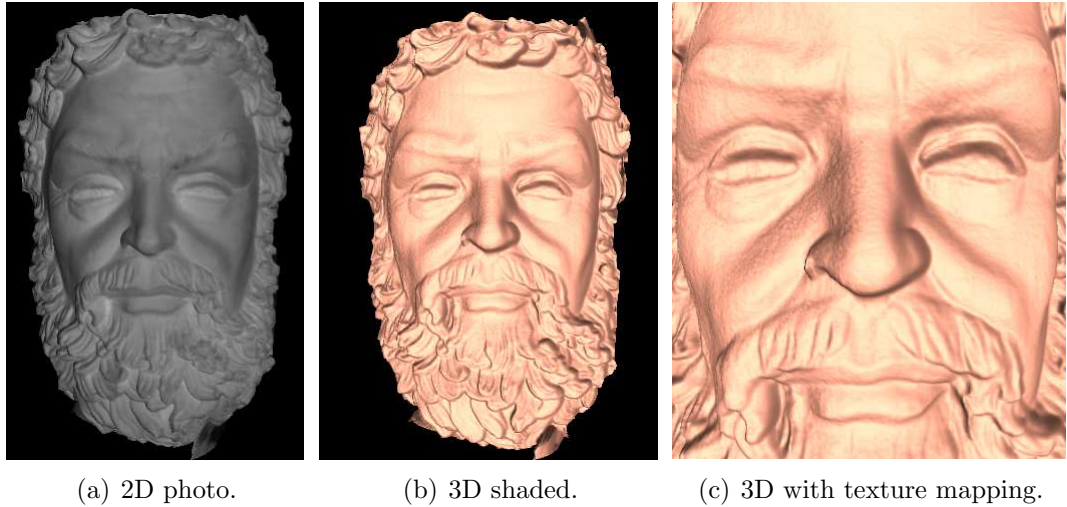


Figure 7.10: Measurement error after calibration.

is the zoom-in view of the 3D model. The reconstructed 3D model is very smooth with details.

7.4 Calibration Evaluation

For more rigorous evaluation of this calibration procedure, we measured a planar white board at 12 different positions and orientations as shown in Figure 7.12. The whole volume is approximately $342 \times 376 \times 658$ mm. The normals, x, y, z ranges, and the corresponding errors of the plane for each pose are listed in Table 7.1. We found that the error of the calibration method did not depend on the



(a) 2D photo.

(b) 3D shaded.

(c) 3D with texture mapping.

Figure 7.11: 3D Measurement result of sculpture Zeus.

orientation of the measured plane unless the plane is positioned far away from the system. Figure 7.13(a) illustrates the relationship between the error and the location of the testing plane. It is obvious that the error is affected by the position of the testing plane, though it is affected when the plane is put far behind. Figures 7.13(c)-7.13(b) show the measured error correlated to the rotation angle between x , y , and z axes, respectively. No clear correlation between the orientation of the testing plane and the measured error can be observed. Our experiments also show that the remaining error is mostly caused by the residual non-sinusoidal fringes. Therefore, these results demonstrate that the calibration is robust and accurate over a large volume.

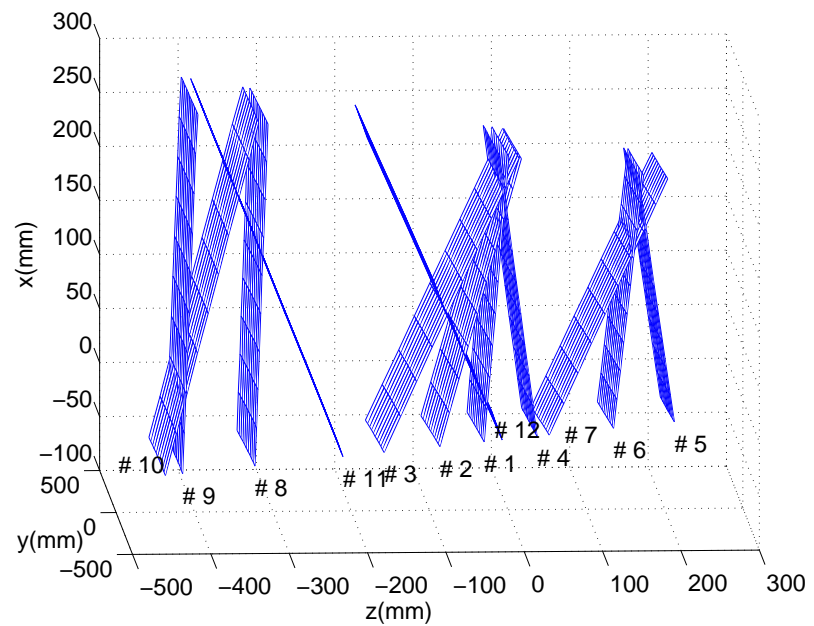


Figure 7.12: Positions and orientations of the planar board for the evaluation of the calibration results.

Table 7.1: Measurement data of the testing plane at different positions and orientations

Plane	Normal (mm)	x range (mm)	y range (mm)	z range (mm)	RMS error (mm)	RMS* error (mm)
# 1	(-0.1189, 0.0334, 0.9923)	[-32.55, 236.50]	[-58.60, 238.81]	[-43.47, -1.47]	0.10	0.48
# 2	(-0.3660, 0.0399, 0.9297)	[-36.05, 234.77]	[-64.24, 243.10]	[-102.24, 14.61]	0.10	0.33
# 3	(-0.5399, 0.0351, 0.8410)	[-40.46, 234.93]	[-72.86, 248.25]	[-172.84, 11.61]	0.13	0.22
# 4	(0.1835, 0.0243, 0.9827)	[-60.11, 233.74]	[-60.11, 233.74]	[-22.37, 33.31]	0.10	0.64
# 5	(0.1981, 0.0259, 0.9798)	[-17.52, 217.04]	[-38.04, 221.09]	[156.22, 209.44]	0.11	0.61
# 6	(-0.1621, 0.0378, 0.9860)	[-22.33, 216.39]	[-37.42, 226.71]	[122.37, 171.38]	0.11	0.46
# 7	(-0.5429, 0.0423, 0.8387)	[-27.41, 212.85]	[-47.36, 232.86]	[38.06, 202.34]	0.10	0.17
# 8	(-0.0508, 0.0244, 0.9984)	[-50.66, 272.30]	[-96.88, 260.18]	[-336.22, -310.53]	0.22	0.55
# 9	(-0.0555, 0.0149, 0.9983)	[-56.38, 282.45]	[-108.03, 266.72]	[-425.85, -400.54]	0.22	0.57
# 10	(-0.3442, 0.0202, 0.9387)	[-57.74, 273.35]	[-106.63, 268.37]	[-448.48, -322.44]	0.22	0.44
# 11	(0.4855, -0.0000, 0.8742)	[-43.70, 281.07]	[-106.88, 260.01]	[-394.84, -214.85]	0.20	0.67
# 12	(0.5217, -0.0037, 0.8531)	[-31.12, 256.75]	[-81.14, 245.23]	[-185.51, -10.41]	0.16	0.66

Note: RMS is the standard deviation of the measured plane using our calibration method

RMS* is the standard deviation of the measured plane using the approximate calibration method introduced in Chapter 3.

As a comparison, we compute planar error when the approximate calibration method introduced in Chapter 3 is employed. Figure 7.14(a) shows the correlation between the error and the position of the plane. Since the surface normal direction changes, it may still cause large error. Figures 7.14(c)-7.14(b) show the correlation between the error and the rotation angle of the plane about x , y , and z axes, respectively. It is obvious that the error is not sensitive to the position but is highly sensitive to the rotation about of the plane around y axis. This is not desirable for a real object, the geometry may be complex and the surface normal may vary dramatically from point to point. However, since the approximate calibration method does not require the additional centerline image, it is suitable for our real-time acquisition, reconstruction, and display system. Even though, the error is larger (RMS 0.6 mm), it is still acceptable for a real-time system.

To further verify that our calibration method is not significantly affected by the surface normal direction while the traditional method is, we measured a cylindrical surface with a diameter of 200 mm. Figure 7.15 shows the measurement results. In comparison with the measurement result obtained using the traditional approximate calibration method, the error is significantly smaller. This is because the surface normal of a cylindrical surface changes continuously across the surface and the traditional approximate calibration method is highly sensitive to this change.

7.5 Discussion

The calibration method introduced in this research for the structured light systems has the following advantages over other methods:

- *Simple* The proposed calibration method separates the projector and camera calibration, which makes the calibration simple.
- *Simultaneous* For each checkerboard calibration pose, the camera image and the projector image can be obtained simultaneously. Therefore, the camera and the projector can be calibrated simultaneously.
- *Fast* The calibration of the projector and the camera follows the same pro-

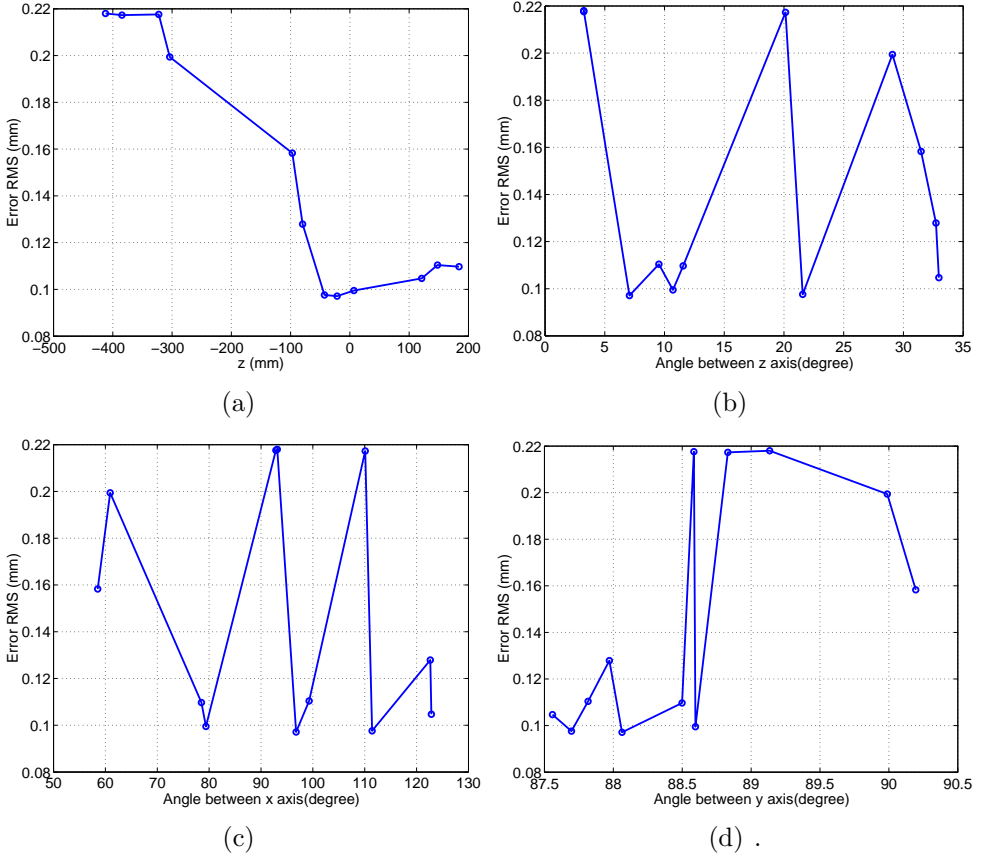


Figure 7.13: Planar error correlated to the poses of the measured plane using our calibration method. (a) Planar error vs plane position. (b) Planar error plane rotation angel around x axis. (c) Planar error vs plane rotation angel around y axis. (d) Planar error vs plane rotation angel around z axis.

cedures of camera calibration. A standard checkerboard can be utilized to calibrate the camera and the projector simultaneously. This is much faster than other structured light calibration methods in which complex optimization procedures have to be involved to obtain the relationship between the camera and projector parameters.

- *Accurate* Since the projector and camera calibrations are independent, there is no coupling issue involved and thus more accurate parameters of the camera and projector can be obtained.

For the system we developed, we did not use the nonlinear model for the camera or the projector. Our experiments showed that the nonlinear model generates worse

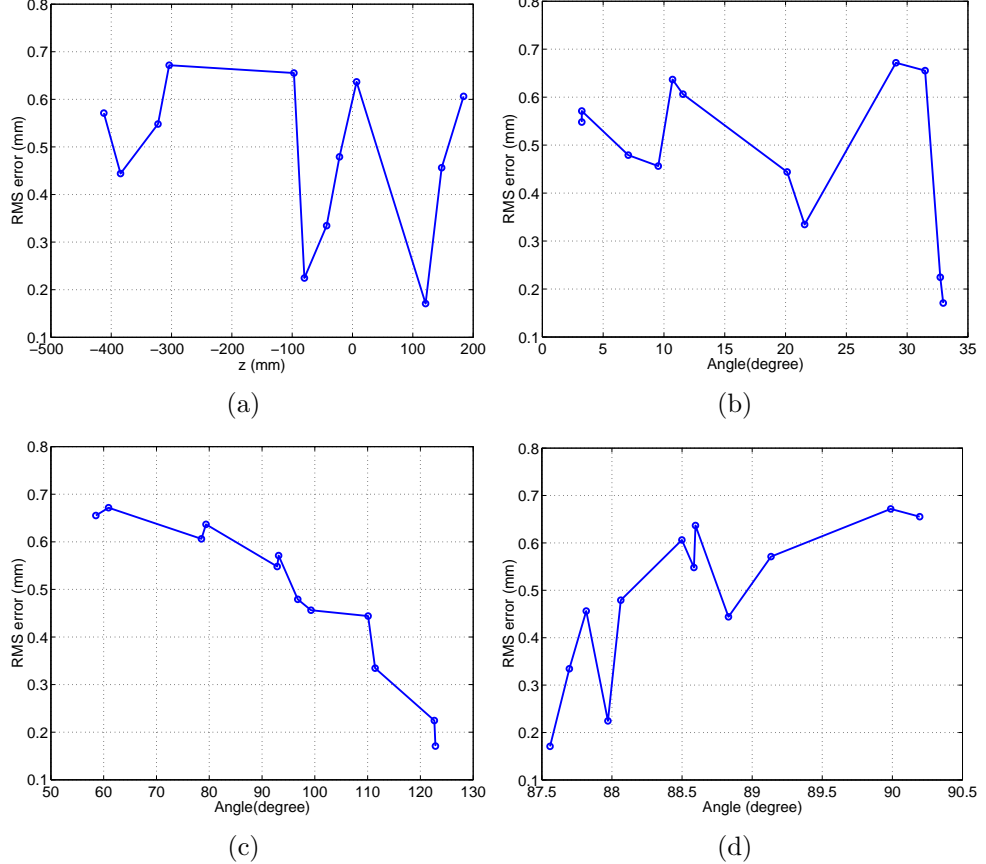


Figure 7.14: Planar error correlated to the poses of the measured plane using traditional approximate calibration method. (a) Planar error vs plane position. (b) Planar error plane rotation angel around x axis. (c) Planar error vs plane rotation angle around y axis. (d) Planar error vs plane rotation angel around z axis.

results since the nonlinear distortion of the lenses of our system was small. Use of the nonlinear model may have caused numerical instability. To verify that the nonlinear distortions of the camera and the projector are negligible, we compute the errors of the corner points of the checkerboard on the image planes of the camera and projector assuming a linear model. Here the error is defines as the difference between the coordinates of a checker corner point as computed from the real captured image and from the back projected image based on a linear model. Figure 7.16 shows the error for the calibration plane, whose variations are within one pixel. Therefore the linear model is sufficient to describe the camera and the projector of our system.

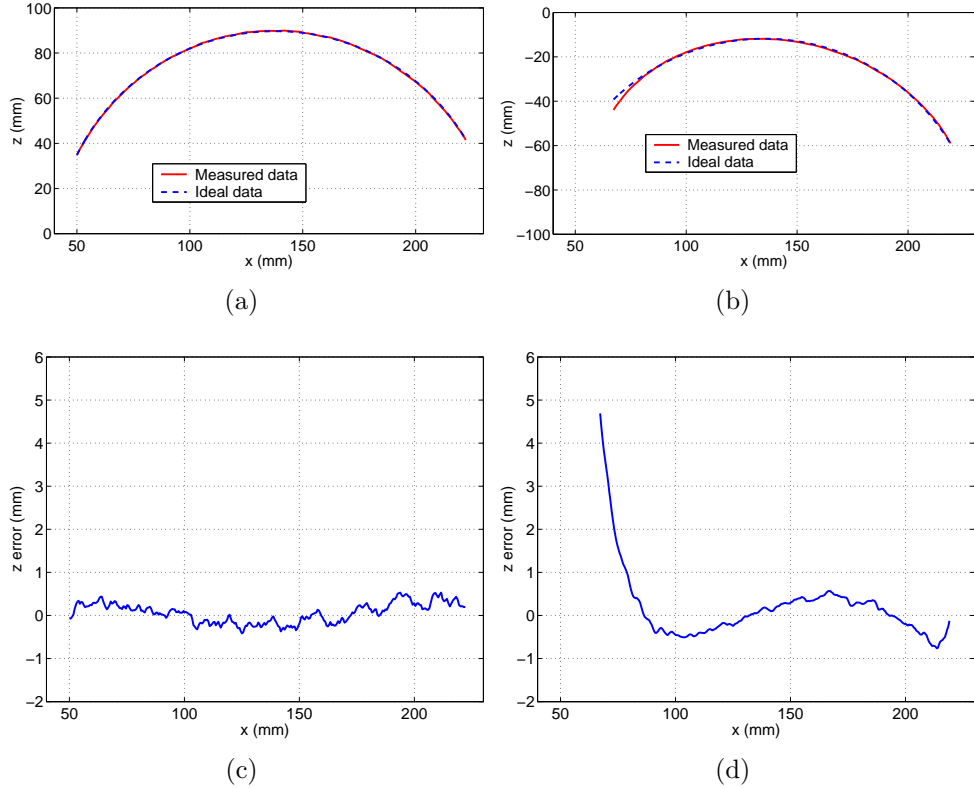
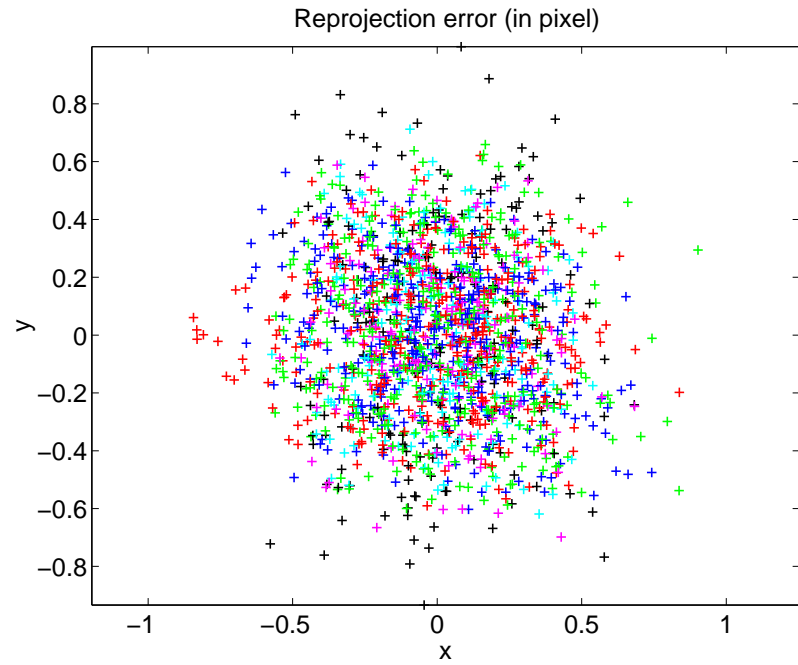


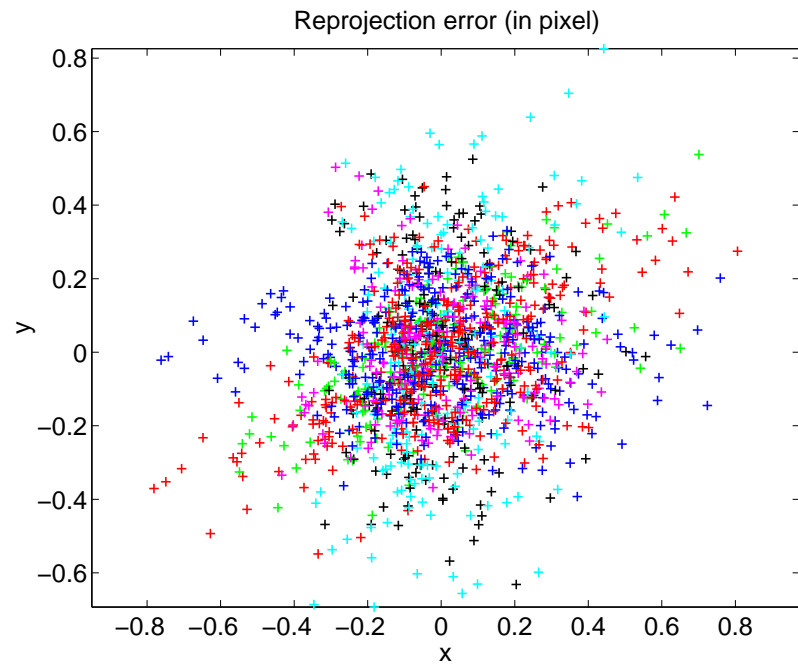
Figure 7.15: Measurement result of a cylinder. (a) Cross section of the measured shape using our calibration method. (b) Cross section of the measured shape using the approximate calibration method. (c) Shape error for our calibration. (d) Shape error for the traditional approximate calibration method.

7.6 Conclusions

This chapter introduced a novel structured light calibration method that calibrates the projector and the camera independently and accurately. The measurement error is demonstrated to be RMS 0.22 mm over a volume of $342 \times 376 \times 658$ mm. We proposed a method that enabled a projector “capture” images, thus turning the projector into a bi-directional device which might have potential other applications in computer graphics, medical imaging, plastic surgery, etc. The calibration is fast, robust and accurate. It, significantly simplifies the structured light system calibration and re-calibration procedures.



(a) Error for the projector.



(b) Error for the camera.

Figure 7.16: Error caused by nonlinear image distortions.

Chapter 8

Conclusions and Future Works

This chapter summarizes the accomplishments and proposes the future works of this dissertation research.

8.1 Conclusions

In this dissertation research, we made the following major contributions:

- (1) **Developed an advanced high-resolution, real-time 3D shape measurement system**

Two high-resolution, real-time 3D shape measurement systems have been successfully developed in this research. Both systems generate a data cloud of 532×500 points per frame. The first system has a speed of 40 frames per second for 3D data acquisition, 40 frames per second for B/W texture image acquisition, and 26.7 frames per second for color texture image acquisition. The second system has a lower speed of 30 frames per second for both 3D data and B/W texture image acquisition. Color texture mapping is not possible for the second system due to hardware limitation. However, the second system is much more stable and produces better results with smaller errors, as compared to the first system. By further implementing the fast 3D reconstruction algorithms and parallel processing technique into the real-time 3D data acquisition system, we developed a system that can simultaneously acquire, reconstruct and display 3D information of the measured object at a

frame rate of up to 40 frames per second and at a image resolution of 532×500 points per frame. Experiments demonstrated that the real-time system provided satisfactory measurement results for slow moving objects such as human facial expressions.

(2) Developed a novel trapezoidal phase-shifting method

A novel coding algorithm, trapezoidal phase-shifting algorithm was developed in this research. It has the advantage of high computation speed, which is at least 4.5 times faster when compared to the traditional sinusoidal phase-shifting method. If compared with the intensity ratio based methods, this algorithm is significantly less sensitive to image defocus, thus permitting a larger dynamic range measurement. This coding algorithm made real-time 3D reconstruction possible at an image resolution of 532×500 pixels with an ordinary PC (Pentium 4, 2.8 GHz).

(3) Developed a novel fast phase-wrapping algorithm

Though the trapezoidal phase-shifting algorithm is much less sensitive to image defocus as compared to the intensity ratio based methods, it is still affected by the defocusing effect. In the extreme case, when the trapezoidal fringe pattern is defocused so much that it becomes sinusoidal, we found that the error was still at a relatively small value of 0.6%. Based on this finding, we introduced a fast phase-wrapping algorithm which employs the trapezoidal phase-shifting algorithm to process sinusoidal patterns and a LUT method to compensate for the error. The reconstructed geometry has similar quality as that of the traditional phase-wrapping algorithm. This new algorithm combines the speed advantage of the trapezoidal phase-shifting algorithm and the accuracy advantage of the sinusoidal phase-shifting algorithm. By implementing this new algorithm, 3D reconstruction can be accomplished in real time with high accuracy.

(4) Developed a novel error compensation method

In the phase-shifting method we used, the distortion of the supposedly sinusoidal fringe patterns due to projector nonlinearity is the major error source. In this research, a novel method was developed that could theoretically completely eliminate the error caused by the non-sinusoidal waveforms. This method uses a small LUT to compensate for the error and was shown to be able to reduce the error by 10 times. In addition, a method was developed to correct the non-sinusoidality of the fringe patterns, which makes high-quality texture mapping possible. Texture mapping important for applications in computer vision and computer graphics.

(5) Developed a novel calibration method

A novel method was developed for accurate and quick system calibration. In particular, a new method was developed that enabled a projector to “capture” images like a camera, thus making the calibration of a projector the same as that of a camera. This is a significant development because today projectors are increasingly used in various measurement systems yet so far no systematic way of calibrating them has been developed. With the proposed method, the total calibration process only took approximately 30 minutes. Our experimental results demonstrated that the measurement accuracy of our system was less than RMS 0.22 mm over a volume of $342 \times 376 \times 658$ mm.

8.2 Future Works

In this research, we successfully developed two prototype real-time 3D shape measurement systems. However, there are still many research issues to be studied and applications to be explored.

(1) Eliminate errors caused by tangent illumination

When the projection light is tangent to an object’s surface, the spatial fringe period becomes infinite, which causes phase distortion and therefore measurement error. Figure 8.1 shows a typical case when large errors occur near

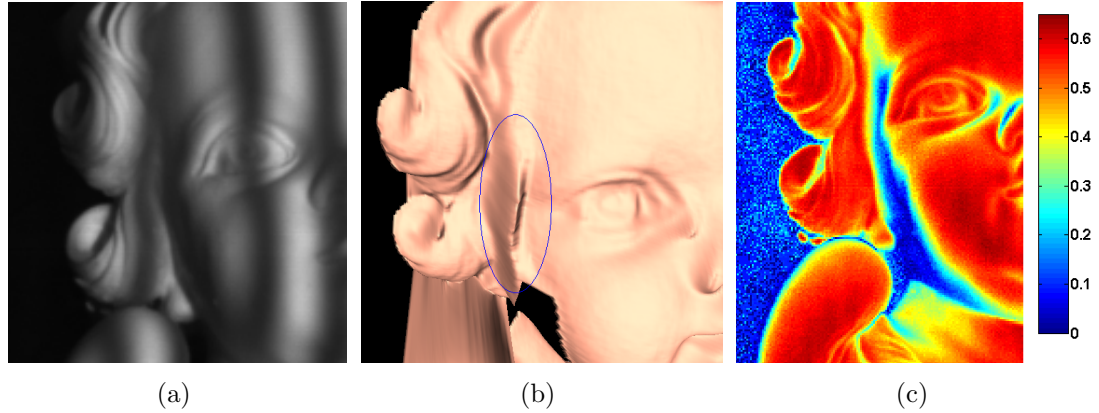


Figure 8.1: Tangent projection effect and possible solution. (a)Fringe image. (b)3D reconstructed result. (c) Gamma map.

a tangent region. One possible way of detecting this tangent region is to calculate data modulation γ . Tangent regions are usually located at the start of the shadow areas of the projector. γ value is usually close to 0 in the shadow areas of the projector, but close to 1 in well illuminated regions with reasonable surface reflectivity. Figure 8.1(c) shows the γ map of the measured object. If we use the γ map to detect the tangent regions and then eliminate the data in these regions from the final result, we can possibly avoid the errors due to tangent illumination. However, the issue may be more complicated due to multiple reflections from adjacent areas on the surface. Therefore, more experiments and analysis are necessary.

(2) Develop a real-time 360° 3D shape measurement system

In order to obtain full 360° shape information, there are two approaches. One is to rotate the object and the other is to use multiple systems. For the measurement of static objects, the former is feasible. However, for real-time applications, the latter is the only choice. A potential approach is to set up four systems around the object as illustrated in Figure 8.2. These four systems obtain 3D geometric patches independently from different angles. Full 360° shape can be reconstructed by stitching four patches together. The challenging tasks are: 1) How to synchronize the four systems, and 2) how

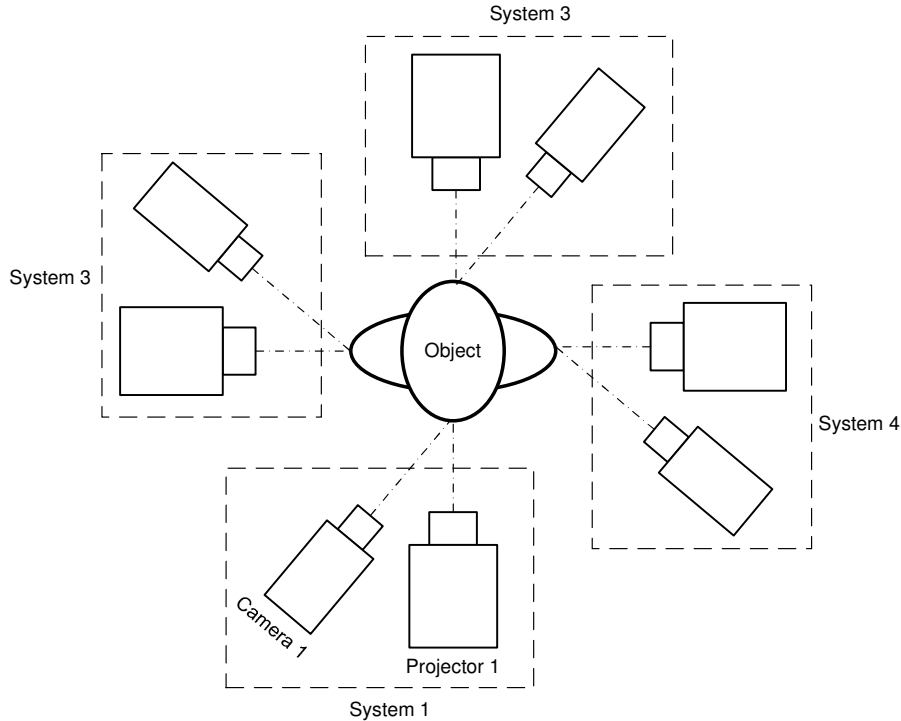


Figure 8.2: Full field real-time 3D measurement system.

to stitch four patches automatically and accurately.

(3) Explore applications of projectors as bi-directional devices

In this research, we found a way to allow a projector to “capture” images with the assistance of a camera. Therefore we have essentially converted a projector into a bi-directional device, which projects images as a normal projector and “captures” images like a camera. The potential applications of this device are extensive, including entertainment, plastic surgery, online assembly, etc., and should be explored.

(4) Explore more applications

This real-time system developed in this research has many potential applications, such as medical imaging, security, facial recognition, design and manufacturing, etc. During the course of this dissertation research, we have worked with other researchers to explore the applications of our real-time systems in the areas of computer vision and computer graphics, in partic-

ular human facial expression analysis and modeling, and facial recognition. We plan to continue this collaboration and in the mean time, explore more applications in other areas, especially biomedical.

Appendix A

World Coordinates Calculation

For the camera and projector, let's assume intrinsic matrices are A^c , A^p respectively. Extrinsic parameter matrices are $[R^c, t^c]$ and $[R^p, t^p]$ respectively. Assume

$$X = \{x^w, y^w, z^w\}^T \quad (\text{A.1})$$

is the world coordinates, and

$$I^c = \{u^c, v^c, 1\}^T$$

and

$$I^p = \{u^p, v^p, 1\}^T$$

are image coordinates of the camera and projector respectively. Then we have,

$$s^c I^c = A^c [R^c, t^c] \{X, 1\}^T \quad (\text{A.2})$$

$$= A^c R^c X + A^c t^c \quad (\text{A.3})$$

$$= B^c X + d^c \quad (\text{A.4})$$

where $B^c = A^c R^c$, $d^c = A^c t^c$

$$s^p I^p = B^p X + d^p \quad (\text{A.5})$$

here $B^p = A^p R^p$, $d^p = A^p t^p$

$$s^c I_i^c = \sum_3^{k=1} (B_{ik}^c X^k) + d_i^c \quad (\text{A.6})$$

$$s^p I_i^p = \sum_3^{k=1} (B_{ik}^p X^k) + d_i^p \quad (\text{A.7})$$

here $i = 1, 2, 3$, where the superscript means the element of the vector. I_1^c is the first element of vector I^c . The following notation follows the same definition. Then we have,

$$AX = b \quad (\text{A.8})$$

where A is a 3×3 matrix, and b is a 3×1 vector, Assume we know the horizontal line position of the corresponding pixels, then,

$$A_{ij} = B_{3j}^c I_i^c - B_{ij}^c \quad (\text{A.9})$$

$$A_{3j} = B_{3j}^p I_1^p - B_{1j}^p \quad (\text{A.10})$$

here $i = 1, 2, 3, j = 1, 2$. Where B_{ij}^c is the $i-th$ row, $j-th$ column element of matrix B^c .

$$b_j = d_j^c - B_{3j}^c d_3^c \quad (\text{A.11})$$

$$b_3 = d_3^p - B_{32}^p d_3^p \quad (\text{A.12})$$

Then

$$X = A^{-1}b$$

Bibliography

- [1] U. Dhond and J. Aggarwal, “Structure from Stereo-A Review,” IEEE Trans. Systems, Man, and Cybernetics **19**(6), 1489–1510 (1989).
- [2] R. Zhang, P.-S. Tsai, J. Cryer, and M. Shah, “Shape from Shading: A Survey,” IEEE Trans. on Pattern Analysis and Machine Intelligence **21**(8), 690–706 (1999).
- [3] M. Subbarao and T. Choi, “Focusing Techniques,” in *Proc. of SPIE*, pp. 163–174 (1992).
- [4] M. Subbarao and G. Surya, “Application of Spatial-Domain Convolution/Deconvolution Transform for Determining Distance from Image Defocus,” in *Proc. of SPIE*, pp. 159–167 (1992).
- [5] M. Levoy, K. Pulli, B. Curless, S. Rusinkiewicz, D. Koller, L. Pereira, M. Gingrton, S. Anderson, J. Davis, J. Ginsberg, J. Shade, and D. Fulk, “The Digital Michelangelo Project,” in *Proceedings of SIGGRAPH 2000*, K. Akeley, ed., Computer Graphics Proceedings, Annual Conference Series, pp. 131–144, ACM (ACM Press / ACM SIGGRAPH, 2000).
- [6] J. Batlle, E. M. Mouaddib, and J. Salvi, “Recent Progress in Coded Structured Light as a Technique to Solve the Correspondence Problem: A Survey,” Pattern Recognition pp. 1–63 (1998).
- [7] B. Curless, “Overview of Active Vision Techniques,” in *Proc. SIGGRAPH 99 Course on 3D Photography* (1999).
- [8] J. Davis, R. Ramamoorthi, and S. Rusinkiewicz, “Spacetime Stereo: A Unifying Framework for Depth from Triangulation,” IEEE Trans. on Pattern Analysis and Machine Intelligence **27**(2), 1–7 (2005).
- [9] G. Hobrough and T. Hobrough, “Stereopsis for Robots by Iterative Stereo Image Matching,” in *Proc. SPIE*, vol. 449 of *Intelligent Robots: 3rd Intl Conf on Robot Vision and Sensory Controls*, pp. 94–102 (1983).
- [10] A. Fusello, V. Roberto, and E. Trucco, “Efficient Stereo with Multiple Windowing,” in *IEEE Int'l Conference on Computer Vision and Pattern Recognition*, pp. 858–863 (1997).

- [11] R. C. Gonzalez and R. E. Woods, *Digital Image Processing* (Addison Wesly, 1992).
- [12] C. Sun, “A Fast Stereo Matching Method,” in *Digital Image Computing: Techniques and Applications*, pp. 137–148 (1997).
- [13] J. Weng, N. Ahuia, and T. S. Huang, “Matching Two Perspective Views,” IEEE Trans. on Pattern Analysis and Machine Intelligence **14**, 917–924 (1992).
- [14] P. J. Burt, “The Laplacian Pyramid as a Compact Image Code,” IEEE Trans. on Communications **31**(4), 532–540 (1983).
- [15] A. Koschan and V. Rodehorst, “Dense Depth Map by Active Color Illumination and Image Pyramids,” in *Advances in Computer Vision*, pp. 137–148 (1997).
- [16] L. Zhang, B. Curless, and S. Seitz, “Spacetime Stereo: Shape Recovery for Dynamic Senses,” in *Proc. Computer Vision and Pattern Recognition* (2003).
- [17] C. S. Fraser, “Photogrammetric Measurement to One Part in a Million,” Photogramm. Eng. Remote Sens. **58**(3), 305–310 (1992).
- [18] B. K. P. Horn and M. J. Brooks, *Shape from Shading* (MIT Press, Cambridge, MA, 1989).
- [19] R. A. Jarvis, “A Perspective on Range Finding Techniques for Computer Vision,” IEEE Trans. Pattern Analysis and Machine Intelligence **5**(2), 122–139 (1983).
- [20] E. Krotkov, “Focusing,” Int’l J. of Computer Vision **1**, 223–237 (1987).
- [21] J. S. Massa, G. S. Buller, A. C. Walker, S. Cova, M. Umasuthan, and A. M. Wallace, “Time of Flight Optical Ranging System Based on Time-Correlated Single-Photo Counting,” Appl. Opt. **37**(31), 7298–7304 (1998).
- [22] P. Besl, “Active Optical Range Imaging Sensor,” Machine Vision and Applications **1**, 127–152 (1988).
- [23] Z. Ji and M. C. Leu, “Design of Optical Triangulation Devices,” Opt. Laser Technology **21**(5), 335–338 (1989).
- [24] C. P. Keferstein and M. Marxer, “Testing Bench for Laser Triangulation Sensors,” Sens. Rev. **18**(3), 183–187 (1998).
- [25] J. L. Posdamer and M. D. Altschuler, “Surface Measurement by Space-encoded Projected Beam Systems,” Computer Graphics and Image Processing **18**(1), 1–17 (1982).
- [26] D. Skocaj and A. Leonardis, “Range Image Acquisition of Objects with Non-uniform Albedo Using Structured Light Range Sensor,” in *IEEE Proc. of the 15th International Conference on Pattern Recognition*, vol. 1, pp. 778–781 (2000).

- [27] J. Salvi, J. Pages, and J. Batlle, “Pattern codification strategies in structured light systems,” *Pattern Recognition* **37**(4), 827–849 (2004).
- [28] J. Pan, P. Huang, S. Zhang, and F.-P. Chiang, “Color N-ary Gray Code For 3-D Shape Measurement,” in *Proc. 12th Int'l Conference on Experimental Mechanics* (2004).
- [29] D. Caspi, N. Kiryati, and J. Shamir, “Range Imaging with Adaptive Color Structured Light,” *IEEE Trans. on Pattern Analysis and Machine Intelligence* **20**(5), 470–480 (1998).
- [30] E. Horn and N. Kiryati, “Toward Optimal Structured Light Patterns,” *Image and Vision Computing* **17**(2), 87–89 (1999).
- [31] B. Carrihill and R. Hummel, “Experiments with the Intensity Ratio Depth Sensor,” *Computer Vision, Graphics and Image Processing* **32**, 337–358 (1985).
- [32] T. Miyasaka, K. Kuroda, M. Hirose, and K. Araki, “Reconstruction of Realistic 3D Surface Model and 3D Animation from Range Images Obtained by Real Time 3D Measurement System,” in *IEEE 15th International Conference on Pattern Recognition*, pp. 594–598 (2000).
- [33] G. Chazan and N. Kiryati, “Pyramidal Intensity-Ratio Depth Sensor,” Tech. Rep. No. 121, Israel Institute of Technology, Technion, Haifa, Israel (1995).
- [34] S. Savarese, J. Bouguet, and P. Perona, “3D Depth Recovery with Grayscale Structured Lighting,” Tech. rep., Computer Vision, California Insititute of Technology (1998).
- [35] K. A. Haines and B. P. Hildebrand, “Contour Generation by Wavefront Construction,” *Phys. Lett.* **19**, 10–11 (1965).
- [36] K. Creath, Y. Y. Cheng, and J. Wyant, “Contouring Aspheric Surface Using Two-Wavelength Phase Shifting Interferometry,” *Opt. Acta.* **32**(12), 1455–1464 (1985).
- [37] R. P. Tatam, J. C. Davies, c. H. Buckberry, and J. D. C. Jones, “Holographic Surface Contouring Using Wavelength Modulation of Laser Diode,” *Opt. Laser Technol.* **22**, 317–321 (1990).
- [38] J. S. Zelenka and J. R. Varner, “Multiple-index Holographic Contouring,” *Appl. Opt.* **9**(2), 1431–1434 (1969).
- [39] Y. Y. Hung, J. L. Turner, M. Tafralian, J. D. Hovanesian, and C. E. Taylor, “Optical Method for Measuring Contour Slopes of an Object,” *Appl. Opt.* **17**(1), 128–131 (1978).
- [40] H. Ei-Ghandoor, “Tomographic Investigation of the Refractive Index Profiling Using Speckle Photography Technique,” *Opt. Commun.* **133**, 33–38 (1997).

- [41] C. Joenathan, B. Fraze, P. Haible, and H. J. Tiziani, "Contouring by Electronic Speckle Pattern Interferometry Using Dual Beam Illumination," *Appl. Opt.* **29**, 1905–1911 (1990).
- [42] R. Rodrguez-Vera, D. Kerr, and F. Mendoza-Santoyo, "Electronic Speckle Contouring," *J. Opt. Soc. Am. A* **9**(1), 2000–2008 (1992).
- [43] L. S. Wang and S. Krishnaswamy, "Shape Measurement Using Additive-Subtractive Phase Shifting Speckle Interferometry," *Meas. Sc. Technol.* **7**, 1748–1754 (1996).
- [44] F. Chen, G. M. Brown, and M. Song, "Overview of Three-Dimensional Shape Measurement Using Optical Method," *Opt. Eng.* **39**(1), 10–22 (2000).
- [45] F. P. Chiang, "Techniques of Optical Spatial Filtering Applied to the Processing of Moiré -Fringe Patterns," *Experimental Mechanics* pp. 523–526 (1969).
- [46] Y. Z. Dai and F. P. Chiang, "Moiré Interferometry Applied to Topographic Contour Measurement," in *Proc. SPIE*, vol. 954 of *Optical Testing and Metrology II*, pp. 153–157 (1988).
- [47] M. Idesawa, T. Yatagai, and T. Soma, "Scanning Moiré Method and Automatic Measurement of 3-D Shapes," *Appl. Opt.* **16**(8), 2153–2162 (1977).
- [48] V. Srinivasan, L. H. C., and M. Halioua, "Automated Phase-Measuring Profilometry of 3D Diffuse Objects," *Appl. Opt.* **23**(18), 3105–3108 (1984).
- [49] H. Takasaki, "Moiré Topography," *Appl. Opt.* **9**(6), 1467–1472 (1970).
- [50] A. J. Boehlein and K. G. Harding, "Adaptation of a Parallel Architecture Computer to Phase-shifted Moiré Interferometry," in *Proc. SPIE*, vol. 728 of *Optics, Illumination, and Image Sensing for machine Vision*, pp. 183–194 (1986).
- [51] M. Halioua and H.-C. Liu, "Optical Three-Dimension Sensing by Phase Measuring Profilometry," *Opt. and Lasers in Engineering* **11**, 185–215 (1989).
- [52] H. P. Stahl, "White-light Moiré Phase-measuring Interferometry," in *Proc. SPIE*, vol. 1332 of *Optical Testing and Metrology III: Recent advances in industrial optical inspection*, pp. 720–728 (1990).
- [53] L. H. Bieman, "Survey of Design Consideration for 3D Imaging System," in *Proc. SPIE*, vol. 1005 of *Optics, illumination, and image sensing for machine vision III*, pp. 138–144 (1988).
- [54] K. G. Harding and J. S. Harris, "Projection Moiré Interferometry for Vibration Analysis," *Appl. Opt.* **22**(6), 856–861 (1983).
- [55] C. Reich, R. Ritter, and J. Thesing, "3-D Shape Measurement of Complex Object by Combining Photogrammetry and Fringe Projection," *Opt. Eng.* **39**(1), 224–230 (2000).

- [56] W. Schreiber and G. Notni, “Theory and Arrangements of Self-calibrating Whole-body Three-dimensional Measurement Systems Using Fringe Projection Technique,” *Opt. Eng.* **39**(1), 159–169 (2000).
- [57] K. G. Harding, “Phase Grating Use for Slop Discrimination in Moiré Contouring,” in *Proc. SPIE*, vol. 1614 of *Optics, illumination, and image sensing for machine vision VI*, pp. 265–270 (1991).
- [58] Z. J. Geng, “Rainbow 3-D Camera: New Concept of High-Speed Three Vision System,” *Opt. Eng.* **35**, 376–383 (1996).
- [59] C. Wust and D. W. Capson, “Surface Profile Measurement using Color Fringe Projection,” *Machine Vision and Applications* **4**, 193–203 (1991).
- [60] P. S. Huang, Q. Hu, F. Jin, and F. P. Chiang, “Color-Encoded Digital Fringe Projection Technique for High-Speed Three-Dimensional Surface Contouring,” *Opt. Eng.* **38**, 1065–1071 (1999).
- [61] L. Zhang, B. Curless, and S. M. Seitz, “Rapid Shape Acquisition Using Color Structured Light and Multi-pass Dynamic Programming,” in *The 1st IEEE International Symposium on 3D Data Processing, Visualization, and Transmission*, pp. 24–36 (2002).
- [62] M. Takeda and K. Mutoh, “Fourier Transform Profilometry for the Automatic Measurement of 3-D Object Shape,” *Appl. Opt.* **22**(24), 3977–3982 (1983).
- [63] S. Rusinkiewicz, O. Hall-Holt, and L. Marc, “Real-Time 3D Model Acquisition,” in *SIGGRAPH*, vol. 1281 of *3D acquisition and image based rendering*, pp. 438 – 446 (ACM Press, 2002).
- [64] O. Hall-Holt and S. Rusinkiewicz, “Stripe Boundary Codes for Real-Time Structured-Light Range Scanning of Moving Objects,” in *The 8th IEEE International Conference on Computer Vision*, pp. II: 359–366 (2001).
- [65] P. S. Huang, C. Zhang, and F. P. Chiang, “High-Speed 3-D Shape Measurement Based on Digital Fringe Projection,” *Opt. Eng.* **42**(1), 163–168 (2003).
- [66] L. J. Hornbeck, “Current Status of the Digital Micromirror Device (DMD) for Projection Television Applications,” in *Intl. Electron. Devices Tech. Digest*, pp. 381–384 (1993).
- [67] J. M. Younse, “Mirrors on a Chip,” in *IEEE Spectrum*, pp. 27–31 (1993).
- [68] D. Malacara, ed., *Optical Shop Testing* (John Wiley and Sons, NY, 1992).
- [69] D. C. Ghiglia and M. D. Pritt, *Two-Dimensional Phase Unwrapping: Theory, Algorithms, and Software* (John Wiley and Sons, Inc, 1998).

- [70] W. H. Press, B. P. Flannery, S. A. Teukolsky, and W. T. Vetterling, *Numerical Recipes in C: the Art of Scientific Computing*, 2nd ed. (University of Cambridge, Cambridge, 1992).
- [71] C. Zhang, “Optical Profilometry and its Applications,” Ph.D. thesis, State University of New York at Stony Brook, Stony Brook, NY, 11794 (2001).
- [72] J. H. Brunning, J. E. Herriott, D. P. Gallagher, A. White, and D. J. Brangaccio, “Digital Wavefront Measuring Interferometer for Testing Optical Surfaces and Lenses,” *Appl. Opt.* **13**, 2693–2073 (1974).
- [73] D. Malacara, ed., *Optical Shop Testing* (John Wiley and Sons, NY, 1992).
- [74] P. S. Huang, Q. Y. Hu, , and F. P. Chiang, “Double Three-step Phase-shifting Algorithm,” *Appl. Opt.* **41**(22), 4503–4509 (2002).
- [75] R. Legarda-Sáenz, T. Bothe, and W. P. Jüptner, “Accurate Procedure for the Calibration of a Structured Light System,” *Opt. Eng.* **43**(2), 464–471 (2004).
- [76] F. J. Cuevas, M. Servin, and R. Rodriguez-Vera, “Depth Object Recovery Using Radial Basis Functions,” *Opt. Commun.* **163**(4), 270–277 (1999).
- [77] F. J. Cuevas, M. Servin, O. N. Stavroudis, and R. Rodriguez-Vera, “Multi-layer Neural Networks Applied to Phase and Depth Recovery From Fringe Patterns,” *Opt. Commun.* **181**(4), 239–259 (2000).
- [78] C. C. Slama, C. Theurer, and S. W. Henriksen, *Manual of Photogrammetry*, American Society of Photogrammetry, 4th ed. (Falls Church, VA, 1980).
- [79] C. S. Fraser, “Photogrammetric Camera Component Calibration: A Review of Analytical Techniques,” in *Calibration and Orientation of Camera in Computer Vision*, A. Gruen and T. S. Huang, eds., pp. 95–136 (Springer-Verlag, Berlin Heidelberg, 2001).
- [80] A. Gruen and H. A. Beyer, “System Calibration Through Self-Calibration,” in *Calibration and Orientation of Camera in Computer Vision*, A. Gruen and T. S. Huang, eds., pp. 163–194 (Springer-Verlag, Berlin Heidelberg, 2001).
- [81] J. Heikkilä, “Geometric Camera Calibration Using Circular Control,” *IEEE Trans. Pattern Anal. Mach. Intell.* **PAMI-22**(10), 1066–1077 (2000).
- [82] F. Pedersini, A. Sarti, and S. Tubaro, “Accurate and Simple Geometric Calibration of Multi-camera Systems,” *Signal Process* **77**(3), 309–334 (1999).
- [83] D. B. Gennery, “Least-square Camera Calibration Including Lens Distortion and Automatic Editing of Calibration Points,” in *Calibration and Orientation of Camera in Computer Vision*, A. Gruen and T. S. Huang, eds., pp. 123–136 (Springer-Verlag, Berlin Heidelberg, 2001).

- [84] Q. Hu, P. S. Huang, Q. Fu, , and F. P. Chiang, “Calibration of a 3-D Shape Measurement System,” Opt. Eng. **42**(2), 487–493 (2003).
- [85] D. C. Brown, “Close-range Camera Calibration,” Photogrammetric Engineering **37**(8), 855–866 (1971).
- [86] W. Faig, “Calibration of Close-range Photogrammetry System: Mathematical Formulation,” Photogrammetric Engineering and Remote Sensing **41**(12), 1479–1486 (1975).
- [87] C. Slama, *Manual of Photogrammetry*, 4th ed. (American Society of Photogrammetry, 1980).
- [88] J. Weng, P. Cohen, and M. Herniou, “Camera Calibration with Distortion Models and Accuracy Evaluation,” IEEE Trans. on Pattern Analysis and Machine Intelligence **14**(10), 965–980 (1992).
- [89] R. Y. Tsai, “A Versatile Camera Calibration Technique for High-accuracy 3D Machine Vision Metrology using Off-the-shelf TV Camera and Lenses,” IEEE Int. J. Robot. Automat. RA-3 **3**(4), 323–344 (1987).
- [90] G. Wei and S. Ma, “Implicit and Explicit Camera Calibration: Theory and Experiments,” IEEE Trans. on Pattern Analysis and Machine Intelligence **16**(5), 469–480 (1994).
- [91] Z. Zhang, “A Flexible New Technique for Camera Calibration,” IEEE Trans on Pattern Analysis and Machine Intelligence **22**(11), 1330–1334 (2000).
- [92] J.-Y. Bouguet, “Camera Calibration ToolBox for Matlab,” Online available at: http://www.vision.caltech.edu/bouguetj/calib_doc.